A MEASUREMENT OF THE COLOUR FACTORS OF QUANTUM CHROMODYNAMICS FROM FOUR-JET EVENTS AT LEP

Simon James Dorris

Department of Physics and Astronomy

The University of Glasgow

Thesis submitted for the degree of

Doctor of Philosophy

March, 1997

Abstract

From a sample of 3.7 million events collected with the ALEPH detector between 1992 and 1995, those containing four jets are selected. These are used to measure angular variables sensitive to the underlying spin structure of the event which are then combined with $\mathcal{O}(\alpha_s^2)$ QCD predictions to extract values of the Colour Factor ratios $\frac{C_A}{C_F}$ and $\frac{T_R}{C_F}$. Events containing two identified b jets are separated from the rest of the data and the extra information used to increase the accuracy of the measurement. A matrix element calculation which takes the b quark mass into account is used in the fit to these tagged events. The final Colour Factor values are obtained by combining the results from the two samples:

$$\frac{C_A}{C_F} = 2.294 \pm 0.151 \qquad \frac{T_R}{C_F} = 1.491 \pm 0.490$$

which are in agreement with the QCD predictions of $\frac{C_A}{C_F} = 2.25$ and $\frac{T_R}{C_F} = 1.875$.

Preface

This thesis presents a measurement of the Colour Factors of Quantum Chromodynamics from 4-jet events observed with the ALEPH detector using data collected at the LEP accelerator between 1992 and 1995.

The work of the ALEPH Collaboration depends on the efforts of many people over a long period of time. The author's contribution to the experiment included performing an upgrade to the Laser Calibration System of the Time Projection Chamber, periods as the TPC Coordinator and regular shifts monitoring the quality of the data as it was recorded.

The material presented here reflects the author's own analysis of the ALEPH data. No portion of the work described in this thesis has been submitted in support of an application for another degree or qualification in this, or any other, institute of learning.

Acknowledgements

Many people were involved in the creation of this thesis, and I would like to take the opportunity to thank one or two of them. My supervisor Robert Turnbull and Stan Thompson head the list for their contributions over the three years but I would also like to thank the other members of the Glasgow Experimental Particle Physics group, particularly Catherine MacIntyre and Pedro Teixera-Dias. Thanks also go to the ALEPH QCD and TPC groups and especially to the TPC Laser Team, Eric and Lee for their sparkling wit.

My personal thanks go to the people who have kept me happy throughout the endeavor which includes a great many souls. I cannot omit the efforts of my colleagues Fi, Martin, Richard, Allan and Steve and would also like to single out Dougal, Iain, Olly, Dave, Matt and Mark for being outstandingly entertaining from start to finish.

Finally I would like to acknowledge the faultless support of my family, all of whom have been invaluable, and of Miss Smith who has been indescribable.

Contents

List of Figures

Chapter 1

Quantum Chromodynamics and the Standard Model

1.1 Introduction

The aim of particle physics is to understand the ultimate constituents of matter and to describe the interactions between them. The search for a solution to this problem has brought with it an expanding collection of experimental evidence from the reactions of high energy particles which probe the structure of matter at ever smaller distances. This body of knowledge is summarized in a set of theories known as the Standard Model which encompass our progress to date in answering this fundamental question.

1.2 The Standard Model

The Standard Model expresses our current understanding in terms of two types of particle: the *fermions* from which all matter is constructed, and carrier particles called *bosons* which are exchanged between them. The bosons communicate the forces through which the fermions interact and always possess integer values of spin angular momentum (in units of $\hbar$). Fermions always have half-integer spin and are found in three generations sharing similar features.

Three Families

In each of the three fermion families we find two quarks and two leptons, together with their associated anti-particles. Quarks were originally observed in electron-proton scattering experiments in the 1970's. The high angle through which some electrons were deflected indicated some sub-structure within the proton in analogy to the Rutherford scattering of α particles from atomic nuclei. This structure is thought to be due to three point-like entities within the proton which we call quarks.

In the first of the three generations the leptons are the familiar electron with charge -1, and a particle with no charge or mass called the electron neutrino which is involved in radioactive β decay. The second and third families contain heavier versions of the electron together with their associated neutrinos.

The up and down quarks of the first family are found in the proton which contains two up and one down quark, and the neutron which contains two down and one up quark. Fractional values of electric charge were originally assigned to them in order to obtain the observed totals of +1 for the proton and 0 for the neutron but have since been directly confirmed as correct in other experiments.

The heavier quarks of the higher generations are found in unstable short lived particles. The recent discovery of the top quark by the CDF collaboration [1] completes the set of fundamental fermions predicted by the Standard Model. The following table summarizes the characteristics of these particles in a way which highlights the similarities between each family.

first generation

particle	symbol	charge	spin ($\hbar$)	mass (GeV)
up quark	u	$+\frac{2}{3}$	$\frac{1}{2}$	$\sim 5\text{x}10^{-3}$
down quark	d	$-\frac{1}{3}$	$\frac{1}{2}$	$\sim 1\text{x}10^{-2}$
electron	e	-1	$\frac{1}{2}$	$5\text{x}10^{-4}$
electron neutrino	ν_e	0	$\frac{1}{2}$	$< 5\text{x}10^{-9}$

second generation

particle	symbol	charge	spin ($\hbar$)	mass (GeV)
charm quark	c	$+\frac{2}{3}$	$\frac{1}{2}$	~ 1.3
strange quark	s	$-\frac{1}{3}$	$\frac{1}{2}$	~ 0.2
muon	μ	-1	$\frac{1}{2}$	0.106
muon neutrino	ν_μ	0	$\frac{1}{2}$	$< 2.7\text{x}10^{-7}$

third generation

particle	symbol	charge	spin ($\hbar$)	mass (GeV)
top quark	t	$+\frac{2}{3}$	$\frac{1}{2}$	174
bottom quark	b	$-\frac{1}{3}$	$\frac{1}{2}$	~ 5
tau	τ	-1	$\frac{1}{2}$	1.8
tau neutrino	ν_τ	0	$\frac{1}{2}$	$< 3.1\text{x}10^{-5}$

Four Forces

In the Standard Model all physical processes are explained through the interactions of four forces. Gravity is the most apparent of the four but is sufficiently weak relative to the others that it can be ignored at the energy scales we consider in particle physics and will not be considered further.

The electromagnetic force is described by Quantum Electrodynamics (QED) which is a locally gauge-invariant field theory (i.e. charge is locally conserved). It is mediated between charged particles by the exchange of massless neutral bosons called photons [2]. The coupling constant involved in the interaction, α, is sufficiently small to allow perturbation theory to be used successfully. The prediction obtained in this way for the magnetic moment of the muon has been experimentally confirmed to one part in 10^9 [3].

$$\alpha = \frac{e^2}{4\pi\hbar c\epsilon_0} \sim \frac{1}{137}$$

The weak interaction, which was originally suggested to explain the β decay of neutrons has also been formulated as a gauge theory in analogy to QED. It is communicated between quarks and leptons by the exchange of a triplet of bosons: the W^+, W^- and Z^0. The large mass of these particles results in the short range and thus relative weakness of the force. The weak and electromagnetic interactions as formulated in the Standard Model are unified, or considered to be different aspects of the same 'electroweak' force. This means that the two become equivalent in processes involving large momentum transfers.

The strong force is responsible for binding quarks together to form hadrons, such as the proton and neutron. As with electromagnetism and the electroweak interaction it is described by a local gauge field theory, known in this case as Quantum Chromodynamics (QCD). The force is communicated between quarks by massless bosons called gluons, the two being collectively known as 'partons'. Leptons do not couple to gluons and have no interaction with the strong force. Some further features of QCD are explored in the next Section.

The following table summarizes the characteristics of the gauge bosons of the Standard Model.

gauge boson	symbol	charge	spin ($\hbar$)	mass (GeV)
photon	γ	0	1	0
W^+ W^- bosons	$W^{\pm}$	± 1	1	80
Z boson	Z^0	0	1	91
gluon	g	0	1	0

The Standard Model as introduced above has passed stringent tests in a range of environments and has yet to be challenged by any decisive experimental evidence. It remains however a source of frustration in that it lacks the elegance desired of a fundamental theory and requires too many arbitrary constants.

As a result the search for theories which combine our current knowledge in a more fundamental framework continue. One contender is Supersymmetry which postulates a spin 0 partner for each quark and lepton and a spin $\frac{1}{2}$ partner for each of the gauge bosons [4]. In particular the theory predicts a spin $\frac{1}{2}$ partner for the gluon known as the 'gluino'. Current searches for these new particles have failed but the analysis presented in the thesis is sensitive to one area of low gluino mass which has yet to be excluded by experiment [5].

1.3 Quantum Chromodynamics

In order to explain the quark structure of hadrons a new kind of charge called 'colour' was proposed which had three possible values (e.g. red, green and blue) [6]. Quantum Chromodynamics describes the interaction of coloured quarks via the exchange of gluons which themselves carry colour charge and can interact with each other. This feature leads to the triple gluon vertex as shown in Figure 1.1 which displays the basic interactions of the theory.

In electromagnetic interactions we consider each charge to be surrounded by a cloud of virtual particle-antiparticle pairs which screen and thus reduce the impact of the bare charge. This introduces an energy dependence in the coupling

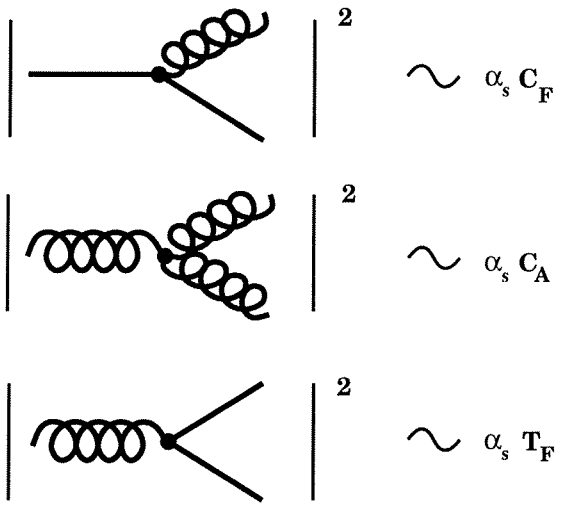

Figure 1.1: The basic vertices of the QCD interaction. The Colour Factors C_F, C_A and T_F can be thought of as representing the relative strength of each process.

strength as high energy processes penetrate further into the virtual cloud and see the unscreened charge, enhancing the strength of the interaction.

In QCD however the influence of the gluon self-interaction is to reverse the effect of the virtual cloud and produce an enhancement of the bare charge, resulting in a coupling that decreases with energy. This phenomenon is known as asymptotic freedom and aids calculation in that the strong coupling constant α_s becomes sufficiently small in high energy processes for perturbative methods to be used. Conversely at the other end of the energy spectrum the strength of the interaction becomes infinite. This fact is thought to be related to the non-observation of free quarks and the restriction of the known hadrons to two kinds of colourless combination: the qqq baryons with one quark of each colour making a 'white' composite, and the mesons with a colour-anticolour $q\bar{q}$ pair.

1.3.1 e^+e^- Annihilation to Quark-Antiquark Pairs

In Figure 1.2 we see a representation of a typical hadronic event from the process shown below.

$$e^+e^- \rightarrow Z^0/\gamma \rightarrow q\bar{q} \rightarrow jets$$

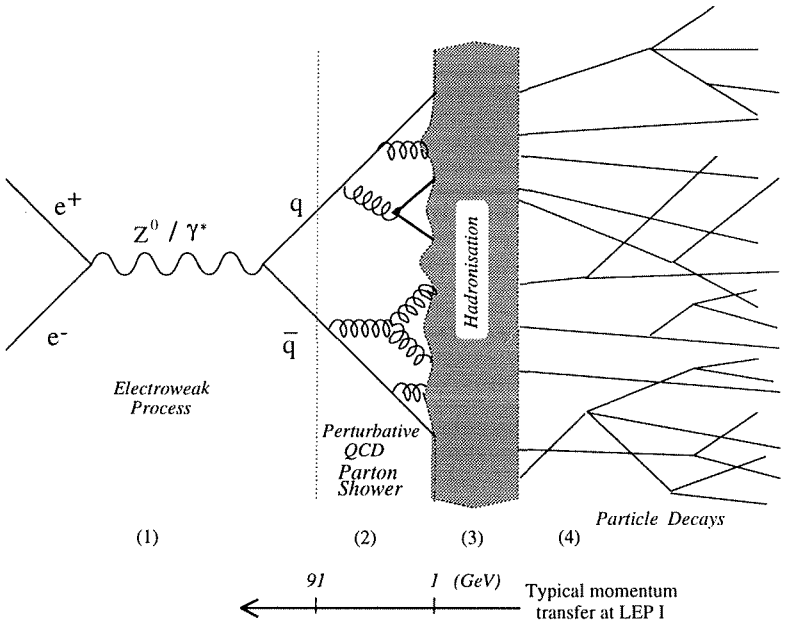

Figure 1.2: A schematic representation of a hadronic event.

The annihilation of the e^+e^- pair to produce the virtual Z^0/γ is followed by the production of a quark-antiquark. This process is well described by the Electroweak interaction mentioned above.

In the next step the $q\bar{q}$ radiate hard gluons which in turn radiate further partons. At this stage the high energy of the branchings ensures that α_s is small and perturbative techniques can provide an accurate description. This is not the case in the next section where the coloured partons combine to form colourless hadrons, resulting in collimated sprays of particles known as 'jets'. We have no reliable way to calculate the processes involved in this hadronization step and resort to phenomenological models, the details of which will be introduced below.

1.3.2 Perturbative QCD

The small value (~ 0.1) of the strong coupling constant at LEP I energy scales enables the use of perturbative expansions in α_s to describe the early quark and gluon branchings from the initial $q\bar{q}$ pair. The two calculational techniques commonly employed to obtain predictions are introduced below.

Matrix Element

The Matrix Element approach is to follow the expansion in α_s and calculate all Feynman diagrams for the process order by order. In principle this is the correct method as it includes all kinematic and helicity information but the number of diagrams to be computed increases rapidly at each order. The QCD interactions of the $q\bar{q}$ pair produced in e^+e^- annihilation have currently only been fully calculated to $\mathcal{O}(\alpha_s^2)$.

Parton Shower

This technique exploits simplified approximations to the full matrix element calculations which include any number of parton branchings. This is achieved by summing the leading terms in a rearranged perturbative expansion. The basic branching processes can then be described by simple expressions which depend on how the energy of the parent parton is divided between the two daughters [7].

This approach is very successful at describing some features of hadronic events and is the preferred one for many applications. Other analyses require a complete description of the kinematic and helicity information included in the matrix element method.

1.3.3 Hadronization

At the low energies involved in the hadron formation process perturbative techniques break down and we must employ phenomenological models inspired by physical arguments.

The string fragmentation model of the JETSET Monte-Carlo [8] approximates the colour field between the initial $q\bar{q}$ with a narrow flux-tube or 'string' drawn between the two. The constant energy per unit length of the tube causes a linearly rising potential as the two quarks move apart. This stored energy can produce a new $q'\bar{q}'$ or di-quark pair causing the string to break. The adjacent quarks at the end of each string are combined to form baryons and mesons. The process continues until only hadrons remain.

An alternative method is contained in the HERWIG Monte-Carlo [9] which splits any gluons left after the perturbative stage into $q\bar{q}$ pairs. Adjacent quarks are then combined to form colourless clusters which decay into hadrons via a two-body process.

1.3.4 Colour Factors and the Structure of the Strong Interaction

QCD describes the interactions of spin $\frac{1}{2}$ quarks and massless spin 1 gluons with colour charges determined by an underlying SU(3) group symmetry. These assignments determine the dynamics of the theory and can be tested directly.

The spin of the partons has been verified with considerable accuracy and found to agree with the QCD prediction [10]. In exploring their colour charges we must remember that the contribution of each process shown in Figure 1.1 to the observable cross-section is not gauge invariant due to the inclusion of interference terms. However the 'Colour Factors' C_F, C_A and T_F can be considered the physical manifestation of the underlying group structure and the intuitive connection shown in the Figure is valid. Thus we associate C_F with the coupling strength of a gluon to a quark, C_A with the gluon self-coupling and T_F with the gluon splitting to quarks. This leads to the interpretation of C_F as the colour charge of a quark and C_A as the colour charge of a gluon.

The Colour Factors are defined through the generators T^a and structure constants f^{abc} of any group:

$$\sum_{a=1}^{N_{adj}} (T^a T^{\dagger a})_{ij} = \delta_{ij} C_F$$

$$\sum_{a,b=1}^{N_{adj}} f^{abc} f^{*abd} = \delta^{cd} C_A$$

$$\sum_{i,j=1}^{N_{fun}} T^a_{ij} T^{\dagger b}_{ji} = \delta^{ab} T_F$$

where i,j =1,..,N_{fun} denote the colour of the quarks, and a,b,c,d = 1,.., N_{adj} the colour of the gluons. We have assumed that the fermions lie in the fundamental representation and the gauge bosons in the adjoint representation of the group. Summing over all indices in the equations for C_F and T_F we obtain a relation between the dimension of the two representations; $N_{fun}C_F = N_{adj}T_F$. Note that in the above equations the generators T^a can be represented by matrices and the structure constants are defined by the commutation relations between them:

$$[T^a, T^b] = i\sum_c f^{abc}T^c.$$

The Colour Factors provide a way of classifying theories and differentiating between them. In terms of these variables, all SU(N) theories have the structure:

$$C_F = \frac{N^2-1}{2N} \qquad C_A = N \qquad T_F = \frac{1}{2}$$

and all abelian theories have $C_A = 0$. For example QED is specified through $C_F = T_F = 1$ and $C_A = 0$. QCD, which is based on an SU(3) symmetry, predicts $C_F = \frac{4}{3}, C_A = 3$ and $T_F = \frac{1}{2}$.

The factor T_F enters into the cross-section once for each quark flavour and thus the product $n_f T_F$ where n_f represents the number of active strongly interacting fermions is often abbreviated to $T_R = n_f T_F$. If the C_F factor is absorbed into the definition of the coupling constant we can describe the dynamics of a theory efficiently through two ratios: $\frac{C_A}{C_F}$, the ratio of the gluon self-coupling to the quark-gluon coupling, and $\frac{T_F}{C_F} = \frac{N_{fun}}{N_{adj}}$, the number of colours divided by the number of gluons. The values predicted by QCD for these ratios are: $\frac{C_A}{C_F} = \frac{9}{4} = 2.25$ and $\frac{T_F}{C_F} = \frac{3}{8} = 0.375$.

This topic will be discussed again in Chapter 4 which introduces a method by which these ratios can be determined experimentally.

Chapter 2

The ALEPH Detector

2.1 The ALEPH Detector at LEP

The Large Electron Positron Collider (LEP) is located near Geneva in Switzerland and is the largest in a sequence of five accelerators at CERN. It provides beams for four multi-purpose experiments which are designed to study e^+e^- interactions at energies of up to 200 GeV.

The leptons are accelerated in stages by the smaller accelerators (see Figure 2.1) culminating in the 22 GeV Super Proton Synchrotron which injects directly into the 27km LEP ring. The electrons and positrons circulate in LEP in opposite directions under the control of thousands of bending and focussing magnets which keep them separated until they are forced to collide at the experiments. During collision the beams converge to a 250μm interaction region.

The analysis presented here is based upon data collected at the Z^0 resonance between 1992 and 1995. This thesis also contains hardware work and some results from the recent high energy phase of LEP operation above 130 GeV.

2.2 The ALEPH Detector

The ALEPH detector is described in detail elsewhere [11, 12]. This Chapter provides an overview of the general principles of the detector while emphasizing the features most relevant to the analysis.

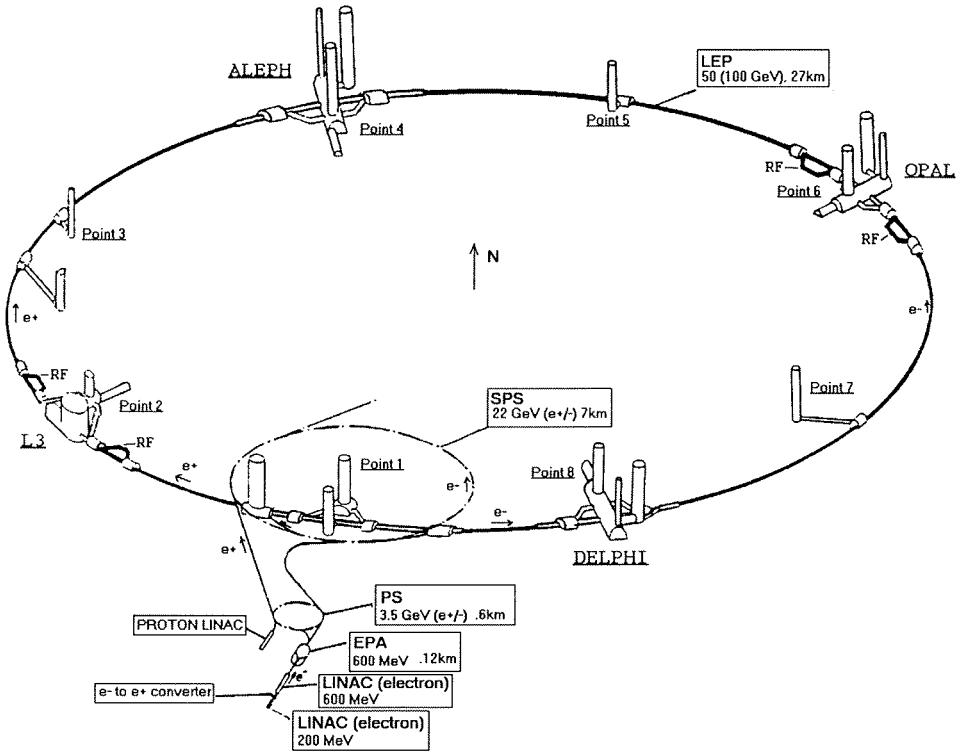

Figure 2.1: LEP and the CERN Accelerator Chain.

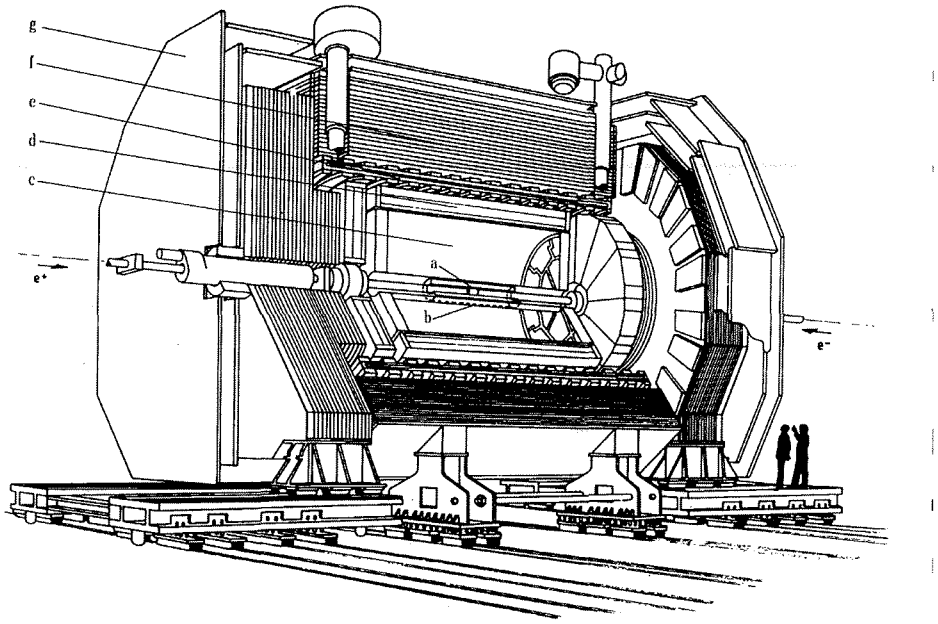

Figure 2.2: Cut away view of the 14m long ALEPH Detector showing subdetector components: *a:* Vertex Detector *b:* Inner Tracker *c:* TPC *d:* ECAL *e:* Superconducting Solenoid *f:* HCAL *g:* Muon Chambers.

The detector has a modular construction and is organised in concentric cylinders around the e^+e^- interaction point as shown in Figure 2.2. The inner modules provide tracking information on the particles produced by the collision, allowing momentum information to be derived from the curvature produced in the 1.5 Tesla magnetic field. Particles then pass to the outer layers where they are absorbed and their energy is measured.

Z^0 decays are often complex with around 20 charged and a similar number of neutral particles distributed around the full solid angle. As a result ALEPH is designed to combine high granularity with hermetic coverage. The low trigger rate at LEP facilitates this approach by making it possible to record as much information as required from each event, allowing precision tracking with an emphasis on momentum and vertex information.

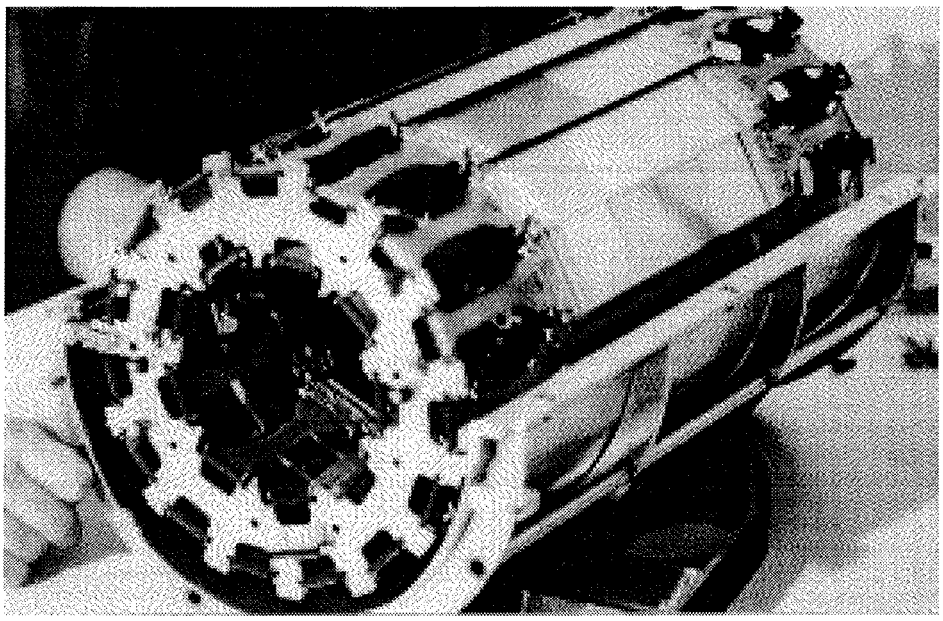

Figure 2.3: ALEPH's Silicon Vertex Detector.

2.2.1 Vertex Detector

In the region around the interaction point tracking information is provided by a vertex detector (VDET) consisting of two coaxial cylinders of double-sided silicon microstrip wafers at average radii of 6.5 and 11.3cm which cover respectively 85% and 69% of the solid angle (see Figure 2.3). The main purpose of the detector is to allow the identification of the displaced decay vertices of long-lived particles containing b-quarks.

Each of the 96 silicon wafers measures 5.12cm by 5.12cm and is divided into 100μm pitch strips which are read out in the $r\phi$ direction on one side and in rz on the other. The convention is such that the z axis lies along the beam-pipe, r is the radial distance from it and ϕ the azimuthal angle around it.

Hits are reconstructed independently for each side by combining the charge weighted positions of adjacent strips. These are then assigned to tracks extrapolated from the outer detectors with an efficiency approaching 98%.

The small overlap in ϕ between the active region of the wafers allows the point resolution to be measured directly, which for high momentum (>2 GeV/c) tracks

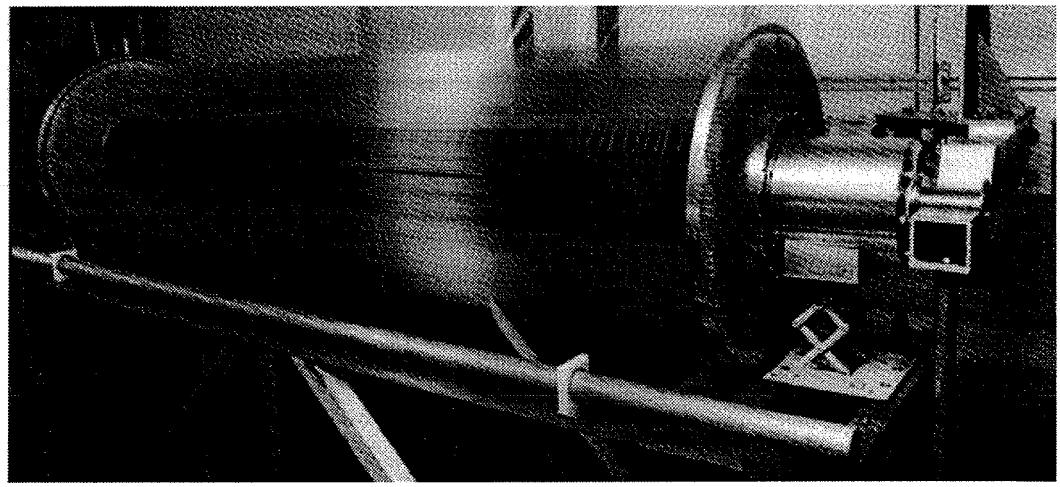

Figure 2.4: The 2m long Inner Tracking Chamber.

results in an accuracy of 12μm in both directions.

The original VDET was replaced by an improved detector in October 1995 for the high energy LEP run. The new VDET shares the main characteristics of its predecessor but increases coverage of the solid angle to 90% for the inner layer while offering greater resistance to radiation damage.

2.2.2 Inner Tracker

The Inner Tracking Chamber surrounds the vertex detector and provides tracking via 8 concentric layers of hexagonal drift cells. These combine a point resolution in $r\phi$ of 150μm with some coarse z information, allowing implementation of a fast 3-dimensional track trigger capable of reaching a decision in under 6 μs.

2.2.3 Time Projection Chamber

The Time Projection Chamber occupies most of the tracking volume and provides up to 21 space points on each track at radii from 30 to 180cm. Figure 2.5 shows the TPC's cylindrical structure surrounding the Inner Tracker.

A drift field running parallel to the z axis is provided by a central membrane held at 27kV with respect to the end-plates. When charged particles pass through

the gas they leave behind a trail of ionization electrons which drift in this field towards end-caps instrumented with a proportional wire system read out by segmented cathode pads. The $r\phi$ resolution of 173 μm relies on making corrections for inhomogeneities in the electric and magnetic fields and accurate knowledge of the end-cap alignment.

The arrival time of ionization electrons at the end-plates is used to obtain a position in z for each hit accurate to 740 μm for a track within 10° of perpendicular to the beams. This is combined with the $r\phi$ information to produce a full 3-dimensional reconstruction of the event.

In addition to the cathode pads used in the main readout the proportional chambers contain a system of sense wires. These allow up to 338 samples of ionization energy loss (dE/dx) per track making some particle identification possible. There is also a gating system designed to prevent ions from re-entering the drift volume where they could cause field distortions.

A Laser Calibration System measures the drift velocity of electrons in the TPC gas and also monitors irregularities in the electric and magnetic fields. Chapter 3 provides more information about the Laser System and details the upgrade it received for the high energy LEP run.

2.2.4 Electromagnetic Calorimeter

The Electromagnetic Calorimeter (ECAL) is a lead/proportional wire-chamber sampling device. It covers 98 % of the solid angle and consists of a 4.8m long barrel region closed by two end-caps, all lying within the superconducting magnet coil to minimize the amount of material preceding it. Both end-caps and the barrel are each sub-divided into 12 modular regions in ϕ as shown in Figure 2.6. Each module consists of 45 fully instrumented layers corresponding to around 22 radiation lengths.

Each layer contains a lead sheet in which electrons and photons can produce showers of other electromagnetic particles. These cause signals in the proportional wire-chambers which are read out by 3cm × 3cm cathode pads. These are

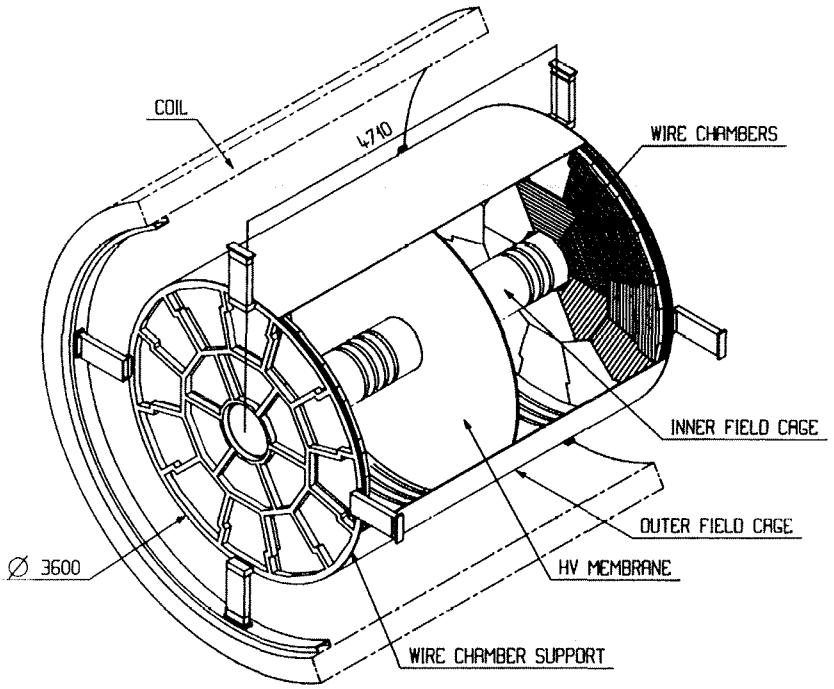

Figure 2.5: The Time Projection Chamber.

connected internally in three segments of depth and arranged in projective towers subtending an angle of $0.9° \times 0.9°$ at the interaction point. This high granularity is central to the performance of the ECAL in finding electrons and photons in hadronic jets.

In addition to the main pad readout, the wire planes of each module provide fast signals which allow a trigger to be implemented. The redundancy provided by the two readout chains allows signals from occasional electronic noise to be removed and thus retain sensitivity to low energy clusters.

By comparing the momentum of particles measured in the tracking detectors with the energy found by the ECAL, a resolution of $\frac{\Delta E}{E} = \frac{0.18}{\sqrt{E/GeV}} + 0.009$ is measured for electrons. This is complemented by an angular resolution for both charged and neutral tracks of 0.05° obtained by interpolating between the signals in adjacent towers.

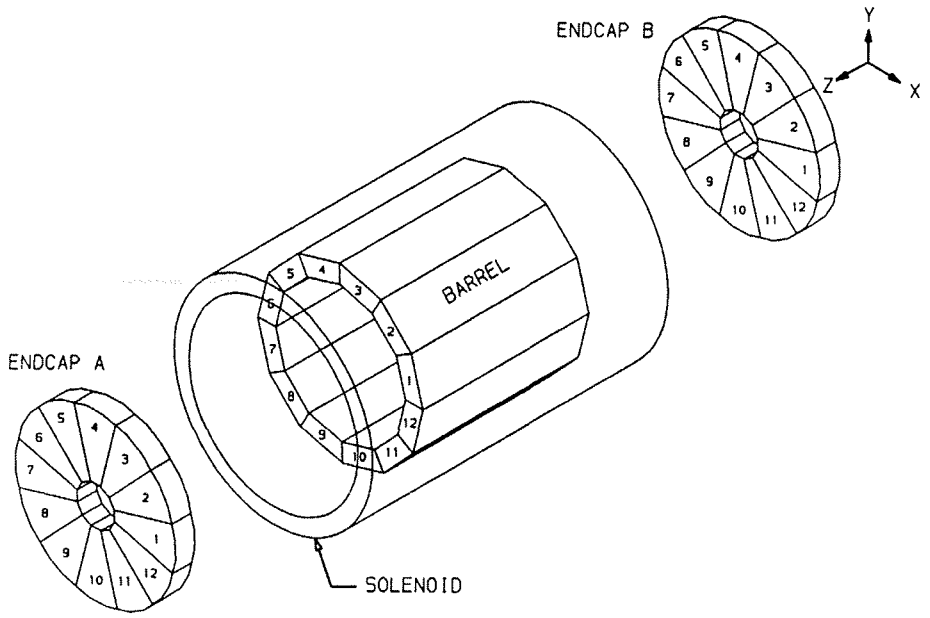

Figure 2.6: Electromagnetic Calorimeter Module Layout.

2.2.5 Hadron Calorimeter

The Hadron Calorimeter (HCAL) consists of alternate layers of iron and streamer tubes organised with a modular layout similar to that of the ECAL. The sheets of iron provide a total of 7 interaction lengths of material in which hadrons dissipate energy by generating showers of particles, and also provide the return yoke for the magnetic field.

Instrumentation is provided between each layer by streamer tubes similar to the wire chambers used in other detector elements. These are readout by cathode pads arranged in projective towers of 3.7° x 3.7°. These correspond to 4 x 4 blocks of ECAL towers but are rotated by 2° to allow detection of particles which escape through the cracks between modules in the electromagnetic calorimeter. Using the pad readout an energy resolution of $\frac{\Delta E}{E} = \frac{0.85}{\sqrt{E/GeV}}$ is obtained for hadronic showers.

Digital strips running along the 1cm square streamer tubes provide a longitudinal profile of the shower development which is used in differentiating between hadrons and minimum ionizing muons. These are the only charged particles likely to penetrate the HCAL, and in order to identify them the outer shell of the detector is surrounded by a double layer of streamer tubes which provide positional

information.

The signals from the HV wires of all streamer tubes are read out as part of a trigger used in conjunction with the ITC to distinguish e^+e^- interactions from background events.

2.2.6 Luminosity Measurement

The luminosity delivered by LEP is determined from the rate of low angle Bhabha scattering events for which the cross-section is calculable. An accurate determination relies on knowledge of the position of the scattered electrons because the cross-section is a strong function of the scattering angle. In the period before 1992 the measurement was made by a lead/proportional wire device similar to ECAL but covering the area close to the beam-pipe from 2° to 9°. This Luminosity Calorimeter (LCAL) was then superseded by a Tungsten/Silicon Calorimeter (SiCAL) capable of providing superior spatial resolution.

During this period LCAL remained in operation extending the low-angle coverage of the detector. As a result of recent changes in LEP timing which are incompatible with the SiCAL readout, the LCAL is once again being used for the primary luminosity measurement.

2.2.7 The Trigger System

The ALEPH trigger aims to accept all real e^+e^- interactions while minimizing dead-time from background events. It is organized in 3 levels which use partial information to make increasingly strict demands on an event before a decision is taken to record it.

LEP currently operates in a 'bunch train mode' of 4 trains which collide every 22μs. The trains can contain 4 wagons, each separated by 250 ns, but the ALEPH hardware reacts to these as one large 'super-bunch'. Of the 45,000 bunch crossings which occur every second, fewer than 10 produce an interaction. This requires the inclusive trigger philosophy mentioned above.

The Level 1 decision is based on information from the ITC, which is tested for track segments, and the calorimeters which are examined for energy deposits. If these are found in the regions indicated by the ITC tracks a YES decision is reached. This conclusion is possible irrespective of the Inner Tracker if a large signal is observed in the ECAL or LCAL. The decision is available in under $6\mu s$ from the time of the beam crossing.

If the Level 1 trigger produces a negative result the detector is reset in time for the next crossing. When a positive result is given the Level 2 trigger initiates readout of the TPC; this takes $50\mu s$. Trigger pads in the TPC produce a more detailed picture of the event upon which the same criteria as above are re-applied. A YES initiates full readout of the detector while a NO causes a reset, returning it to readiness for the next event $100\mu s$ after the Level 1 YES.

The final Level 3 trigger consists of a software process which analyses the event before it is recorded to verify earlier decisions.

Events from genuine interactions tend to satisfy more than one trigger. This redundancy allows measurement of the trigger efficiency by looking at whether one or both fire. The efficiency for Z^0 decays is found in this way to be greater than 99.99%.

2.2.8 Data Acquisition

The readout chain aims to convert the raw data of sub-detector hits into a reconstructed event as quickly as possible in order to reset the detector for the next event.

It is organised as a series of links in a data pipeline, each of which consists of a VME micro-processor capable of dealing with several events at once. The final step in the pipeline is reached when the Main Event Builder concatenates all elements of the event together and sends it to the online cluster. The structure of the readout chain is shown in Figure 2.7.

A group of computers known as the Online Cluster runs the Level 3 task to verify that the event came from a genuine interaction and simultaneously

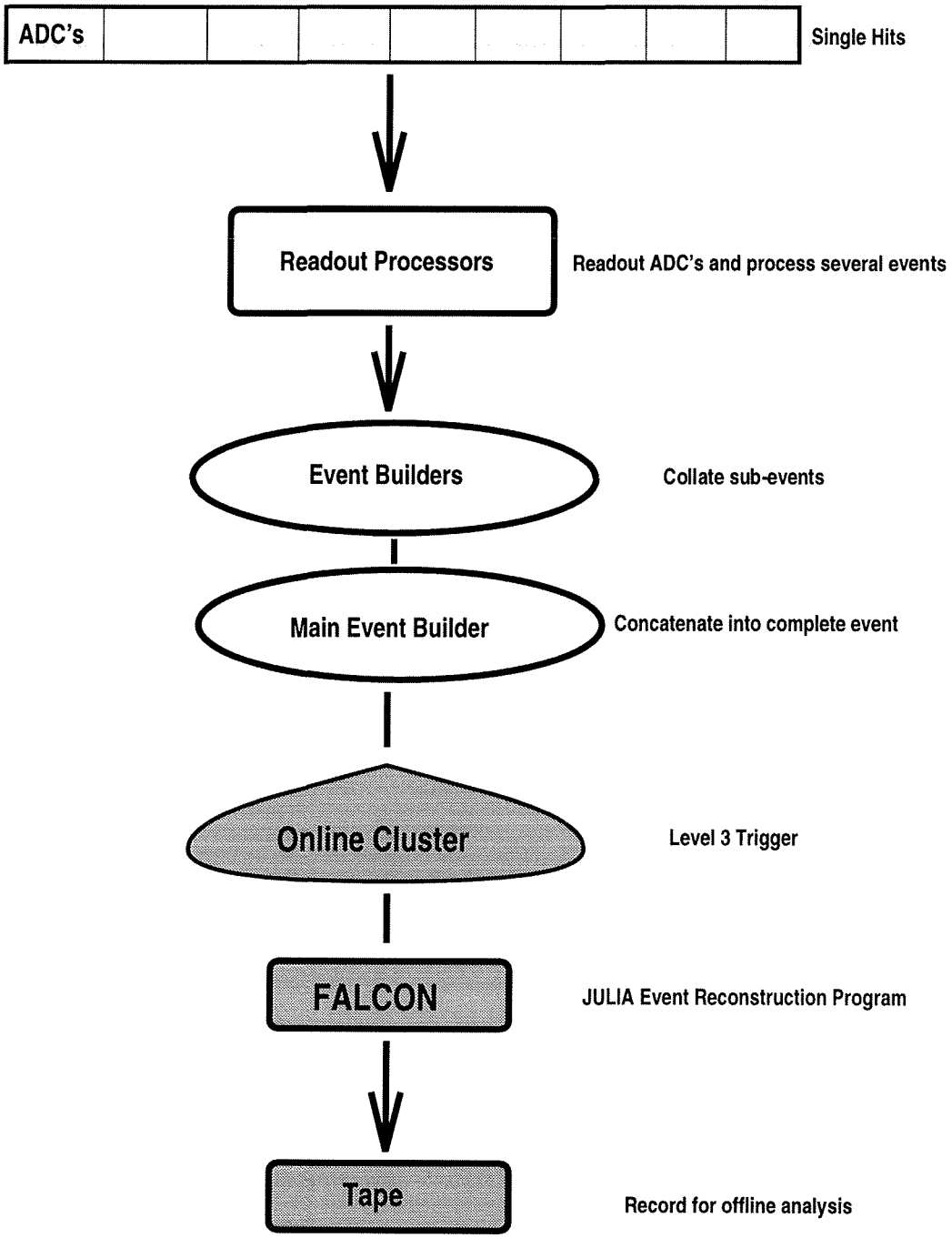

Figure 2.7: Readout structure from ADC to Tape.

passes it to other tasks which monitor the quality of the data coming from each sub-detector. If the Level 3 criteria are met the event is passed to a second computer cluster known as 'FALCON' which reconstructs the event in a quasi-online environment using the 'JULIA' program. It is then passed to a task which writes the event to tape for offline analysis. Reference [14] contains more detailed information on the data acquisition system.

2.3 Event Reconstruction

2.3.1 Track Reconstruction

The ALEPH reconstruction program, JULIA, begins the task of building tracks by combining nearby TPC hits into track segments which are then added together if compatible with a helix hypothesis. These candidate tracks are then extrapolated into the ITC where hits are assigned using $r\phi$ information only. VDET hits are assigned next, producing a preliminary track upon which a final fit is then performed. This last step considers track errors and uses Kalman techniques [15] to account for possible multiple scattering and in-flight decays.

When the hits from all three tracking detectors are combined we obtain a transverse momentum resolution from the track curvature in the magnetic field of $\sigma(1/p_T) = 6 \times 10^{-4}$ (GeV/c)$^{-1}$ for 45 GeV/c muons with an impact parameter resolution of around 25μm. At low track momenta scattering effects become more important leading to the addition of a constant term of 5×10^{-3} to the momentum resolution.

2.3.2 The 'Energy Flow' Algorithm

Rather than performing a straight summing of calorimeter cells, an improved picture of the total energy in an event can be formed by including tracking and particle identification information.

After a cleaning stage during which beam gas particles and noisy channels are removed, the remaining tracks are extrapolated to the outer detectors where

Measurement Method	Measurement Energy	Resolution $\Delta E/E$
Single Particle Tracking $\Delta p/p$	10 GeV	1 %
Single Particle ECAL	10 GeV	8 %
Single Particle HCAL	10 GeV	27 %
Whole Event Energy Flow	91 GeV	7 %
Whole Event Σ Cells	91 GeV	13 %

Table 2.1: Energy resolutions for isolated charged particles in tracking and calorimetry compared with whole event energy flow results.

overlapping ECAL and HCAL clusters are combined into 'calorimeter objects' and assigned to compatible tracks. Electron, muon and photon clusters are identified using dE/dx and shower profile estimators and then removed. Any remaining clusters compatible with a charged track are assigned the momenta of that track and also removed. All remaining calorimeter energy is assumed to come from neutral hadrons. This results in a set of 'energy flow objects' which are the input to the offline analysis presented here.

Using this method the energy of an event can be measured with greater accuracy than with the summing technique. Table 2.1 displays the energy resolution of the whole event obtained using the two algorithms and compares this with the response of the calorimetry and tracking to isolated 10 GeV charged particles. The 'single particle' resolutions are calculated by extrapolating the results quoted in earlier Sections to 10 GeV.

The resolution obtained from the energy flow algorithm is shown as a function of the angle of the event Thrust axis to the beam-pipe, θ in Figure 2.8. The energy detection efficiencies for hadronic and leptonic events are also shown which demonstrate the hermeticity of the detector.

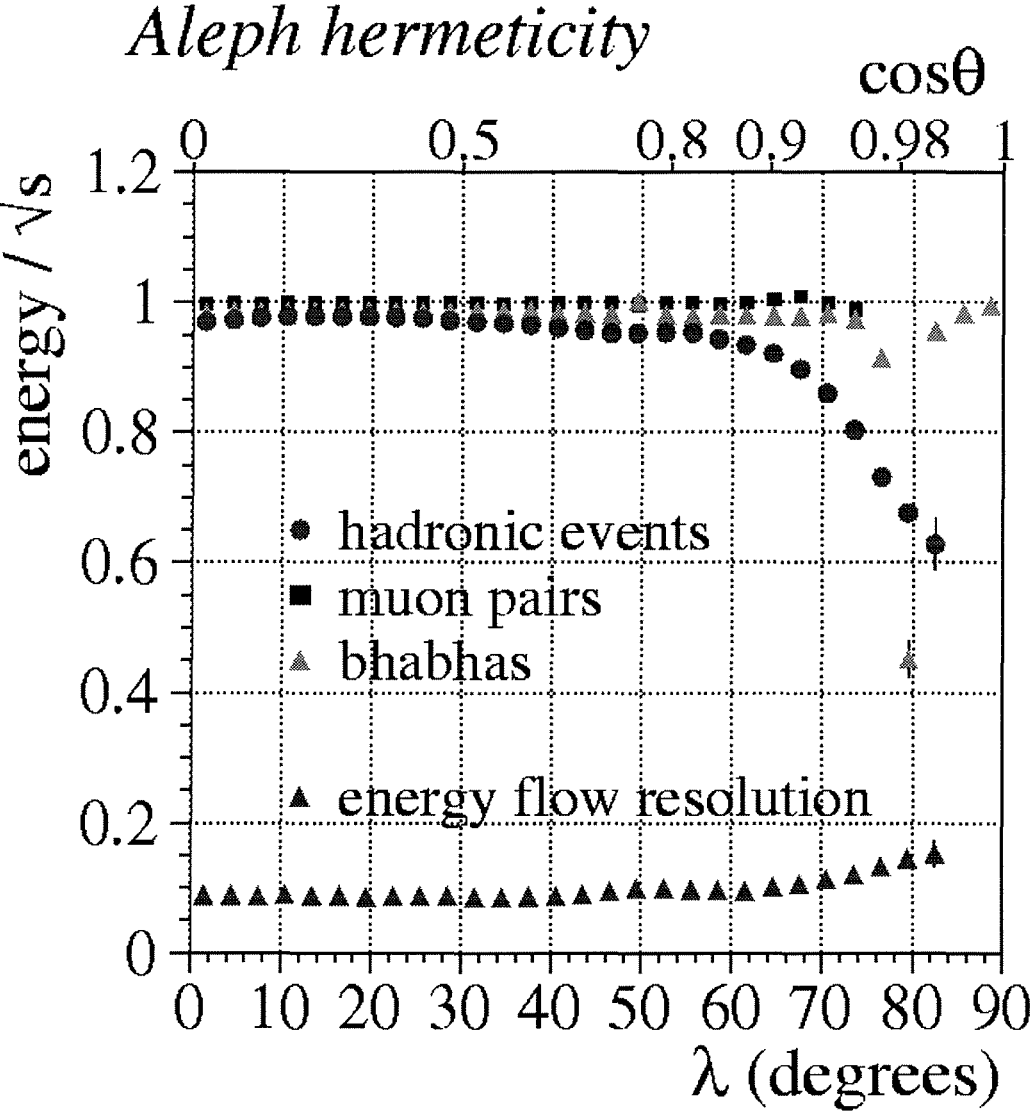

Figure 2.8: Energy resolution achieved with the energy flow algorithm as a function of the angle of the event Thrust-axis to the beam pipe, θ. The Thrust-axis is defined in Section 5.3. On the lower scale the angle is given in terms of $\lambda = \pi/2 - \theta$. Also shown are total energy detection efficiencies for leptonic and hadronic events, expressed as the ratio of the detected energy to twice the beam energy.

2.3.3 Reconstructed Event

Figure 2.9 shows a fully reconstructed ALEPH event in three projections. The main view is along the beam-pipe and shows TPC hits as small squares connected by the line of the track fit. The small circular view is an enlargement of the ITC and VDET from the same direction showing the extrapolation of these tracks toward the interaction point.

The third view is an end-on picture showing ECAL hits as squares which display the projective geometry of the towers. The energy deposition in the HCAL is represented by a histogram. A muon, visible at the edge of the picture, penetrates the calorimetry and registers hits in both muon chambers. The small amount of ionization caused by the track as it passes through the HCAL is shown in the main view.

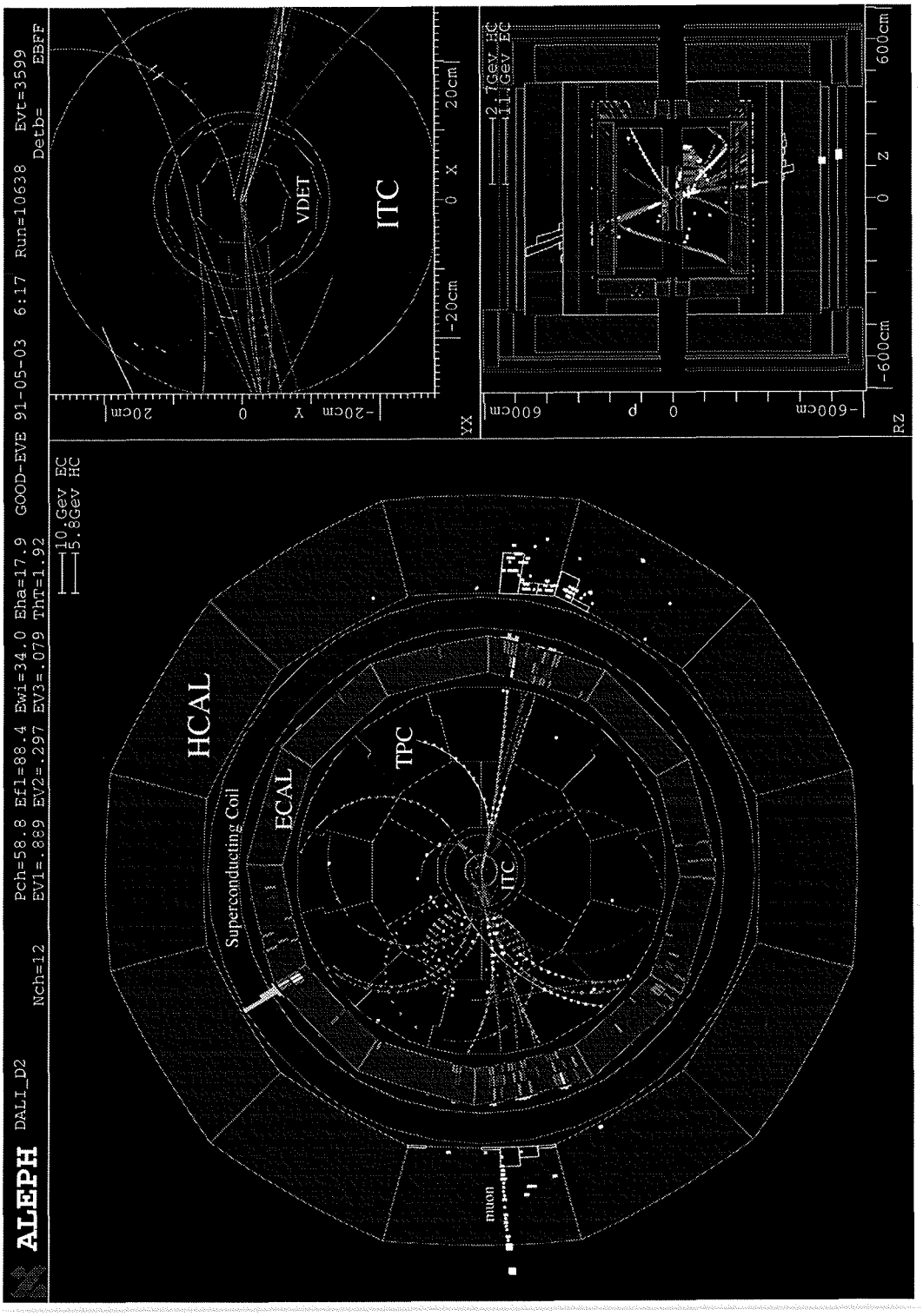

Figure 2.9: A Fully Reconstructed ALEPH Event.

Chapter 3

The TPC Laser System

3.1 Introduction

In this Chapter a project to upgrade the Laser Calibration System of the ALEPH TPC is presented. After introducing the laser calibration method the need for an upgrade to meet the new demands of high energy running at LEP II is discussed. This is followed by an explanation of the system's main components and the principle by which information is extracted from the calibration events. The objectives of the upgrade are then defined followed by a summary of the steps taken to meet them.

The ALEPH tracking performance relies on the Time Projection Chamber as detailed in Section 2.2.3. The quality of track reconstruction possible with a TPC depends upon knowledge of the distortions experienced by electrons as they drift towards the end-plates. It is therefore necessary to measure and correct for these effects.

The TPC Laser System performs two complementary functions to improve the accuracy of track reconstruction. It monitors irregularities in the electric and magnetic fields which can cause systematic shifts in track co-ordinates and also measures the drift velocity of electrons in the TPC gas.

The z position of each point on a track is obtained by combining the arrival time of electrons at the end-caps with the drift velocity, which is a function

of atmospheric pressure and requires constant monitoring. The control of field distortions is vital as they can cause 5% shifts in the measured momentum of a 45 GeV/c track, while any change in the drift velocity directly affects the reconstructed angle of tracks in the rz plane.

The accuracy with which the momentum and angle of tracks can be reconstructed is fundamental to the analysis presented later in this thesis; it will also be of importance to high energy analyses which attempt to determine the mass of the W boson.

3.2 Motivation for Upgrade to System

During the six years up to mid 1995 LEP ran at a c.m.s. energy of around 91 GeV, the mass of the Z^0 boson. During this time the primary measurement of drift velocity came from analysis of hadronic events. However, in order to search for new particles and provide information about W^+W^- production, the accelerator began a scan in energy above the Z^0 mass in October 1995.

The preliminary stage of 'LEP II', as the high energy machine is known, provided events at 140 GeV in late 1995, and the W threshold (161 GeV) was passed in July 1996. It is intended to continue up to 192 GeV when further accelerating cavities have been incorporated and to continue taking data until 1999.

At the high energies of LEP II running the cross-section for hadronic events drops by a factor of around 10^3 compared to its value at the Z^0 resonance. As a consequence we no longer have enough data to obtain the drift velocity in this way and the primary measurement must come from the Laser System.

During LEP I operation dedicated laser runs were taken every few weeks to allow a cross check of the drift velocity and to monitor field distortions. However, the new requirement for continuous operation of the Laser System at LEP II forces fundamental changes to the system.

The remainder of this Chapter describes the efforts undertaken to upgrade the Laser System to provide laser calibration events interleaved with normal data

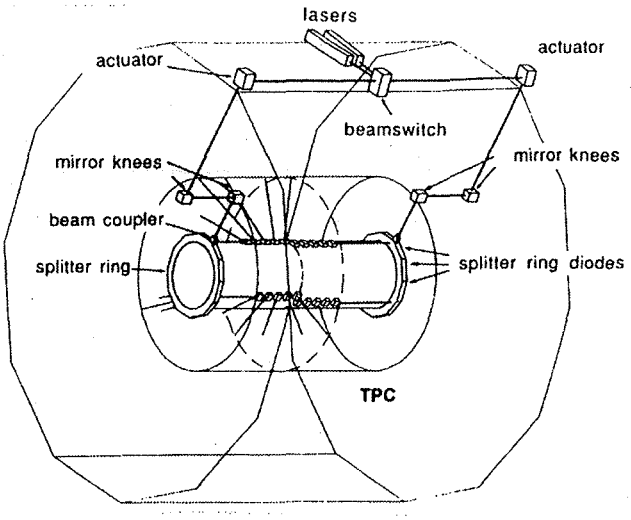

Figure 3.1: Schematic outline of the Laser System showing lasers and 15m beam path through ALEPH to the TPC.

taking in a robust and reliable system.

3.3 The TPC Laser System

The TPC Laser System consists of two lasers which transmit light into the TPC via a complex beam transport system as shown in Figure 3.1. The system exploits the fact that ultra-violet light can excite a two-photon resonance in organic impurities in the Argon/Methane gas inside the TPC and cause an ionization trail similar to that left by the passage of a charged particle. The ionization is caused by the interaction of U.V. light with phenol or toluene present in the gas at the ppm level [16]. This allows a real track to be mimicked by a perfectly straight laser track; any deviations from straightness are then due to inhomogeneities in the electric and magnetic fields as the electrons drift towards the end-plates. The measured curvature in laser tracks is then used to correct particle tracks. The drift velocity is determined from the reconstructed polar angle of laser tracks, the differences of which are known to 0.02° [17].

Using a suitable laser and a set of semi-reflecting mirrors on the inside of the

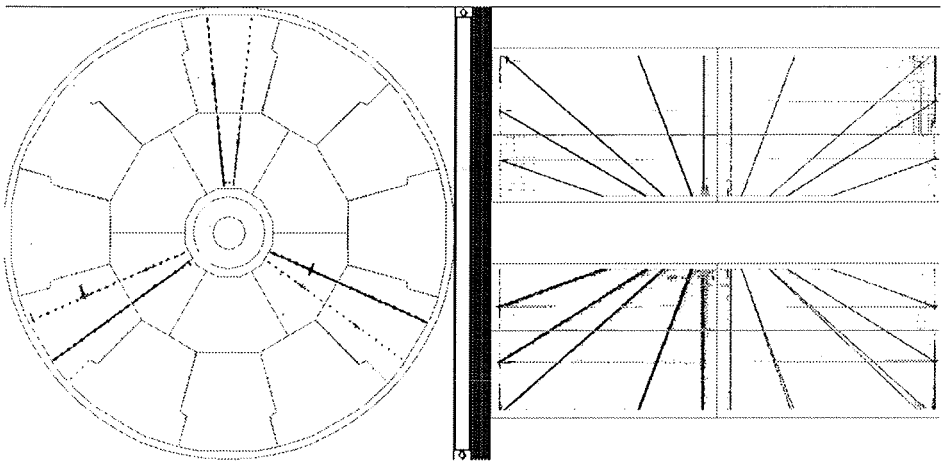

Figure 3.2: A Laser Event in the TPC.

TPC, mock hadronic events consisting of 30 laser tracks distributed throughout the volume of the detector can be recreated. One of these 'laser events' is shown in Figure 3.2. The reproducibility of tracks makes it possible to average over statistical fluctuations and study systematic effects.

An introduction to the construction of the TPC is given in Section 2.2.3. A full discussion can be found in References [11, 12, 13].

3.3.1 The Lasers

The system is divided into two symmetric halves, each served by a Nd-YAG laser running at a wavelength of 1064nm. After two frequency doubling crystals this reaches an output wavelength of 266nm in the near Ultra-Violet with a pulse length of 5ns and maximum repetition rate of 10Hz.

The pulse energy of over 2mJ is monitored by an internal photo-diode and is sufficient to produce 15 ionizing beams in the TPC after the losses of the beam transport system. The plane of polarization of the laser light can be manipulated via a half-wave plate to equalize the intensity of the beams. A telescope mounted on the front of the lasers produces a waist of the beam in the TPC with an average width of around 5mm. The laser energy and repetition rate are controlled from the ALEPH online computer cluster via an electronic module.

The lasers have proved fairly reliable over the 1989-95 period, with occasional replacement of broken parts and regular servicing every winter to remove dust from optical components and tune the position sensitive frequency doubling crystals.

3.3.2 The Beam Transport System

The beams travel down a complex 15m path from the top of the detector before reaching the TPC as shown in Figure 3.3. All mirrors are manually adjustable and are used to align the beams roughly each year after the winter servicing. Fine tuning is achieved via a computer controlled steering system located in the actuator box.

Once the laser light reaches the splitter ring shown in Figure 3.4 the beams are split into 3 and reflected into the TPC at angles in ϕ of 84°(96°), 204°(216°) and 324°(336°) on side A(B). Note that looking at ALEPH from outside the LEP ring side A is on the right hand side in the positive z direction.

The beams pass through 15mm quartz windows into the TPC where they are reflected from a series of 5 semi-transparent mirrors glued to the inner wall of the detector. The mirrors are angled such that the beams seem to originate from the interaction point, as shown in Figure 3.3. After passing the final mirror the beams exit from windows in the far wall of the TPC where their position is monitored with diodes.

3.3.3 Beam Position Monitoring and Steering

The position of the beam has to be controlled to an accuracy of better than 1mrad in order to hit all of the mirrors and the 15mm exit window at the end of the 15m path length. Precision of this order is difficult to maintain over this distance when several adjustable mirrors are included in the system and the whole is subject to vibration and temperature fluctuation.

To overcome these problems the beam position is changed via a steerable mirror in the actuator box as shown in Figure 3.5. This allows movement in 2

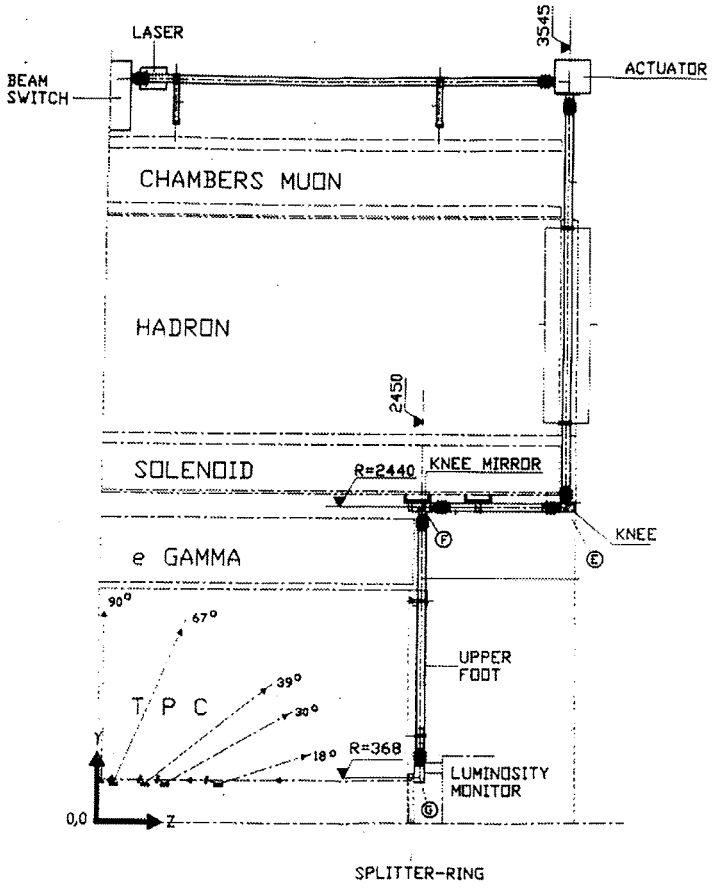

Figure 3.3: The beam transport system showing the 15m path length and the deflection angles of the mirrors in the TPC.

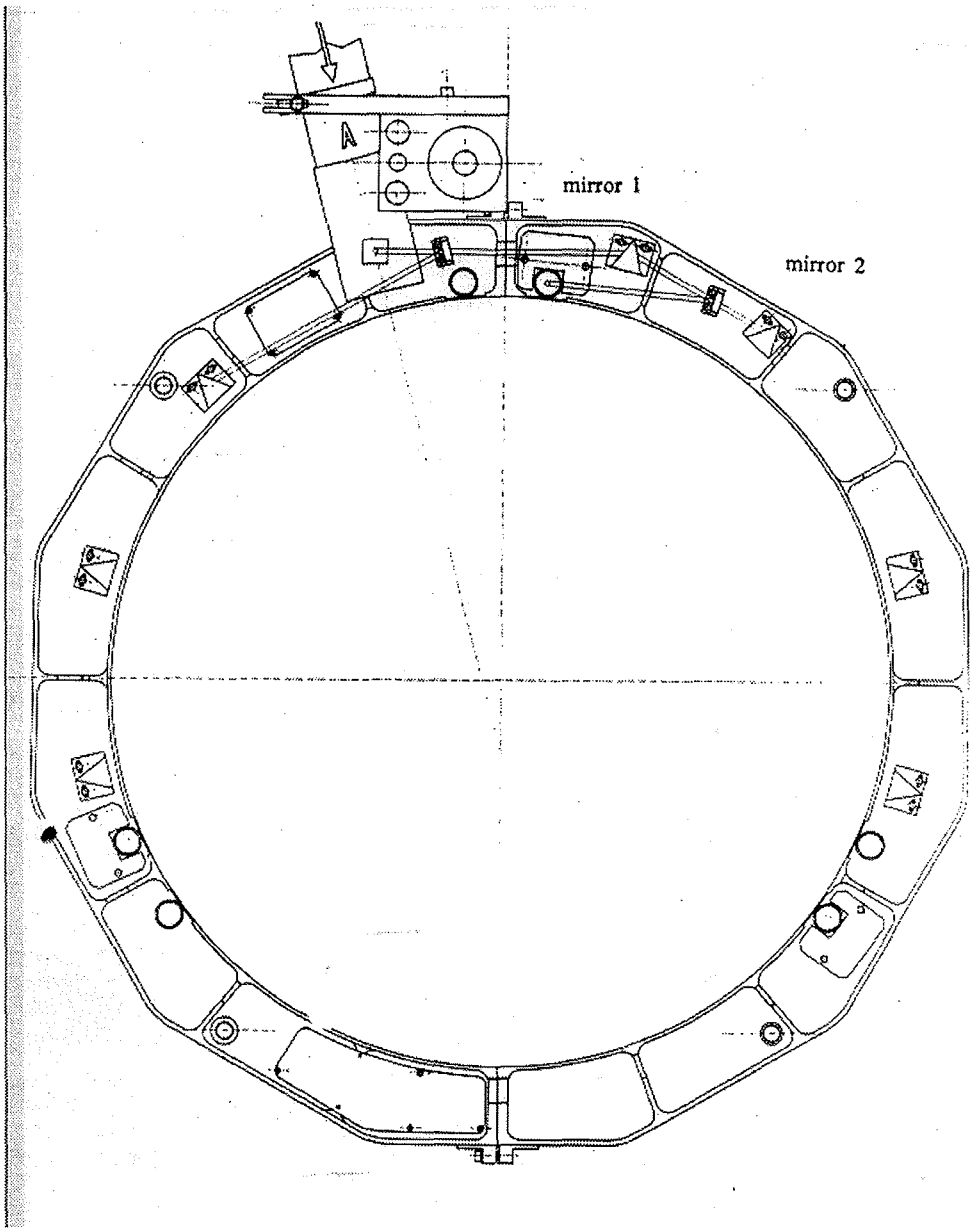

Figure 3.4: View down beam pipe of Splitter Ring showing windows to reflect beams into TPC. Diameter of Ring = 70cm.

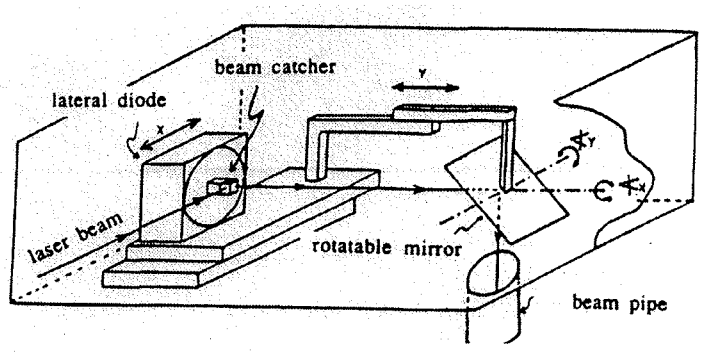

Figure 3.5: The Actuator Box showing stepper motors and steerable mirror.

translational and 2 rotational directions to reproduce all 4 degrees of freedom of the beam. The system is operated by a computer algorithm which uses as input the beam position as monitored by 5 photo-diodes on each side. These are located at each exit window in the TPC wall, at the beam coupler into the splitter ring as shown in Figure 3.6 and in the actuator box. The diode in the actuator box monitors the position of the light reflected back from the semi-reflecting mirror in the beam coupler and sits at a path length roughly equivalent to the centre of the TPC.

The diodes and steering motors are controlled by dedicated electronics modules located in barracks beside the detector. These communicate via standard protocols with the online computer cluster which runs the control tasks for the lasers and steering system.

It is important to note that the elements of the beam transport system beyond the actuator box are in general inaccessible during LEP's operational period from around May to November each year. It is possible to reach all elements of the system only during the long winter shutdown when opening of the detector endcaps and removal of the LCAL and SiCAL facilitate access to the splitter rings. This places a stability requirement on the system; any beam position fluctuations over the year should be small enough to allow compensation by the steering system.

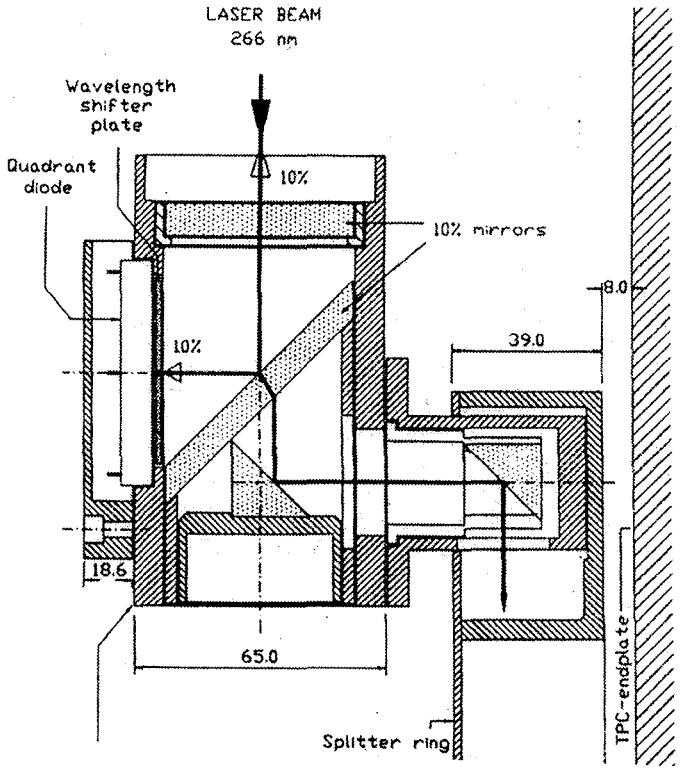

Figure 3.6: The Beam Coupler into the Splitter Ring showing the position sensitive quadrant-diode and reflected/transmitted beam. All measurements are in mm.

3.4 Principle of Field Distortion Correction

The drift velocity of electrons in a gas in the presence of an electric and magnetic field is given by the Langevin equation [19]:

$$\vec{v} = \frac{\mu}{1+(\omega\tau)^2}\left[\vec{E} + \omega\tau\frac{\vec{E}\times\vec{B}}{B} + (\omega\tau)^2\frac{(\vec{E}\cdot\vec{B})\vec{B}}{B^2}\right]$$

where μ $(= e\tau/m)$ is the electron mobility, $\vec{E}$ is the electric field vector, $\vec{B}$ is the magnetic field vector, τ is the mean drift time between collisions, ω $(= eB/m)$ is the cyclotron frequency , and $\vec{v}$ is the electron drift velocity. The product $\omega\tau$ has been determined in Reference [13] to be 8.9 ± 0.3 for the ALEPH TPC.

In a perfect TPC the electric and magnetic fields are exactly parallel and the above equation simplifies to $\vec{v} = \mu\vec{E}$. However small angles between the two are introduced by irregularities in the fields and by any tilt of the TPC inside the solenoid. Reference [20] demonstrates that the small tilt found in ALEPH is accounted for correctly.

A magnetic field map, taken prior to the start-up of the experiment [21], is used in conjunction with the straightness of reconstructed laser tracks to correct for any distortions. A detailed explanation of the method is given in Reference [18]; an outline is provided below.

The azimuthal symmetry of the detector suppresses field distortions in this direction. Significant radial components of the fields are, however, possible which can cause shifts in both the radius and azimuth of reconstructed tracks.

These are corrected during offline reconstruction using laser data. Stand-alone laser runs consisting of around 100 laser events are taken with the magnetic field on and off. The laser beams are reconstructed in the rz plane and the deviations between full and zero magnetic field are calculated. Combining the shift in the z direction with the known angle of the beam, the radial shift $\Delta_r(B) = r(B) - r(0)$ can be derived. From this we also obtain information about the azimuthal shift.

These corrections are important as they completely remove deviations that can shift the reconstructed momentum of a 45 GeV/c track by 5%.

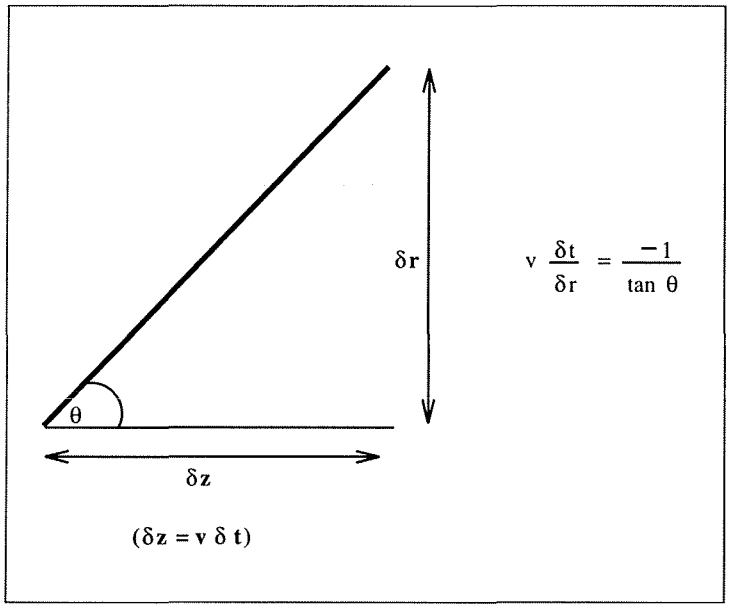

Figure 3.7: The relation between drift velocity and track angle.

3.5 Principle of Drift Velocity Calculation

The Laser System also allows us to measure the drift velocity of electrons in the TPC gas. Constant monitoring of this is necessary as the velocity is sensitive to changes in gas composition and pressure. Recall from above that $\vec{v} = \mu\vec{E}$ and that the electron mobility, $\mu = e\tau/m$ where τ, the mean time between collisions is inversely proportional to the pressure of the gas. Thus the velocity is proportional to $\vec{E}/p$. The TPC gas is maintained at a constant 7mbar over-pressure with respect to outside and so follows any fluctuations in atmospheric pressure.

The radial dependence of the drift time, t of a track is related to its polar angle θ by dt/dr = -1/(v tanθ) as shown in Figure 3.7. Large systematic effects due to sector alignment and electronic delay variations are cancelled by taking time differences with respect to a reference beam in each ϕ plane, allowing considerable accuracy to be achieved. The main element of the drift velocity, v_z is then given by:

$$v_z \frac{d(t_1-t_2)}{dr} = \frac{1}{tan\theta_2} - \frac{1}{tan\theta_1} - p_\phi \left[\frac{1}{sin^2\theta_2} - \frac{1}{sin^2\theta_1} \right]$$

where t_1, t_2 are the measured drift times of two beams, θ_1, θ_2 are the known angles of the mirrors deflecting the beams into the chamber and p_ϕ is a free parameter for each azimuthal plane to compensate for uncertainties in the steering of the beam in that plane. Further details are contained in Reference [18].

A minimum χ^2 fit is performed for the drift velocity with the p_ϕ as free parameters. The accuracy attained is detailed in Section 3.7.2.

3.6 LEP I Mode of Operation

During LEP I the Laser System was used every two weeks to check the drift velocity and occasional runs were taken with the magnetic field on and off to monitor the evolution of field distortions.

In addition a dedicated run was taken at the start of each year to find the maximum value of the drift velocity as a function of the TPC drift field High Voltage as shown in Figure 3.8. These were performed to place the velocity in a plateau region and thus minimize sensitivity to any fluctuations in pressure. The source of the plateau is the Ramsauer-Townsend effect by which electrons of a certain energy can pass through a rare gas without being significantly scattered [22].

It should be noted that the laser runs provided a back-up check for the main calculation of the drift velocity. This came from the analysis of hadronic events where the trajectories of reconstructed tracks in the TPC were combined with knowledge of the beam crossing time to allow the drift velocity to be calculated. This step was performed during a preliminary look at the data before the full reconstruction and is thus referred to as the 'Pass 0' result. The technique requires the tracks from both sides of the detector to come from a common interaction point. A minimum χ^2 fit for the velocity is performed by averaging over all of the events in a data run with this constraint.

All of the laser runs were taken in stand-alone mode with the TPC operating separately from the rest of ALEPH. For this purpose a dedicated data acquistion program was available for recording laser data. Side A and B provided data one

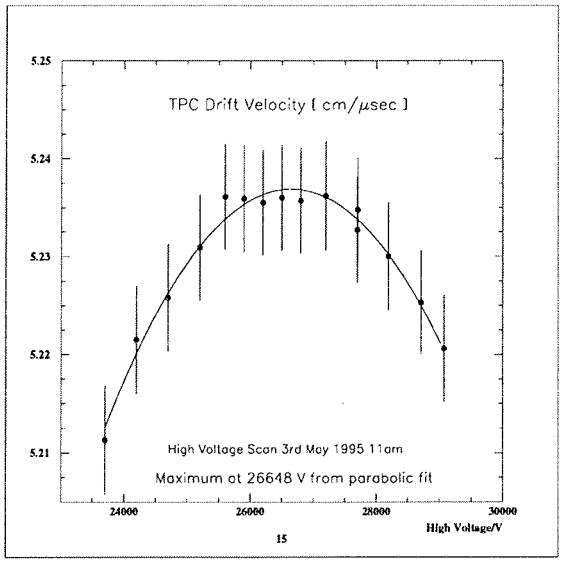

Figure 3.8: 1995 TPC Drift Voltage Calibration.

after the other because of differences in the trigger for each laser and the need to manually optimize the laser energy to produce good ionization. The steering of the beams also had to be tuned and in recent years operation of the data acquisition routine required increasing time and effort due to various problems with the original code. In general it was considered to be unreliable and incapable of unsupervised operation.

After the data acquisition task had successfully finished, a drift velocity calculation was performed and the result stored in private files.

One of the main difficulties with the Laser System during LEP I was a loss of alignment which the steering system could not recover. This happened on Side A on several occasions, leading to a complete loss of function for long periods. Unfortunately no Side A data was available for much of 1994 because of this difficulty. The problem was traced to a combination of limited acceptance in some sections of the optical path and instability in the optical components, particularly the exposed outer mirror knee.

3.7 New LEP II Project

At LEP II the Laser System changes from being an important but secondary part of ALEPH, to being integral to the operation of the detector. This means providing laser events during normal data taking and running the system 24 hours a day.

During the period from January to October 1995 I coordinated a project to upgrade the Laser System to meet these new demands. In this I collaborated with Eric Rohne of Mainz University and Lee Curtis of Glasgow University. The work involved improvements to the beam transport system and a complete re-write of all laser control software. The trigger system of the lasers also was changed to allow both of the lasers to fire simultaneously. The new requirement of constant running and reliability prompted us to introduce automated energy steering and beam position monitoring, along with fault reporting and diagnostic information in an expert system capable of responding to most situations.

3.7.1 Aims

The improved system had to meet several clearly defined criteria.

- No deterioration in the TPC tracking should occur as a result of the new method of finding the drift velocity.
- Field distortion data should be available as before.
- Both lasers should fire simultaneously to allow information from both sides to be obtained with a single readout of the TPC.
- The laser trigger signal should be passed to the ALEPH trigger system to synchronize readout of the detector.
- The result of the drift velocity calculation should be integrated into the ALEPH run records to allow use in track reconstruction algorithms.
- The above aims should be met in a robust and reliable system capable of operating for long periods without manual intervention.

The following Sections contain an explanation of the steps taken to meet these targets.

3.7.2 Accuracy

The drift velocity influences the accuracy with which the z coordinate of tracks can be reconstructed. At present the dominant systematic error in this measurement is due to unknown electronic timing variations from channel to channel which lead to the quoted uncertainty of around 1mm. If we express this as a fractional error by recalling that the total TPC drift length per side is 2.2m we obtain a value of 5 x 10^{-4}.

This figure is combined with the resolution in r and the statistical improvement from averaging the 21 pad hits to give an error on the measurement of the polar angle of 6 x 10^{-4}. The accuracy which the Laser System must achieve in order to avoid increasing this uncertainty is thus defined to be 1 x 10^{-4}. It is also important that the result be independent of changes in the beam steering and other external factors.

For comparison purposes the old Pass 0 method achieved an accuracy approaching 2 x 10^{-5}. During the commissioning period in mid 1995 both the Pass 0 and Laser Systems ran in parallel and the old method was used as a consistency check on the laser result.

In order to achieve the required precision a minimum of 300 laser events would be needed in each data run. Given that a run typically lasts 2 hours this requires a laser trigger rate of 50mHz. The small increase in detector dead-time this causes was deemed acceptable by the Collaboration.

The accuracy finally attained is shown in Figure 3.9 which compares the Pass 0 result with the laser one for all runs in September 1995. It shows that the widest deviation between the results is less than the required 1 part in 10^4 and that the average deviation is much smaller than this. Note that the figure contains two kinds of plot; the top pair show results calculated without any steering correction and demonstrate the importance of this effect by comparison with the bottom

pair which have been corrected. Similar plots exist which demonstrate that the result is insensitive to using information from only one side instead of both, and to changing the beam alignment between runs.

3.7.3 Trigger

The laser trigger was changed to produce pulses from both lasers simultaneously and to synchronize with the 6 μs decision window of the ALEPH Level 1 trigger. The arrangement before 1995 was for dedicated laser runs to record data from each side of the TPC separately and for the TPC to be read out independently of the rest of the detector. The new setup required the possibility of operating both in this stand-alone mode and in step with the ALEPH trigger.

In order to remain in time with ALEPH the new shots during data trigger had to be synchronized with the early beam crossing (EBX) signal from LEP. This is produced every 22 μs to warn of an imminent bunch crossing and requires downscaling to produce laser events at 20 second intervals. The trigger for stand-alone laser runs was incorporated into the scheme by replacing the EBX with a signal from the TPC clock module.

The pulse from the downscaler is passed to logic units which produce three output signals. The first triggers the Laser A Flash Lamp, the second does the same for Laser B and the final one produces a common Pockels Cell trigger which releases the accumulated radiation from both units in two simultaneous pulses. Small differences in construction mean that the optimal time between firing the Flash Lamp and releasing the Pockels Cell is not the same for both lasers. To accommodate this asymmetry Side A has a delay of 180 μs between the two triggers while the Side B period is 200 μs. Figure 3.10 shows the details of the timing.

External control of the trigger is achieved through the fact that many of the electronic modules in the system are programmable and can be operated by software from the online cluster.

The recording of a laser event by ALEPH is initiated many LEP cycles after

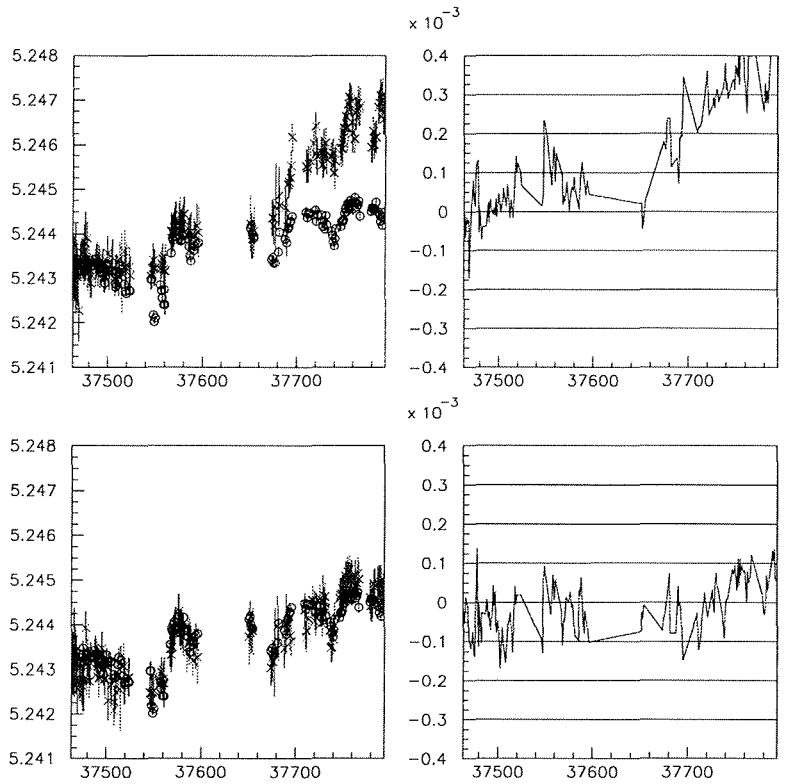

Figure 3.9: Left hand plots show laser (*) and Pass 0 (o) drift velocity values in cm/μs for runs during September 1995. The right hand plots show the difference between the two values in the form (Pass 0 - Laser) / Pass 0. The bottom plots have the steering correction applied while the top plots do not. The y-axis represents time but is calibrated using ALEPH run numbers.

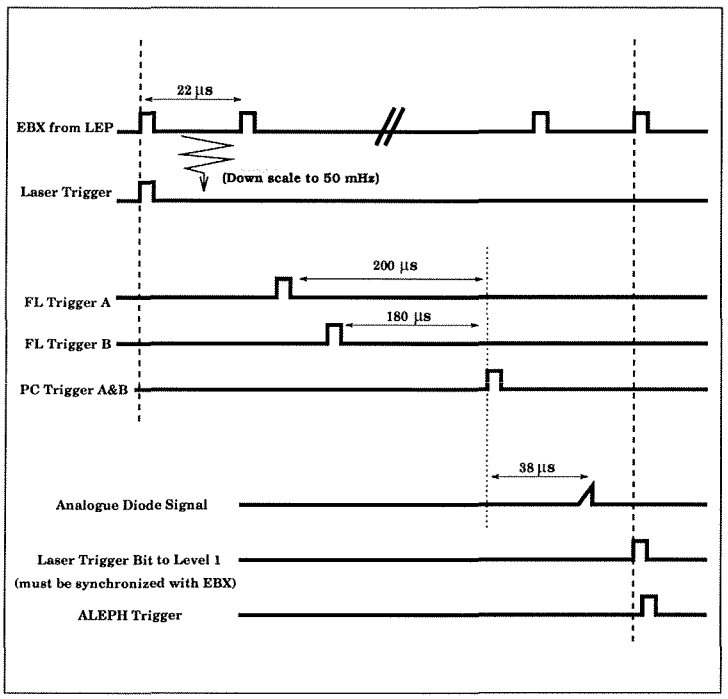

Figure 3.10: The timing of the new 'shots during data' Laser Trigger.

the signal that began the process. Approximately 40 μs after the Pockels Cell trigger a signal is received from the Splitter Ring diode on Side A or B which confirms that the lasers fired correctly. After applying a small delay to ensure it arrives within the 6 μs decision window this signal then passes to the Level 1 trigger and initiates readout of the whole detector.

3.7.4 Beam Transport

The problems with beam transport mentioned in Section 3.6 were traced to instability in the Side A outer mirror knee and limited acceptance at some points in the optical path. The acceptance problem has been successfully tackled over the last 2 years with the progressive removal of magnetic materials close to exposed areas of the path.

However even after these operations a major problem remained throughout 1994. It is believed that this was caused by the outer mirror knee being forced into a bi-stable position during the alignment procedure. The clearance between

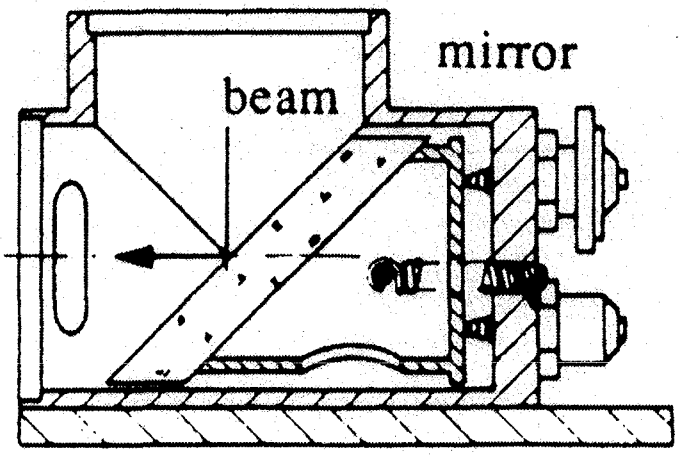

Figure 3.11: The Outer Mirror Knee.

the mirror casing and the mirror is very small and allows only limited angular movement as shown in Figure 3.11.

During the manual alignment at the start of the year it is thought that the adjustment screws forced the mirror knee against the casing and into an unstable position, leaving it vulnerable to disturbance. At some point during the year the mirror slipped into an undefined position with irrecoverable loss of alignment.

The temporary solution of reducing the mirror size by grinding the edges was implemented in April 1995. This allowed manual alignment to proceed without forcing the mirror against the casing and allowed trouble free operation throughout the year. To solve the problem in the long term new mirror knees with greater angular freedom were commissioned from Mainz University and installed in early 1996.

The solutions that were found to these and other problems have been compiled in a manual to assist future laser experts. It contains protocols for the regular operations performed each year and suggestions for diagnostic procedures in all areas of the system. The format of the document was designed to encourage progressive updating as new knowledge is gained. It is hoped that this will reduce the annual loss of expertise suffered when students leave the experiment.

3.7.5 New Laser Control Task

A new laser data acquisition task was written to run as part of the ALEPH DAQ. This controlled the energy, triggering and beam position of the lasers to provide laser events whenever the detector was recording data.

The new program employed the Finite State Machine (FSM) logic which ALEPH uses to describe the various states of the detector as explained in Reference [14]. In this framework tasks are programs which detail how to make transitions between states. Each sub-detector is controlled by a separate task and a central 'run-controller' program ensures that they all make transitions together.

One of the difficulties in developing the new routines was that the previous code used an erroneous protocol to communicate with the control modules of the diodes and steering motors. Once the correct procedure had been implemented it became possible to develop algorithms which were robust. The fact that the problem lay at such a fundamental level made it necessary to rewrite all of the laser software.

Fault reporting structures were integrated into the new task, encouraging the use of automatic recovery procedures when problems occurred. This evolved into an expert system which could eventually deal with all of the reproducible difficulties encountered by the system. In the event of new problems and the automatic recovery failing, diagnostic information was relayed to the ALEPH Shift Leader who would then contact the laser experts for help.

The new task monitored the alignment of the beams and made steering improvements when requested. It also performed actions on the appropriate laser triggers in step with the ALEPH run-controller, and regularly checked the beam energy making adjustments to provide good ionization levels in the TPC.

During the development of the new functionality a 'Test' state was introduced into the FSM structure which simulated thousands of hours of normal running by making intensive transitions between real states. The success and failure rate of the various procedures in the transitions were recorded and exported at the end of operation in the form of efficiency plots which were used to pinpoint weaknesses

in the techniques being used.

3.7.6 New Laser Monitoring Task

A separate task was implemented to process the laser events, calculate a value of the drift velocity and then pass it on to the ALEPH tracking algorithms. This was the responsibility of Eric Rohne who introduced improved beam reconstruction algorithms and steering corrections that allowed accurate calculation of the drift velocity.

In addition both tasks contain monitoring software written by Lee Curtis which integrates the beam energy and position monitoring with the standard ALEPH presenter used for diagnostic histograms. This allows TPC coordinators who may be unfamiliar with the details of laser operation to check on the general performance and call the attention of the experts to any new developments.

3.7.7 Conclusion of New LEP II Project

The project began in February 1995 and the new task to produce laser events interleaved with ordinary data was implemented in June. At the end of August the drift velocity calculation task was successfully introduced and it was verified that the required drift velocity precision of 1 part in 10^4 had been achieved. The system ran without major intervention from June till the end of the year demonstrating that it was reliable and robust. In this way all of the aims set out in Section 3.7.1 were met on schedule and in time for the start of LEP II in October 1995.

3.8 Conclusion

The upgrade of the Laser System for high energy running has been a clear success. The development of a new way of measuring the TPC drift velocity without degrading the tracking performance and simultaneously maintaining control of field distortions is a significant contribution to ALEPH's operation in the demanding

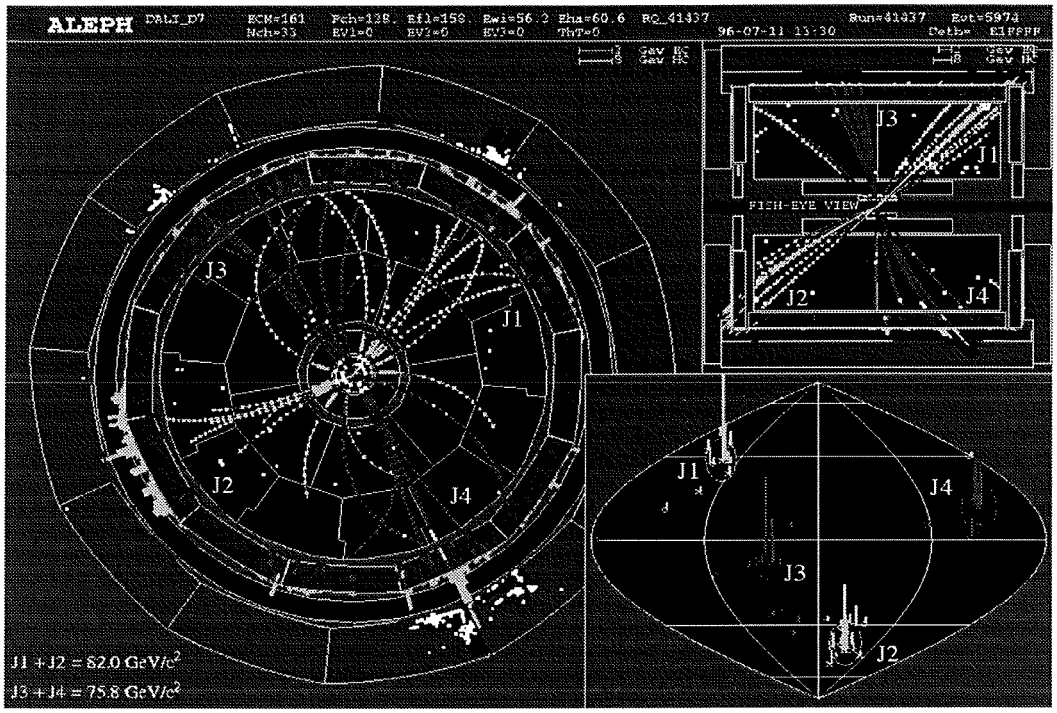

Figure 3.12: The First WW Event recorded by ALEPH.

conditions of LEP II. Figure 3.12 shows the first W^+W^- event recorded by the experiment in this new environment.

The author's other Collaboration responsibilities during 1995 included working as a TPC Coordinator, chairing a Parallel Session at a 'Collaboration Week' in October and making a presentation to the Plenary Session there.

Chapter 4

Method

The following Chapters of this thesis present a direct measurement of the Colour Factors of the strong interaction using a combination of new techniques.

After outlining the motivation for a more accurate evaluation of the Colour Factors, the principle used to make the measurement is explained. The remainder of this Chapter gives an overview of the analysis structure and details the event selection methods.

The topics of jet finding and parton to jet association are presented in Chapter 5, followed by an explanation of the technique used to select heavy flavour quark jets in Chapter 6. Chapter 7 presents the fitting method with a full error analysis, and Chapter 8 summarizes the relevance of the result in the context of the current understanding of strong interaction physics.

4.1 Introduction: Colour Factors in 4 Jet Events

The Colour Factors were introduced in Section 1.3.4 and to a good approximation can be thought of as denoting the relative strength of the three classes of quark and gluon vertex shown in Figure 4.1.

The three processes contribute at tree level to the cross-section for hadronic decays of the Z^0 to four jets. The principle of the measurement is that each process contains a different spin structure leading to characteristic angular orientations of the partons. Simple variables using the angles between the jets have been

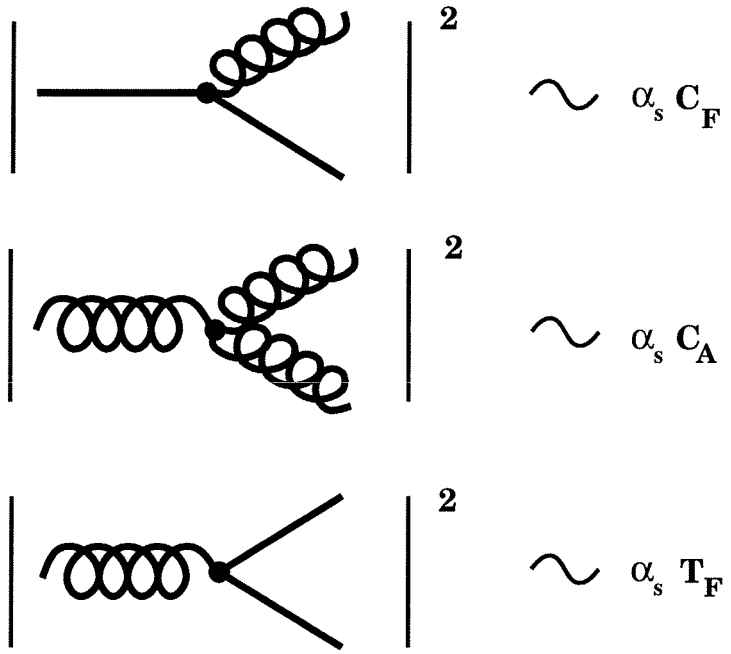

Figure 4.1: Intuitive relation between the three basic QCD processes and their associated Colour Factors.

developed to maximize sensitivity to these differences as explained in Section 4.3.

The experimental method consists of combining a measurement of the variables in hadronic Z^0 decays with $\mathcal{O}(\alpha_s^2)$ QCD predictions of how each process contributes to the total cross-section. A linear combination of the three contributions is then fitted to the data with the Colour Factors as free parameters.

For a general variable, y, the 4-jet cross-section can be expressed as the sum of three terms, each proportional to a Colour Factor.

$$\frac{1}{\sigma_{tot}}\frac{d\sigma}{dy} = (\frac{\alpha_s C_F}{\pi})^2[\alpha(y) + \frac{C_A}{C_F}\beta(y) + \frac{T_R}{C_F}\gamma(y)]$$

In this expression the association of each element to a specific process is complicated by the inclusion of interference terms. However we can make an intuitive link between the dominant direct processes. In this way the α function can be indentified with double gluon bremsstrahlung events, the β function with triple gluon vertex events, and the γ function with four quark events as shown in Figure 4.2.

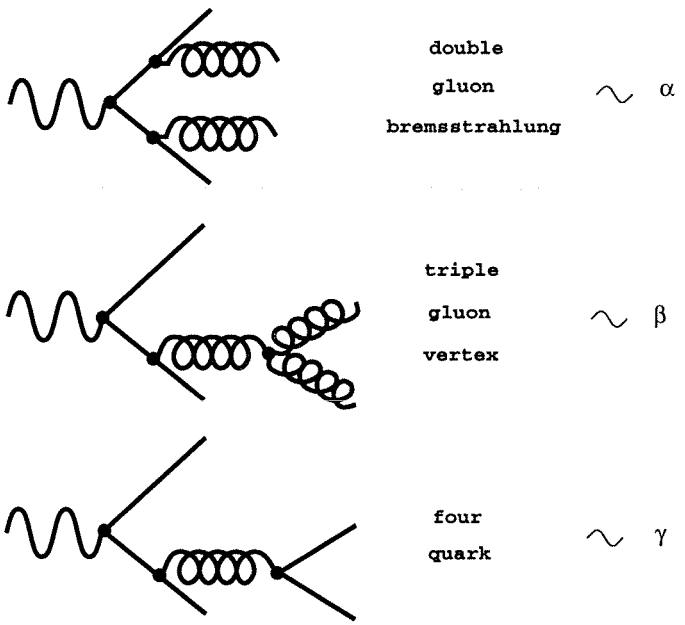

Figure 4.2: Tree level contributions to the 4-jet cross-section.

In practice the common $(\frac{\alpha_s C_F}{\pi})^2$ prefactor is absorbed into a freely varying normalisation parameter leaving us with access only to ratios of the Colour Factors. This is done in order to remove any dependence on α_s and the overall 4-jet rate which is expected to suffer from large higher order corrections as discussed in Section 7.3.2.

4.2 Motivation for Colour Factor Measurement

The experimental verification of QCD has reached an advanced stage with recent results from e^+e^- interactions at LEP complementing findings from other areas of high energy physics to present a coherent description of the available data. However, the group structure of the theory as expressed through the Colour Factors remains one of the most poorly established areas, despite being fundamental to identifying QCD as the theory of the strong interaction.

Recent theoretical interest in this area has centered on the possible existence of a supersymmetric spin $\frac{1}{2}$ partner to the gluon. In Reference [24] it is shown that the existence of a light gluino with a mass of ~3 GeV leads to greater

consistency between measurements of α_s at different energy scales. These effects are a consequence of the change in the number of strongly-interacting fermions, n_f, which increases by three above the threshold for gluino production. The number of fermions is directly related to the quantity $T_R = n_f T_F$ measured in this analysis.

The topic of gluinos is further explored in Reference [5] which shows the importance of lifetime and mass effects, while Reference [25] reviews current progress in experimental searches.

4.2.1 Colour Factors at LEP

The LEP accelerator provides an ideal testing ground for Colour Factor predictions for several reasons. Most obviously, the non-abelian nature of QCD as manifest in the triple gluon vertex (TGV) is directly accessible in this clean environment. Evidence from pp interactions [23] support the predictions of QCD in this respect but cannot provide the direct observation available in hadronic Z^0 decays.

The high energies available at LEP combine with the running of α_s to facilitate the application of perturbative methods, making theoretical predictions more accurate. The separation of this regime from the poorly understood non-perturbative energy range leads to a more straightforward correspondence between the measured jet properties and their parton initiators. This fact is critical to this analysis which relies on achieving a good resolution on the angles and energies of the partons.

Finally, the increased cross-section for e^+e^- annihilation at the Z^0 resonance has led to several million hadronic events being recorded by each of the LEP experiments, allowing a level of statistical accuracy previously unattainable.

4.2.2 Previous Measurements

The idea of exploiting the different angular orientation of the 3 classes of four-jet event was first proposed in Reference [26]. This paper introduced a variable

designed to maximize the difference between two of the classes, and was later complemented by further proposals designed to highlight the other contributions [27, 28, 30]. The four variables will collectively be referred to as Angular Correlation Variables (ACV's).

The LEP Collaborations began experimental investigations into Colour Factors by measuring combinations of ACV's in 4-jet events and performing qualitative comparisons of QCD with a toy model [40] containing no gluon self-coupling [30, 34, 32]. A similar analysis was performed on 4-jet data from e^+e^- interactions at an energy of 58 GeV at the TRISTAN accelerator [37]. All of these studies were limited by the small number of 4-jet events available but did produce evidence in support of QCD predictions.

The first quantitative Colour Factors measurement came from the ALEPH Collaboration using the distribution of invariant masses in 4-jet events [38]. This was followed by a measurement which exploited the Colour Factor dependence of the $\mathcal{O}(\alpha_s^2)$ corrections to the 3-jet final state [39] which was repeated by the OPAL Collaboration [36]. These results were complemented by a number of 4-jet analyses by the other LEP Collaborations using ACV's to make direct measurements of the Colour Factors [31, 33, 35].

In summary, the current experimental position leaves the Colour Factors known to limited accuracy and remains one of the least well established areas of the Standard Model. It also represents an opportunity to test this fundamental prediction of perturbative QCD.

4.2.3 Primary Quark Tagging and Colour Factors

This analysis exploits the ability of ACV's to differentiate between different four parton processes to produce a direct high-statistics measurement of the Colour Factors. The work is performed in an area of phase space where the impact of two and three parton background events is negligible and non-perturbative effects are small as shown in the next Chapter.

The Angular Correlation Variables employed in this analysis rely on energy

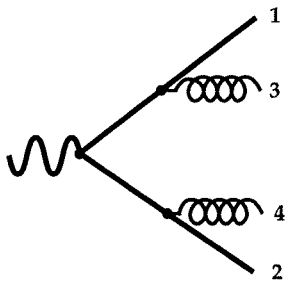

Figure 4.3: An example of energy ordering applied to a double gluon bremsstrahlung event in which the two highest energy partons are the primary quarks. The numbers refer to the energy order of the jets with the hardest being in position 1.

ordering of the four jets to pick out the initial $q\bar{q}$ from the secondary partons, as explained in the next Section. Figure 4.3 shows an example of the favoured configuration of $q\bar{q}$ in position 1 and 2. For the dominant qqgg process, however, this technique succeeds in only $\sim$ 50% of events [40].

To overcome the problem of failing to pick out the correct primary quark jets and thus mis-measuring variables, this analysis exploits the heavy quark tagging capability of the ALEPH detector to label the quark jets directly in $b\bar{b}$ events. This allows the extra information contained in these events to make a substantial contribution to the accuracy of the measurement.

To facilitate this technique, the 4-jet sample is divided into a b-tagged component passing the selection criteria detailed in Chapter 6, and an anti-tagged component containing light u,d,s & c quark events. The overall accuracy is maximized by combining the results from each sample in the final result.

The udsc sample, as it shall be referred to, is compared with $\mathcal{O}(\alpha_s^2)$ QCD matrix-element predictions of the 4-jet cross-section which assume that parton masses are negligible [41]. In the tagged sample the large b quark mass of 5 GeV cannot be ignored as it leads to considerable distortions of the shape of the ACV's. For this sample a new calculation to $\mathcal{O}(\alpha_s^2)$ which includes the quark masses is used [42].

This analysis represents the first use of heavy quark tagging to increase the accuracy of ACV's and also the first use of a massive matrix-element calculation to make a Colour Factor measurement. The combined use of tagged and anti-tagged samples is also novel, as is the use of ACV's to analyse the ALEPH data.

4.3 Angular Correlation Variables

Angular Correlation Variables are designed to be sensitive to different classes of 4-jet event through the characteristic jet orientations which arise from the underlying parton spin structure.

Differentiation between double gluon bremsstrahlung events and other classes relies on the fact that the cross-section for single gluon emission by a quark-antiquark pair strongly favours collinear radiation of the gluon with respect to the quark direction. The cross-section [44] is shown below using the conventional definition of the scaled parton energies, $x_q = \frac{2E_q}{\sqrt{s}}$, $x_{\bar{q}} = \frac{2E_{\bar{q}}}{\sqrt{s}}$ and $x_g = \frac{2E_g}{\sqrt{s}}$. Energy conservation requires that $x_q + x_{\bar{q}} + x_g = 2$.

$$\frac{1}{\sigma_{had}} \frac{d\sigma}{dx_q dx_{\bar{q}}} = \frac{2\alpha_s}{3\pi} \frac{x_q^2 + x_{\bar{q}}^2}{(1-x_q)(1-x_{\bar{q}})}$$

This function is displayed in Figure 4.4 in which the collinear singularities as $x_q \to 1$ and $x_{\bar{q}} \to 1$ are clearly visible. In double gluon bremsstrahlung events collinear emission leads to a characteristic 2-jet like structure which is not observed in the other classes of 4-jet event.

Variables which attempt to differentiate between four quark and triple gluon vertex events exploit the fact that the virtual gluon is highly polarised in the event plane.

If $d\sigma_{||}$ and $d\sigma_{\perp}$ denote the cross-sections for gluon emission in and perpendicular to the event plane, the gluon polarization is defined as

$$P(x_q, x_{\bar{q}}) = \frac{(d\sigma_{||} - d\sigma_{\perp})}{(d\sigma_{||} + d\sigma_{\perp})}$$

and from the gluon cross-section including the plane of polarization given in Reference [43] we then obtain

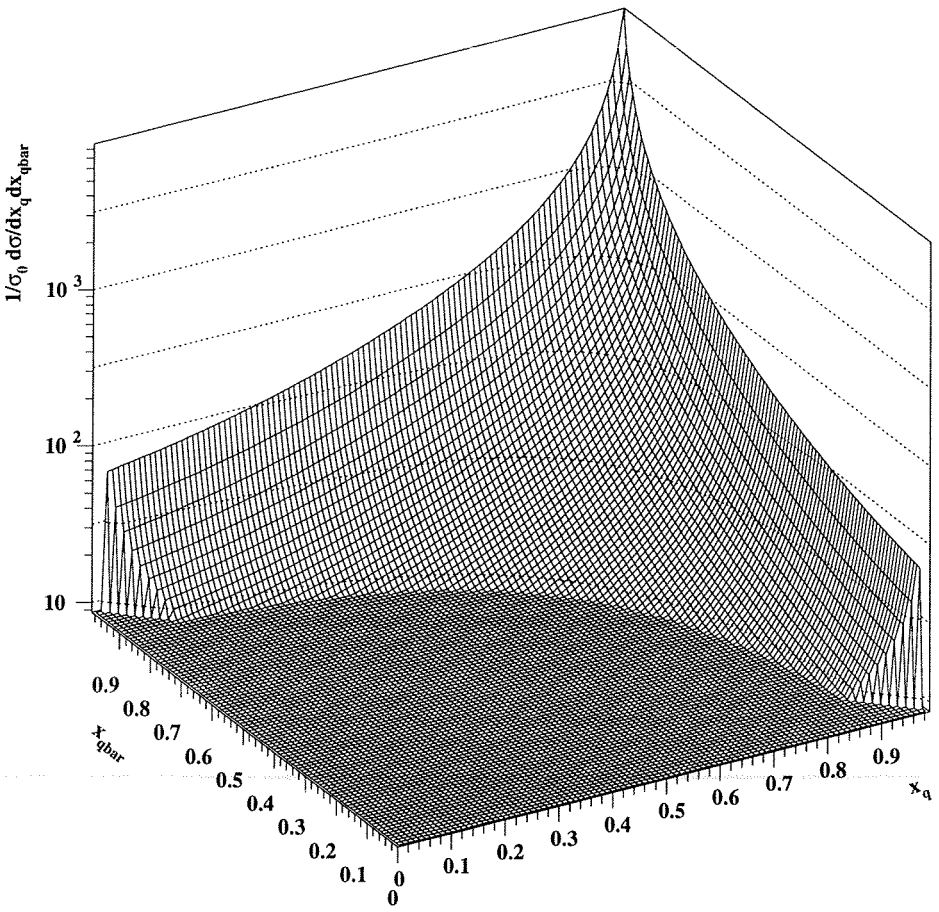

Figure 4.4: The $\mathcal{O}(\alpha_s)$ gluon emission cross-section expressed in terms of the scaled quark energies x_q and $x_{\bar{q}}$. Note that a log scale is used in the z direction, marked in arbitrary units.

$$P(x_q, x_{\bar{q}}) = \frac{2(1-x_g)}{x_q^2+x_{\bar{q}}^2}$$

which shows that the gluon tends to be polarized in the event plane except when $x_g \to 1$. This area of phase space is, however, strongly suppressed as we can see from Figure 4.4.

The gluon polarization vector defines a direction relative to which we can measure the angle of the decay products in TGV and 4 quark events. If this angle is denoted by χ, and the momentum fraction carried by one of the products by z, then quoting a fragmentation function result from Reference [29] which describes the orientation of this decay plane we find an azimuthal term which enters with opposite sign in the two cases:

$$D_{g\to gg}(z,\chi) = \frac{6}{2\pi}\left[\frac{(1-z+z^2)^2}{z(1-z)} + z(1-z)cos(2\chi)\right]$$

$$D_{g\to q\bar{q}}(z,\chi) = \frac{n_f}{2\pi}\left[\frac{1}{2}(z^2+(1-z)^2)^2 - z(1-z)cos(2\chi)\right].$$

This suggests an energy imbalance between the products of the $g \to gg$ process while $g \to q\bar{q}$ favours a more even split. Also, when we look at the azimuthal distribution we find that the decay to quarks tends to produce jets perpendicular to the polarization direction, while for decays to gluons, the two jets line up parallel to this direction. These preferred configurations are displayed in Figure 4.5. Note that the preceding expressions are derived for massless gluons. We assume that the virtual gluon in TGV and 4 quark events is close to being on shell in which case the same features will be apparent.

We now look at the definition of the angular variables to see how the principles introduced above can be exploited to measure the contribution of each process experimentally.

The Korner-Schierholz-Willrodt Angle :χ_{KSW}

The first variable is the Korner-Schierholz-Willrodt angle (χ_{KSW}) which is defined in Figure 4.6. It is designed to pick out the difference between double gluon bremsstrahlung and triple gluon vertex events through the correlation in TGV events that arises from the polarization of the intermediate gluon [26]. The

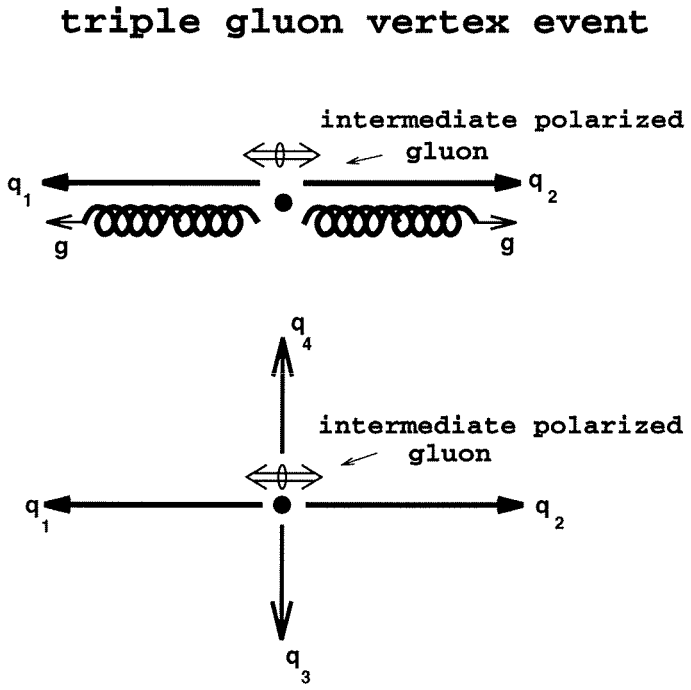

Figure 4.5: The top picture shows the preferred orientation of the decay products for the $g \to gg$ process. The lower picture displays the preferred $g \to q\bar{q}$ orientation. In both diagrams the virtual gluon is viewed head on with the polarization vector horizontal.

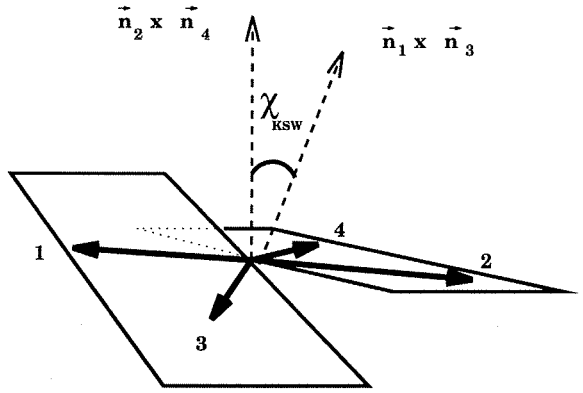

Figure 4.6: The Korner-Schierholz-Willrodt angle (χ_{KSW}) is given by the angle between the normals of the two planes defined by jets 1 and 3, and 2 and 4.

originally proposed variable included a requirement that each hemisphere contain two jets, with events possessing 3 jets in one hemisphere and 1 in the other being disallowed. Here the requirement is relaxed to allow the variable to be used in all events and the absolute value of the cosine of the angle was taken. This leads to some similarity in the appearance of the classes but the variables are measured with sufficient accuracy to overcome this as shown in Chapter 7.

The QCD matrix-element prediction for each ACV is shown in Figure 4.7 separated into the contributions from each class of event. In interpreting the form of the variables it should be remembered the cosine of the angle is plotted and that there is a requirement on the invariant mass between the partons to be above a cut of $y_{cut} = 0.01$ as explained in Chapter 5. It should also be emphasized that it is the relative change in shape for each process which demonstrates the differentiating power of a variable.

The Bengtsson-Zerwas Angle : χ_{BZ}

The Bengtsson-Zerwas angle (χ_{BZ}) is defined in Figure 4.8. It is designed to pick out the difference between qqgg and qqqq events through the different azimuthal orientations of the secondary partons as shown in Figure 4.5. The absence of an intermediate gluon in the double bremsstrahlung events leads to a uniform azimuthal distribution for χ_{BZ} and χ_{KSW}. The enhancement observed in both cases as $\cos(\chi)$ tends to one results from the residual tendency of the second gluon to lie in the plane defined by the other three partons as it is here that the Colour field is concentrated.

The Nachtmann-Reiter Angle : θ_{NR}

The modified Nachtmann-Reiter angle is defined in Figure 4.9 as a generalization of the original variable which can be applied to all 4-jet events [29]. It is designed to differentiate qqqq from TGV events via the orientation of the decay products in a similar way to χ_{BZ} but relies on a different spin effect [27].

The Opening Angle between Jets 3 and 4 : α_{34}

The final variable is the opening angle between jets 3 and 4. It was first

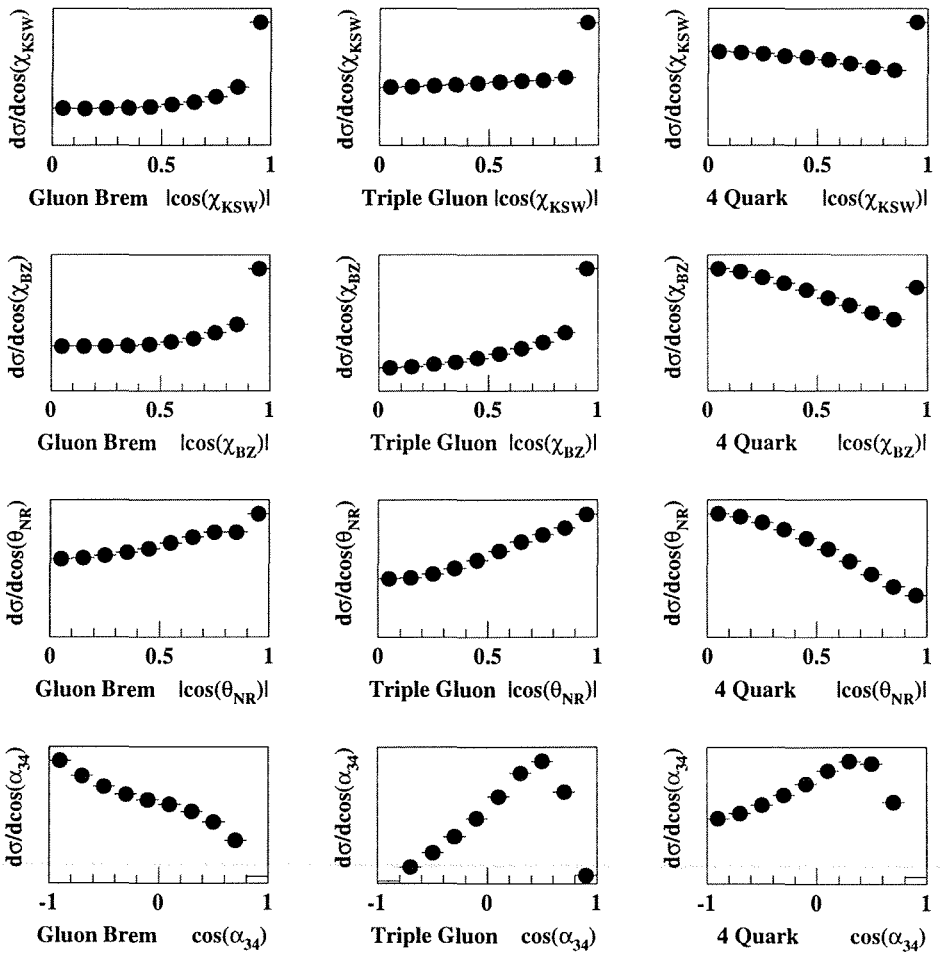

Figure 4.7: The above plot shows the $\mathcal{O}(\alpha_s^2)$ matrix-element prediction for the contribution of the three processes to each angular correlation variable. The analysing power of each variable is contained in the change in shape of the distribution for each process. To emphasize this the y axis is shown with an unmarked scale.

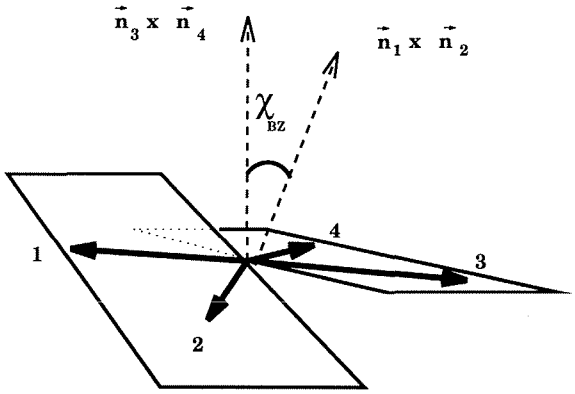

Figure 4.8: The Bengtsson-Zerwas angle (χ_{BZ}) is given by the angle between the normals of the two planes defined by jets 1 and 2, and 3 and 4.

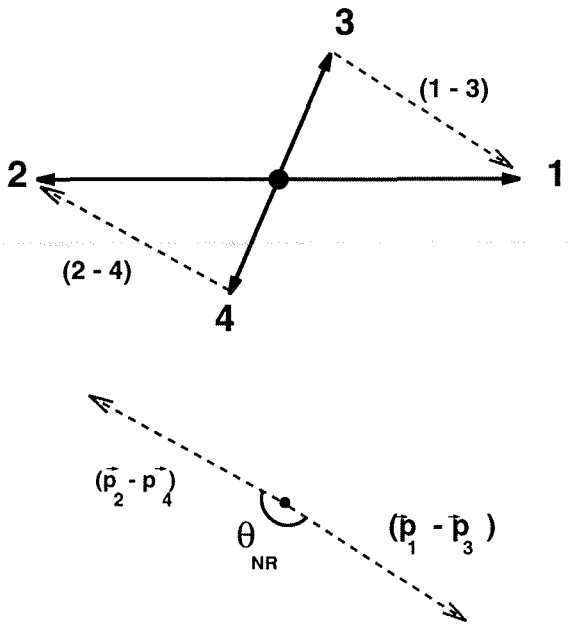

Figure 4.9: The Nachtmann-Reiter angle is defined as the angle between the 3-momentum differences $\vec{p}_1 - \vec{p}_3$ and $\vec{p}_2 - \vec{p}_4$.

proposed by the DELPHI Collaboration [30] and is sensitive to all classes of event but particularly to the gluon bremsstrahlung process where the secondary partons have a characteristic back-to-back orientation.

4.4 Monte-Carlo Studies

An important use of simulated data in High Energy Physics is to model the response of the detector to hypothetical events and thus derive a correction factor to compensate for irregularities. In this respect the accuracy with which the simulated data describes the real is of secondary importance to the quality of the detector simulation; the aim is to model the change in the event because of detector imperfections rather than the event itself.

In this analysis we must compare data with $\mathcal{O}(\alpha_s^2)$ matrix-element predictions which describe quarks and gluons. In reality however we do not observe partons but rather the jets of collimated particles they give rise to. This means we need to convert the jet distributions we measure into their parton equivalents. We derive such a correction function from MC distributions measured before and after the partons fragment to form jets.

In order to handle these effects correctly we need the hadronization process to be as accurately modelled as possible. In doing so we must take care to exactly reproduce the decays of heavy flavour particles, as the b-tagging techniques used later require knowledge of the tag performance measured in simulated data.

These demands cause us to place greater emphasis on the agreement between real data and data simulated using the Monte-Carlo principle, as this gives an indication of how well the hadronization and decay characteristics of the model describe reality. It should be emphasized that the process by which hard partons fragment to produce showers of final state particles is poorly understood and that Monte-Carlo routines attempt to describe it with phenomenological models. In this context the level of agreement observed between these models and the data is remarkable.

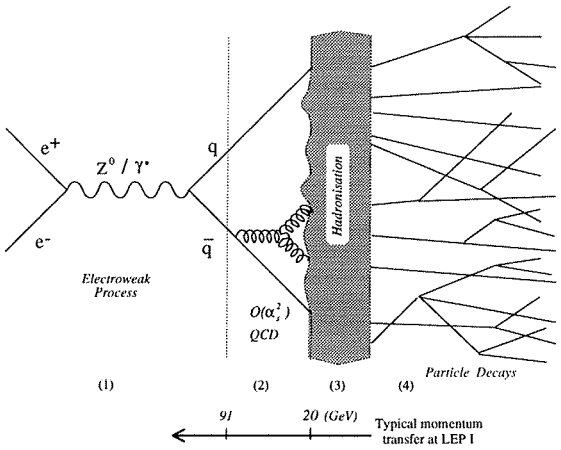

Figure 4.10: Schematic representation of a hadronic event as modelled by the matrix-element option in the JETSET Monte-Carlo.

4.4.1 The Matrix-Element Option in JETSET

In this analysis we use the JETSET Monte-Carlo [8] with the matrix-element option. This employs a parameterization of the full $\mathcal{O}(\alpha_s^2)$ matrix-element calculation to describe the production of the first four partons.

In this scheme the normal parton shower fragmentation procedure is turned off and the hadronization technique usually employed at the end of the shower is used to describe the evolution from the initial 4 partons down to the final state hadrons. The two alternative approaches are displayed in Figures 4.10 and 4.11.

The matrix-element scheme in JETSET is known to describe some features of the data less well than the parton shower version [45] but is nevertheless more appropriate for this analysis. As mentioned above we must compare data with 2^{nd} order QCD and the ability to identify each jet with its parent parton is required in order to derive the hadronization correction function.

In addition, the parton shower option only uses an $\mathcal{O}(\alpha_s)$ matrix-element to describe the first branching in the shower, and thereafter employs the leading-log approximation to describe the branching process. This does not describe the emission of high angle partons as well as the full matrix-element, and does not include the angular correlations which are fundamental to the description of the

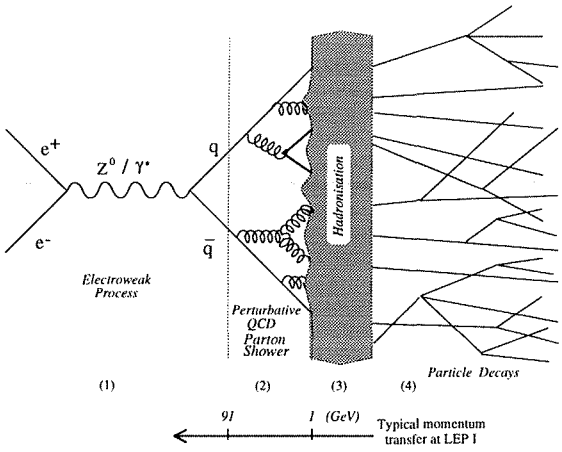

Figure 4.11: Schematic representation of a hadronic event as modelled by the parton shower option in the JETSET Monte-Carlo.

4-jet region. Subsequently we do not expect the parton shower option to do well in this area and it will not be discussed further.

It should be pointed out that the Monte-Carlo data shown here is derived using Version 7.4 of the JETSET program with the matrix-element option using a value of the QCD renormalization scale, μ, which has been chosen so as to best describe the ALEPH data [45]. It employs a standard set of hadronization parameters used by ALEPH including the radiation of initial state photons from the e^+e^- before annihilation and a detailed modelling of the decays of heavy flavour hadrons.

4.4.2 Comparison of Data with Monte-Carlo Predictions

The remainder of this Section is devoted to comparing distributions sensitive to the general features of Z^0 decays in real data with predictions from Monte-Carlo.

Note that matrix-element Monte-Carlo (MEMC) events usually contains 2,3 or 4 partons before hadronization, but the 4-jet selection procedure used here removes almost all 2 and 3 parton events leaving a contamination of less than 0.02% as explained in Section 4.5.3. In recognition of this fact most of the following plots are derived from 433,792 fully simulated MEMC events which contain

only 4 partons before hadronization (denoted the $MEMC_4$ sample). The plots in Figure 4.12 however come from a sample containing 139,163 events containing 2,3 and 4 partons (denoted the $MEMC_{234}$ sample). In both samples the simulated data goes through the full hadronization process and detector simulation and then the same analysis chain as the data before being compared with 3,675,851 uncorrected ALEPH Z^0 events recorded between 1992 and 1995.

Figure 4.12 shows distributions from the initial level of analysis when only basic hadronic event selection cuts have been applied. The data is compared to the $MEMC_{234}$ sample. In the plot of the total event multiplicity we can see that the $MEMC_{234}$ sample slightly under-estimates the number of neutrals by about one particle per event. The mean of the distributions are $< n >_{data}= 37.28 \pm 0.005$ and $< n >_{mc}= 35.80 \pm 0.024$.

Figures 4.13, 4.14, 4.16, 4.15 and 4.17 show distributions derived from events which have passed all 4-jet event selection criteria and been accepted as part of the final sample. Note that the b and udsc samples have been combined in these plots. At this stage we select 96,785 data events and 40,403 events from the $MEMC_4$ sample which satisfy all cuts.

In Figure 4.13 we see plots of variables sensitive to the overall topology of the event. To obtain the variables shown we must first define the momentum tensor for an event as

$$\mathbf{P_{ij}} = \sum_{\mathbf{n=1}}^{\mathbf{N}} \mathbf{\vec{p}_{ni}\vec{p}_{nj}}$$

where i,j = 1,2,3 denote the components in some coordinate system of the 3-momenta $\vec{p}$ of a particle and the sum over n includes all N particles in the event. If we denote the eigenvectors of this tensor as λ_i and normalize them such that $Q_i = \frac{\lambda_i}{\Sigma\lambda_i}$ then we define the quantities shown in Figure 4.13 as follows: Sphericity $= \frac{3}{2}(1 - Q_1)$, Aplanarity $= \frac{3}{2}Q_3$ and Planarity $= (Q_2 - Q_3)$. The agreement observed in these variables and in the polar angles of the jets shown in Figure 4.14 suggests that the shape of the events are reasonably well modelled by the Monte-Carlo.

In Figure 4.15 we see the momentum of all jets divided into longitudinal and transverse components relative to the jet axis. A softer P_T spectrum is observed in

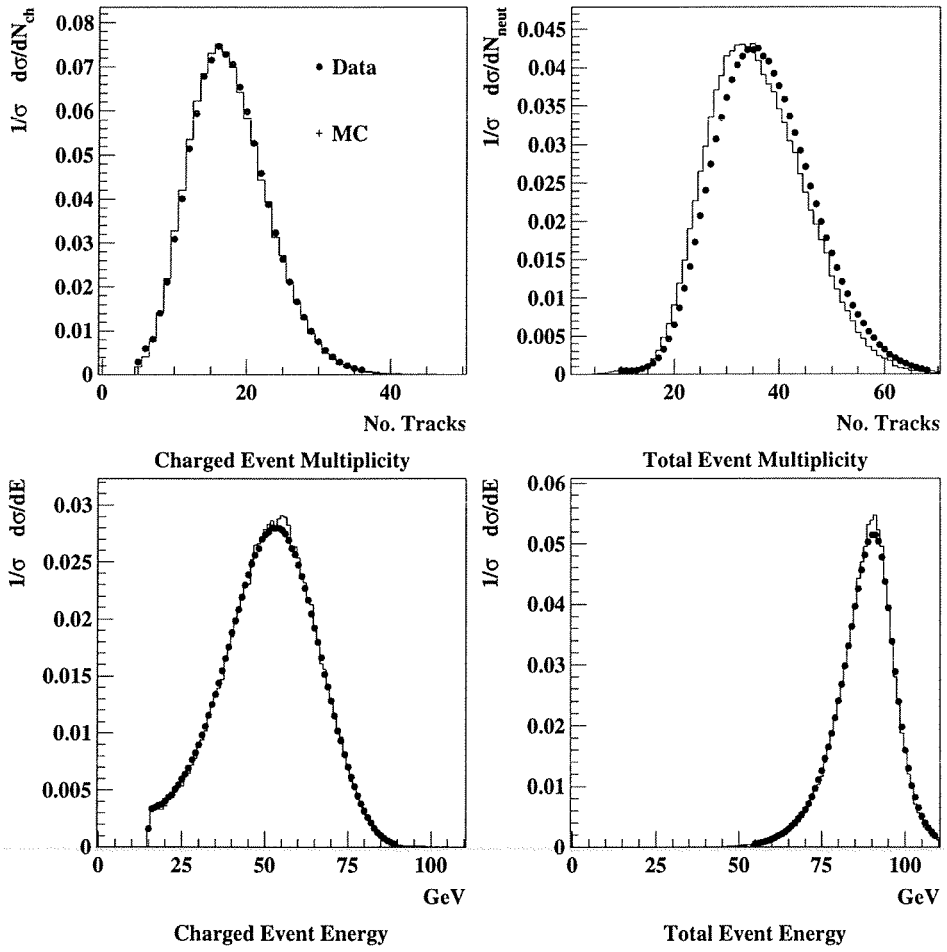

Figure 4.12: Comparison of ALEPH Data with MEMC_{234} predictions for the number of charged tracks and the total number of particles in events which pass the Hadronic Event Selection. The lower left plot shows the sum of the energy of charged tracks, and the lower right plot shows the sum of the energy of all particles (i.e. charged and neutral).

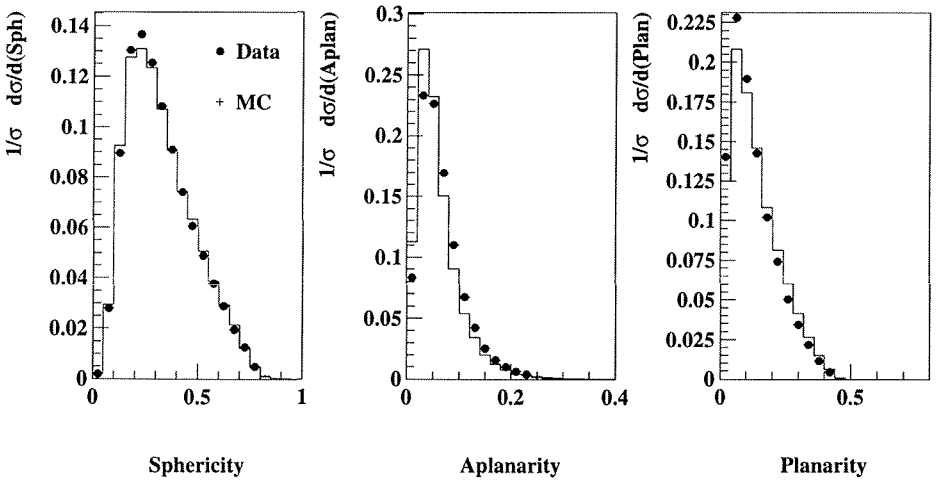

Figure 4.13: Comparison of ALEPH 4-jet Data with $MEMC_4$ predictions for 3 event shape distributions derived from the eigenvalues of the momentum tensor.

the MC sample ($< P_T >_{data} = 4.632 \pm 0.004$ GeV/c and $< P_T >_{mc} = 4.229 \pm 0.004$ GeV/c) and a harder P_L spectrum. When we examine Figure 4.16 we can see that these two effects cancel to give an accurate description of the total energy of the jet.

Figure 4.17 shows measurements of the energy of each particle and of the angle it makes with the jet axis. In the MC the neutral particle energy spectrum is slightly harder, supporting the interpretation of the $MEMC_4$ sample as containing a smaller number of higher energy neutrals than the data. Also the softer P_T spectrum of Figure 4.15 can be understood as an artefact of the slightly greater collimation observed in MC jets.

We conclude the comparison of data and Monte-Carlo with Figure 4.18 which shows the four Angular Correlation Variables used in the final analysis. The level of agreement between the two gives us confidence that the scheme used is appropriate to this analysis, and the slight discrepancy observed in some single particle distributions has little impact on the jet related quantities used.

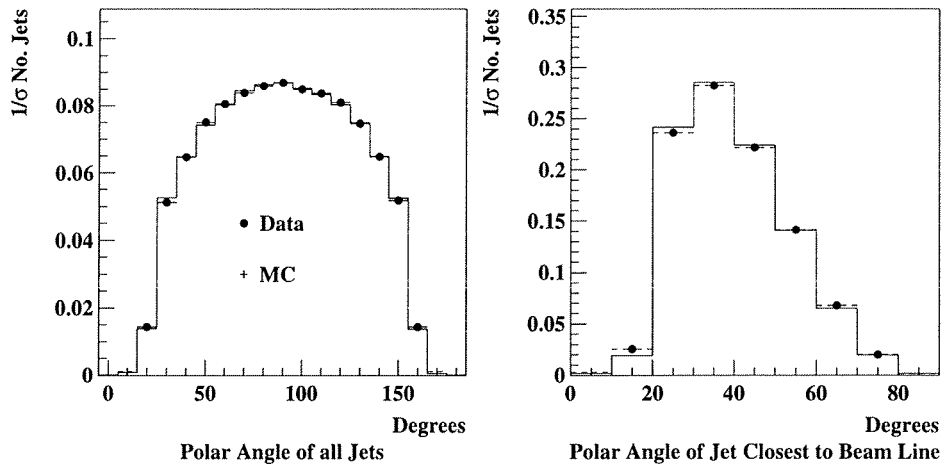

Figure 4.14: Comparison of ALEPH Data with $MEMC_4$ predictions for the polar angle of all jets in the 4-jet sample and the polar angle of the jet closest to the beam line in each event.

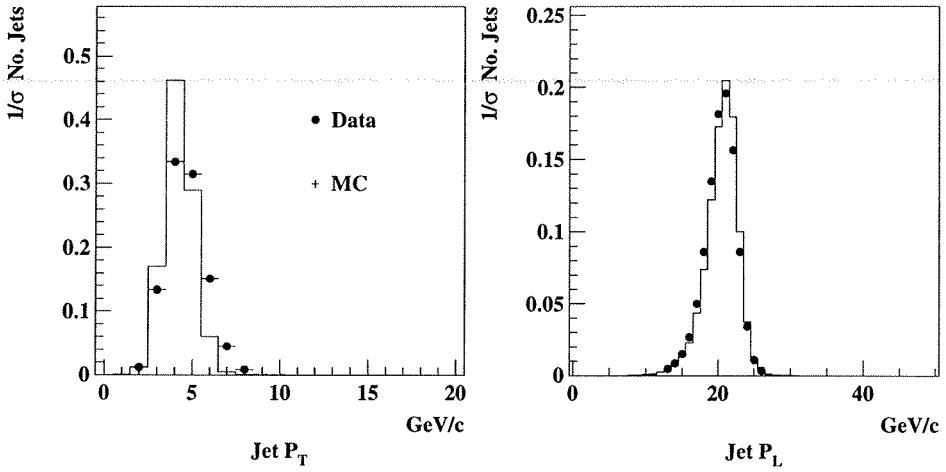

Figure 4.15: Comparison of ALEPH 4-jet Data with $MEMC_4$ predictions for the total longitudinal and transverse momentum of jets.

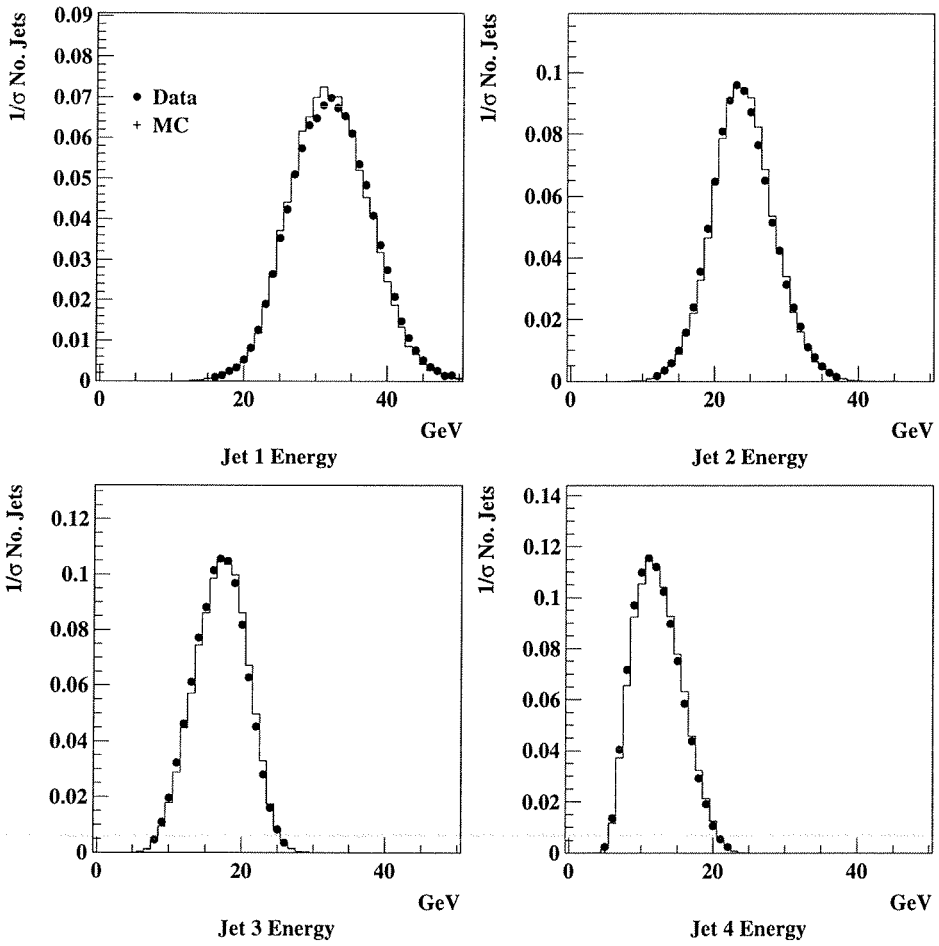

Figure 4.16: Comparison of ALEPH Data with $MEMC_4$ predictions for the energy of jets. In each event the jets have been numbered in descending energy order. The distributions shown are the original versions obtained by summing the energies of the constituent particles, not the jet energies calculated using the method of Section 4.5.3.

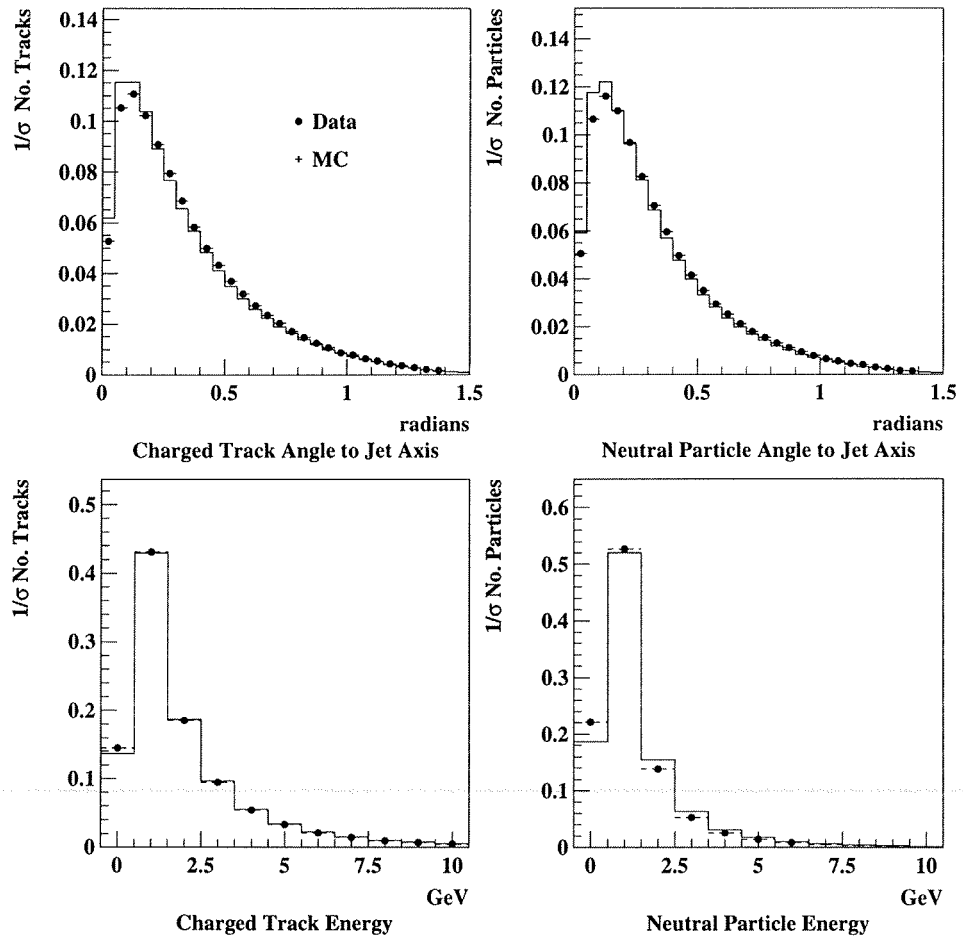

Figure 4.17: Comparison of ALEPH 4-jet Data with $MEMC_4$ predictions of the angle between each track and the jet axis (top plots) and the energy of each track. In both cases the charged and neutral particles have been displayed separately.

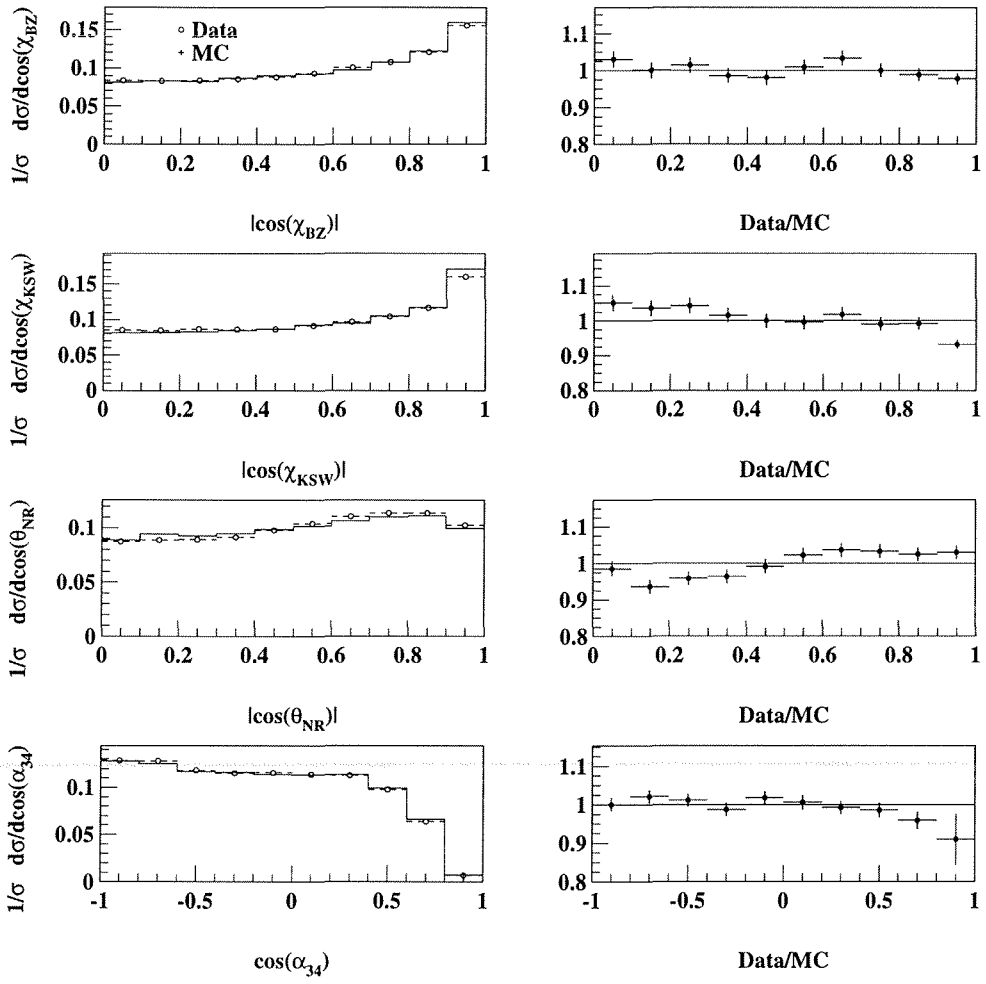

Figure 4.18: Comparison of ALEPH 4-jet Data with MEMC_4 predictions for the Angular Correlation Variables $\chi_{BZ}, \chi_{KSW}, \theta_{NR}$ and α_{34}.

4.5 Analysis Structure

In the next Section we detail the techniques used to obtain from the data a sample of 4-jet events with directions and energies which correspond as closely as possible to those of the parent partons. The analysis contains several steps each of which apply criteria to maximize the number of good events and minimize background contamination. An outline of the main points is provided below.

After applying hadronic event selection cuts the Durham algorithm [46] is used to select 4-jet events. The jet directions are then used to rescale their energies assuming momentum conservation and the same clustering requirement is re-applied. The effect of this step is to improve the energy resolution of the jets and to remove poorly reconstructed events originating from 2 or 3 partons.

The final step in the selection is to apply a two stage tag to pick out the primary quark jets in $b\bar{b}$ events. If two jets are successfully tagged the event is included in the b sample while all others join the udsc sample.

Both data sets selected in this way are then corrected for the effects of hadronization and the detector using response functions derived from Monte-Carlo as explained in Section 4.6. This provides a correction to the 4 parton level available from $\mathcal{O}(\alpha_s^2)$ matrix-element predictions and makes direct comparison of data with theory possible. Chapter 7 explains how theoretical predictions are combined with data to extract values of the Colour Factors.

4.5.1 Hadronic Event Selection

In order to select a clean sample of hadronic decays of the Z^0 boson the following standard cuts are applied to remove background from leptonic decays and two-photon interactions [38].

To be used in the analysis charged particle tracks are required to be reconstructed with at least 4 hits in the TPC and to originate from the beam-crossing point within 5cm along the beam direction and 3cm in the transverse direction. Good tracks must also make an angle of at least 20 degrees with respect to the beam axis and have a transverse momentum greater than 200 MeV. Selected

events have at least 5 such charged tracks and a total charged energy of 15 GeV or more.

Neutral clusters from the energy flow analysis must have an energy of at least 300 MeV and their extrapolation to the interaction point must make an angle of 20 degrees or more with the beam line. The total visible energy of the event is required to be in excess of $0.5\sqrt{s}$ and the momentum imbalance in the beam direction must be smaller than $0.4\sqrt{s}$.

After this selection procedure the data sample contains 3,675,851 events derived from the 139 pb^{-1} of data recorded by the ALEPH detector between 1992 and 1995 at energies close to the mass of the Z^0.

4.5.2 Jet Clustering

The next stage in the analysis is to select 4-jet events from a sample of hadronic events dominated by 2 and 3-jet events. The technique employed is to use the Durham algorithm with the E combining scheme to cluster tracks together to form jets. The process is iterated until the smallest invariant mass between any two clusters exceeds a value known as the y_{cut} which takes the value 0.01 in this analysis. The remaining clusters are then associated with jets. In the data sample we find 192,421 events which contain 4-jets defined in this way. The details of the algorithm and the techniques used to optimize the correspondence between the jets and their parent partons are explained in the next Chapter.

4.5.3 Energy Calculation

If we know the polar and azimuthal angles θ_i & ϕ_i of four jets and assume that they represent massless partons (i.e. $E = |\vec{p_i}|$) then we can calculate the energy of each jet using 4-momentum conservation. This helps us to reconstruct the original parton configuration more accurately by improving the correspondence between the energy of the jet and its parent parton and rejecting poorly reconstructed events. The individual conservation of each 4-momentum component results in the following formulae:

$$\sum_{i=1}^{4} |\vec{p_i}| \mathbf{sin}\theta_i \mathbf{cos}\phi_i = 0 \quad p_x \text{ conservation}$$

$$\sum_{i=1}^{4} |\vec{p_i}| \mathbf{sin}\theta_i \mathbf{sin}\phi_i = 0 \quad p_y \text{ conservation}$$

$$\sum_{i=1}^{4} |\vec{p_i}| \mathbf{cos}\theta_i = 0 \quad p_z \text{ conservation}$$

$$\sum_{i=1}^{4} \mathbf{E_i} = \mathbf{E_{cm}} \quad E \text{ conservation}$$

These simultaneous equations can be represented in matrix form and solved using Cramer's Rule [47] which provides a systematic method for dealing with matrix equations involving algebraic terms.

$$\begin{bmatrix} 1 & 1 & 1 & 1 \\ sin\theta_1 cos\phi_1 & sin\theta_2 cos\phi_2 & sin\theta_3 cos\phi_3 & sin\theta_4 cos\phi_4 \\ sin\theta_1 sin\phi_1 & sin\theta_2 sin\phi_2 & sin\theta_3 sin\phi_3 & sin\theta_4 sin\phi_4 \\ cos\theta_1 & cos\theta_2 & cos\theta_3 & cos\theta_4 \end{bmatrix} \begin{bmatrix} E_1^{calc} \\ E_2^{calc} \\ E_3^{calc} \\ E_4^{calc} \end{bmatrix} = \begin{bmatrix} E_{cm} \\ 0 \\ 0 \\ 0 \end{bmatrix}$$

The 4-momenta of the jets are re-scaled to match the calculated energies and the clustering algorithm is re-applied to remove any events in which the minimum invariant mass is now below the y_{cut}. Events are also excluded from the sample if the re-scaling process produces a negative jet energy or requires a multiplicative factor greater than 3. This leaves 96,785 correctly reconstructed 4-jet events. Figure 4.19 shows the calculated energies and scale factors for jets in the data sample.

To quantify the benefits of removing poorly reconstructed events and calculating the jet energies Figure 4.20 shows the improvement in jet resolution obtained before and after the re-scaling process. The quantities shown are δ_E and δ_θ defined as the difference between the energy and direction of the parton and the energy and direction of the reconstructed jet. We see an improvement in the mean angle between jet and parton of around 23% while the jet energy resolution improves by over 50%. As a result of this the number of events in which the energy

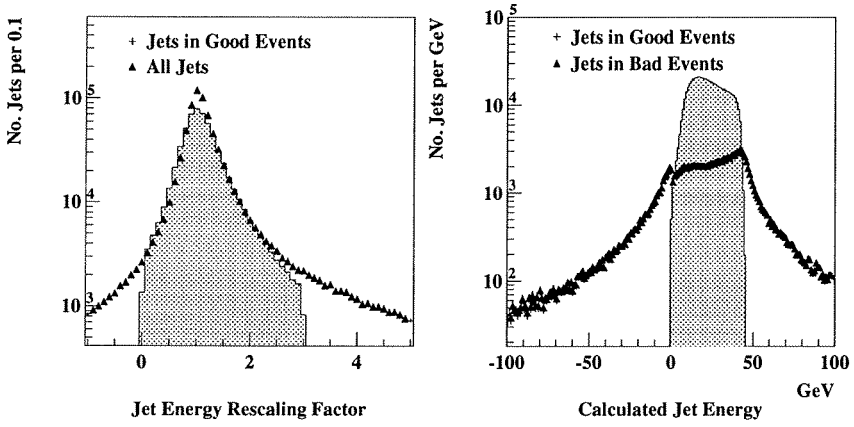

Figure 4.19: In the left hand plot the calculated jet energy re-scaling factors are displayed. The points represent jets from all events in the data sample while the histogram only shows jets from events which pass the cuts. The right hand plot shows the calculated energy for each jet. The points represent jets in events which fail the cuts and the histogram shows jets in events which pass.

ordering of jets correctly reproduces the parton ordering increases from 37% to 55%. This represents a significant step towards an accurate reconstruction of the parton level kinematics, and is an important parameter for the analysis because mis-ordering leads to the 'wrong' ACV value being measured for the event.

In addition to these advances the re-clustering procedure removes all 2 and 3 parton background from the $MEMC_{234}$ sample. The performance is summarized in the following table, which shows figures derived from $MEMC_{234}$ events but which also apply to the $MEMC_4$ data.

Parameter	Value before E_{calc}	Value after E_{calc}	Change
$< \delta_\theta >$	6.56°	5.05°	- 23%
$< \delta_E >$	4.93 GeV	2.28 GeV	- 54%
2,3 parton events	1.6%	$< 0.02\%$	- 1.6%
Correctly ordered	37%	55%	+ 18%
# Events in sample	8301	4440	- 53%

4.5.4 Heavy Quark Tagging

The ACV's used in this analysis rely on being able to differentiate between the primary $q\bar{q}$ and secondary partons. Historically, the technique of energy ordering has been used to do this which exploits the tendency of the primary quarks to be harder than the other partons. This method fails in nearly half of all events, however [40].

In order to maximize the accuracy of the measurement, this analysis selects jets arising from primary $b\bar{b}$ quarks via their long lifetime signature. The 4-jet sample selected up to this point is exposed to the tagging procedure detailed in Chapter 6. Events in which two jets pass the selection cuts are included as part of the b sample while the others go to form the udsc sample.

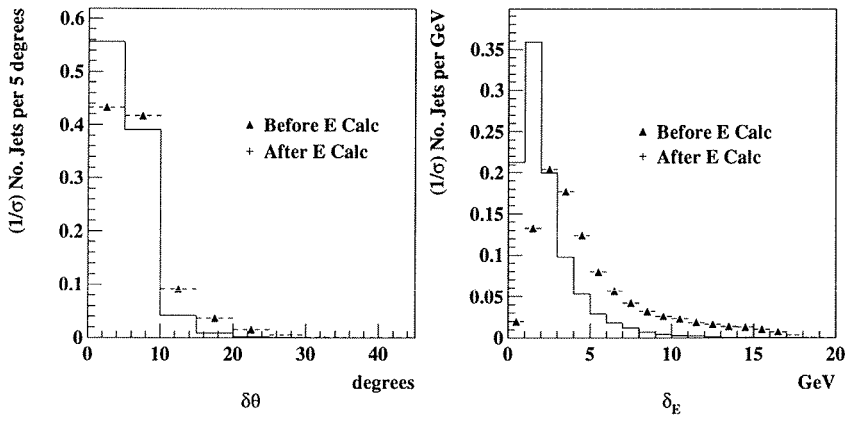

Figure 4.20: The plot on the left shows the difference between the direction of the reconstructed jet and the original parton before and after the re-scaling process. The right hand plot shows the difference in energy for each case.

The b sample is corrected using a dedicated MEMC sample enriched in heavy flavour events as explained in Section 6.4. It is then combined with a matrix-element calculation which includes quark masses to produce a measurement of the Colour Factors.

The details of the MC correction for the udsc sample are given in the next Section. Chapter 7 explains the final step in which the corrected data is combined with a massless matrix element prediction to provide a second independent Colour Factor result.

4.5.5 Analysis Summary

The following table summarizes the number of events selected at each stage of the analysis process explained above for both the $MEMC_4$ and data samples.

Analysis Stage	# Events in Data	% of data	# Events in $MEMC_4$	% of $MEMC_4$
Hadronic Selection	3,675,851	100 %	433,792	100 %
4-Jet Selection	192,421	5.2 %	74,051	17.1 %
E_{calc} & Recluster	96,785	2.6 %	40,403	9.3 %
udsc sample	90,627	2.4 %	36,833	8.5 %
b sample	6,158	0.2 %	3,570	0.8 %

4.6 Correction Procedure

The $MEMC_4$ Monte-Carlo sample introduced above is used to correct the udsc sample for detector and hadronization effects. The method used to correct the b sample is explained in Chapter 6 but follows similar lines.

The ACV's are plotted at 3 stages in the Monte-carlo: at the parton level described by the matrix-element (PARTON), after hadronization but before the detector simulation (HADRON), and after the detector simulation and event reconstruction (RECO). The changes observed in the distributions between each stage are a measure of the systematic shifts caused by the hadronization process and imperfections of the detector. Compensation for these systematic shifts can be achieved by applying a multiplicative correction factor to the data derived from the ratio of the MC distributions before and after the hadronization and detector simulation processes.

In the following all plots are derived from the $MEMC_4$ sample and the different stages of analysis are defined as follows. The RECO plots have been produced from MC data which has been hadronized and then passed through the ALEPH detector simulation and exactly the same analysis chain as the data. The HADRON plots are derived from the same events as those passing the RECO level selection which also cluster to give 4-jets at hadron level. The PARTON level plots consist of all events in which the minimum invariant mass between any pair of partons is above the y_{cut} used in the rest of the analysis, irrespective of whether they pass

the other selections.

Figure 4.21 compares some jet quantities which highlight the general effects of the detector and hadronization process. In Figure 4.22 we see the correction function for each ACV split into hadronization and detector corrections. The hadronization correction is defined as $\text{ACV}_{parton}/\text{ACV}_{hadron}$ and the detector correction is defined as $\text{ACV}_{hadron}/\text{ACV}_{reco}$. At the foot of the plot is the full correction from RECO to PARTON level as used in the final analysis. It is defined as $\text{ACV}_{parton}/\text{ACV}_{reco}$.

We can see from the figures that the full correction is mostly flat and the detector correction is regular. The hadronization correction, however, is sensitive to the region where the ACV tends to 1, an effect which is also visible in the last bin of the full correction. For each of the variables this region of phase space corresponds to having two jets close in angle. The large values of the correction function in this area attempt to compensate for events which fail the y_{cut} after the jet broadening of the hadronization process, and are subsequently removed from the sample.

The slight dip visible in the detector correction for the α_{34} variable can be understood as follows. At the HADRON level energy mis-ordering is reduced to one third of its level at the RECO stage. Figure 4.23 shows the correction function for the energy ordering process, defined at RECO level as the ratio of ACV's from correctly ordered events to energy ordered events. This shows much the same features as the detector correction suggesting that the dominant detector effect is due to mis-ordering. Note that we define 'correctly ordered events' by associating each jet to the closest parton in angle and adopting the parton level energy ordering.

In Figure 4.24 we see the effect of the full correction function on the data. The final ACV distributions are shown before and after the correction has been applied, as well as the correction functions employed. The regularity of these functions gives us confidence that the ACV's are insensitive to the hadronization process and detector imperfections, and hence that the corrected distributions provide a reasonable description of parton processes.

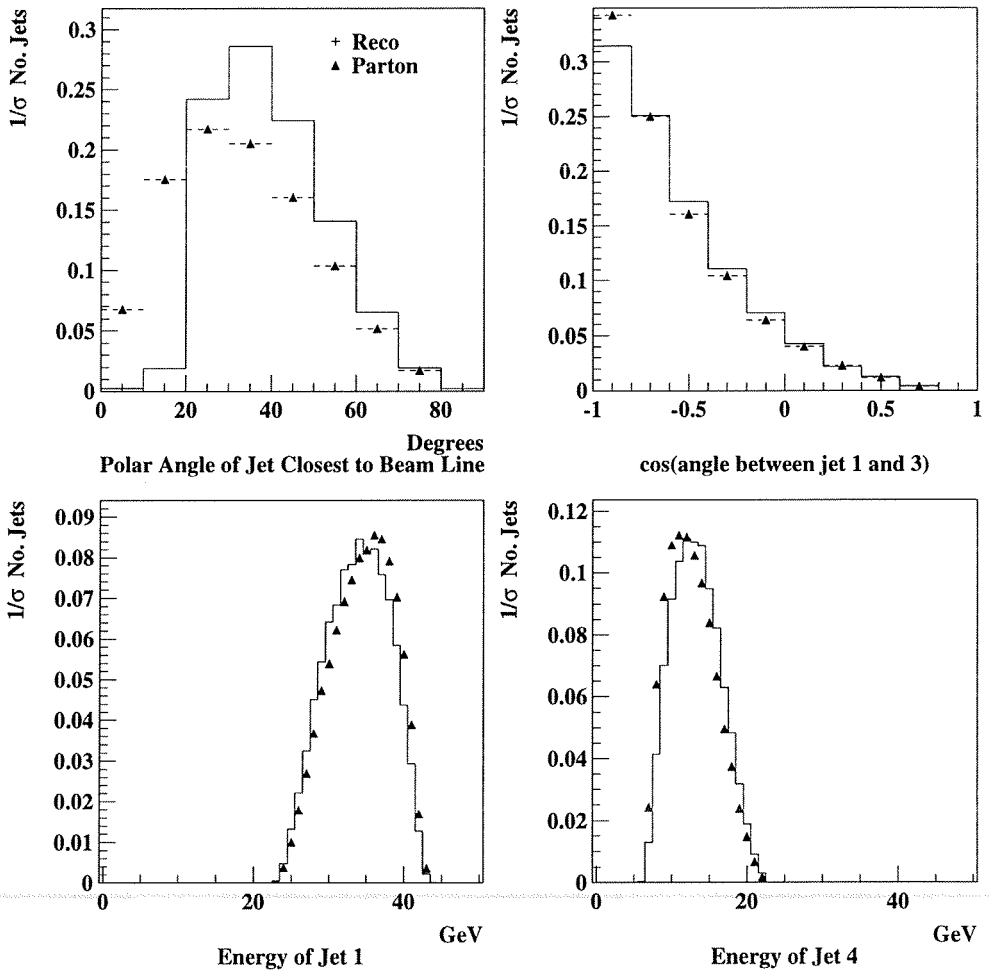

Figure 4.21: Comparison of $MEMC_4$ jet quantities at the parton and reconstructed level. The top left plot displays the angle between the beam line and the nearest jet highlighting the losses due to non-hermeticity of the detector. The top right plot shows the angle between jets 1 and 3 and demonstrates that inter-jet angles are less sensitive to these effects. The jet energy distributions shown at the bottom are similarly insensitive.

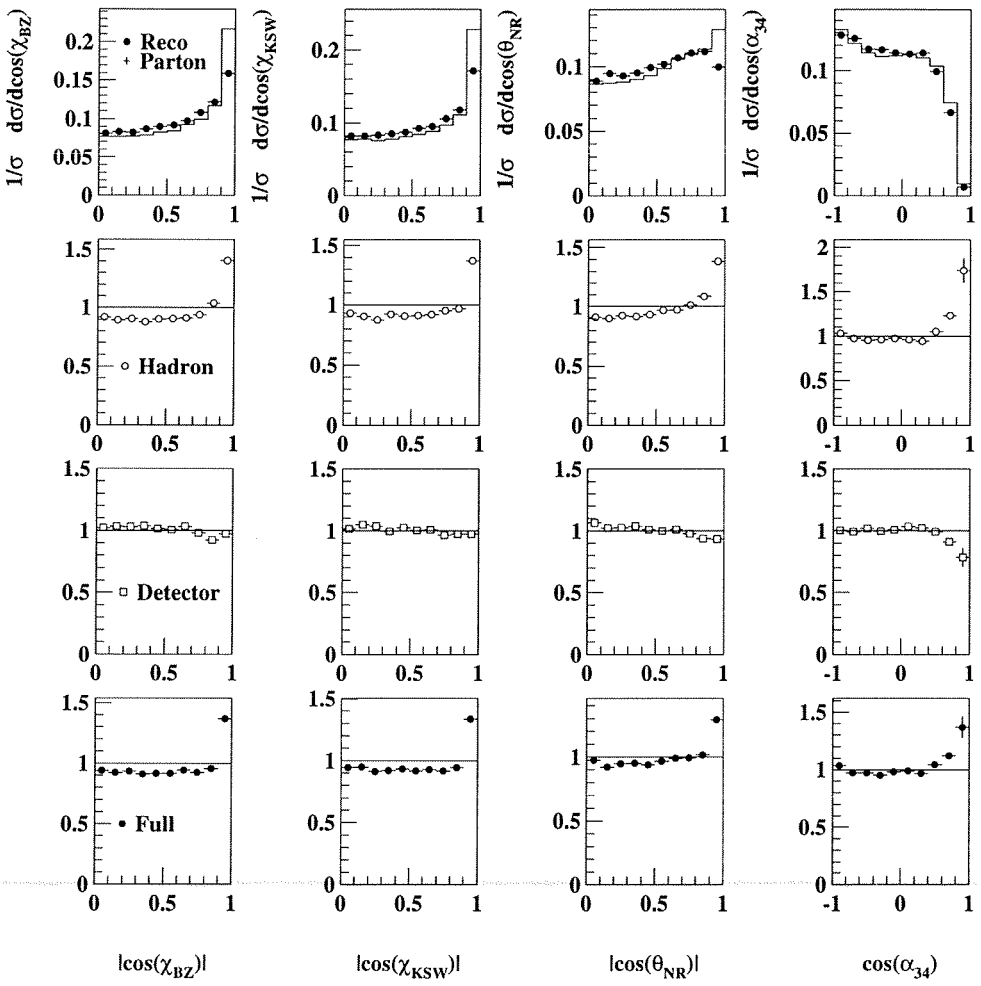

Figure 4.22: At the top of the figure we see the RECO and PARTON level ACV's with the full correction function derived from the ratio of these shown at the bottom. All correction functions have been normalized as the overall efficiency is not a factor in this analysis. The middle plots show the correction functions derived from the MEMC_4 sample for each ACV divided into hadronization and detector components.

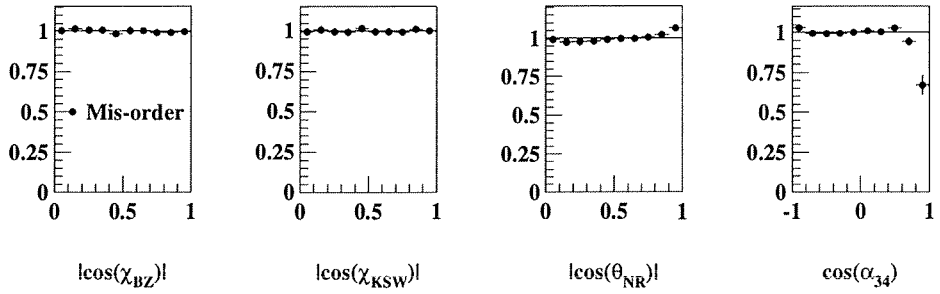

Figure 4.23: Correction functions for the problem of energy ordering failing to assign the jets to their parent partons correctly. The plots shown have been derived at the RECO level as the ratio of (correctly ordered events)/(energy ordered events).

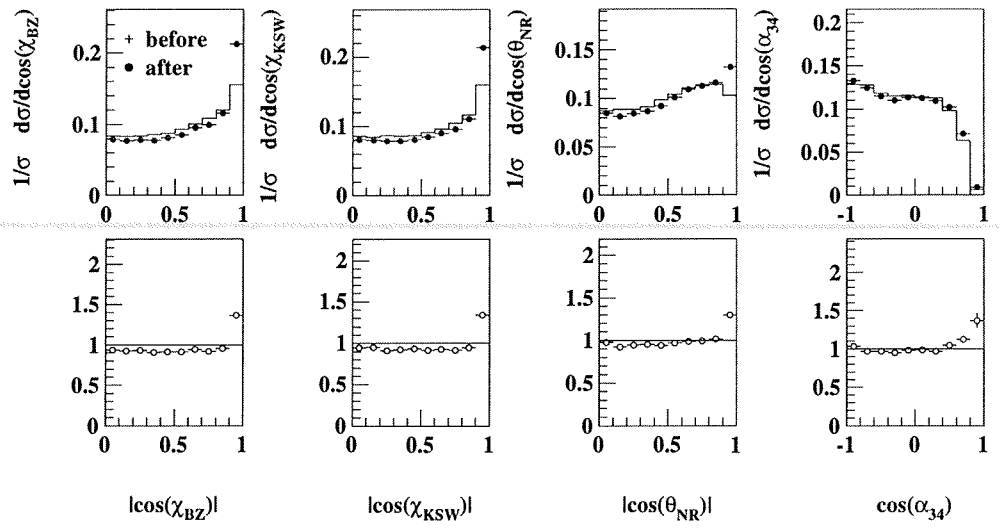

Figure 4.24: The udsc data sample before and after the full correction function from RECO to PARTON level has been applied. The error bars shown combine the statistical uncertainties of the $MEMC_4$ and data samples. The lower plots show the multiplicative correction function.

Chapter 5

Jet Clustering

This Chapter discusses how to obtain parton level information from hadron jets. It covers the selection of a jet clustering algorithm and the Monte Carlo studies used to compare a range of alternative strategies. The final Sections quantify the performance of the chosen algorithm.

5.1 Associating Partons with Jets

A key element in the analysis presented here is the ability to reconstruct the direction and energy of partons from the hadron jets they produce. This one-to-one association is necessary because theoretical predictions are expressed in terms of partons rather than the collimated streams of hadrons we observe in the detector. The process of obtaining this information experimentally has two steps: measuring jet distributions in data, and correcting them for hadronization and detector effects to produce parton level information.

The technique used here to reconstruct jets is the clustering algorithm, which can be thought of as an attempt to run the successive branchings of the parton shower in reverse. There are several variants which share the common structure of finding some distance y_{ij} between all tracks in an event and combining the pair with the lowest value into a composite cluster. The procedure is iterated until the smallest distance left in the event exceeds a prescribed value, at which point the remaining clusters are considered to be jets. The possible variations include

different clustering techniques which decide whether a pair of clusters should be merged, and different combining schemes which decide how to join them.

5.2 Jet Clustering Algorithms

This analysis employs the DURHAM metric for calculating the distance between tracks i & j with a minimum value of $y_{ij} > y_{cut} = 0.01$. When joining two tracks to form one composite cluster the 'E' scheme is employed to calculate the new 4-momentum as detailed below.

This choice is justified in the following Section where the MEMC_{234} sample is used to compare how well various schemes pick out 4-jet events which come from 4 partons at the expense of 4-jet events from 2 or 3 partons. The sensitivity of the algorithm to hadronization and detector effects provides a second measure of performance through the accuracy with which the parton energy and direction are reproduced.

The y_{ij} distance measure is defined below for the DURHAM scheme as well as for an alternative known as the JADE algorithm which calculates the scaled invariant mass between tracks [48].

$$\text{DURHAM} \quad y_{ij} = \frac{2min(E_i^2, E_j^2)(1-cos\theta_{ij})}{E_{vis}^2}$$

$$\text{JADE} \quad y_{ij} = \frac{2E_iE_j(1-cos\theta_{ij})}{E_{vis}^2}$$

In the above expressions E_i is the energy of particle i, θ_{ij} is the angle between particle i and j, and E_{vis} refers to the total energy of all particles in the event. A third technique, known as the PTCLUS scheme mixes two distance measures [49]. In an initial stage the hardest particle in the event is used as a jet initiator to which particles are assigned if their P_T^2 is below 0.15 $(\mathrm{GeV/c})^2$. The hardest particle which fails the P_T cut then initiates a new jet and the process is repeated. Once all particles have been assigned in this way the clusters are merged with the JADE scheme and then in a final step all particles are re-assigned to the nearest jet in P_T. The following comparisons use a variant of the standard PTCLUS method

which uses the DURHAM scheme in the clustering step. Note that the P_T cutoff is fixed and that the main variability in the scheme comes from the choice of y_{cut} used.

The 'E' combining scheme performs a straightforward summing of the components of the 4-vector, but there are other options for this process. The 'E0' and 'P' schemes calculate the new cluster 4-vector so as to form massless jets. The combining process has less influence on the jet structure and subsequently the choice of combination scheme is less critical than the clustering method.

Combining Scheme	Algorithm
E SCHEME	$\vec{p}_{new} = \vec{p}_i + \vec{p}_j$ $E_{new} = E_i + E_j$
P SCHEME	$\vec{p}_{new} = \vec{p}_i + \vec{p}_j$ $E_{new} = \lvert\vec{p}_{new}\rvert$
E0 SCHEME	$\vec{p}_{new} = \frac{E_{new}}{\lvert\vec{p}_i+\vec{p}_j\rvert}(\vec{p}_i + \vec{p}_j)$ $E_{new} = E_i + E_j$

Note that the different definitions of y_{ij} lead to the numerical y values of the schemes being incompatible. This fact is highlighted in Figure 5.1 which shows the different 4-jet rates measured in the data with the three schemes as a function of their respective y_{cut} values.

5.3 Optimizing the Algorithm

Having introduced the clustering schemes we now proceed with the evaluation process. One of the main problems involves 2 and 3 parton events which are reconstructed at detector level as containing 4-jets. The initial comparison criteria will be the efficiency with which the algorithm selects 4-jet events originating from 4 partons, and the purity of the 4-jet sample with respect to 2 and 3 parton

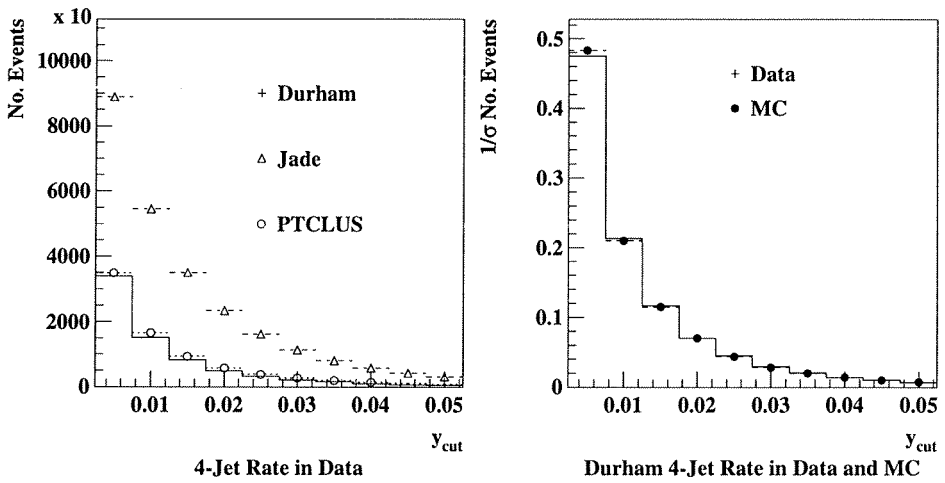

Figure 5.1: The left hand plot shows the 4-jet rate observed in data as a function of y_{cut} for the DURHAM, JADE and PTCLUS clustering algorithms. All of the distributions are derived using the 'E' combining scheme and are made at the RECO level. The right hand plot compares the DURHAM 4-jet rate in data and the MEMC_{234} sample.

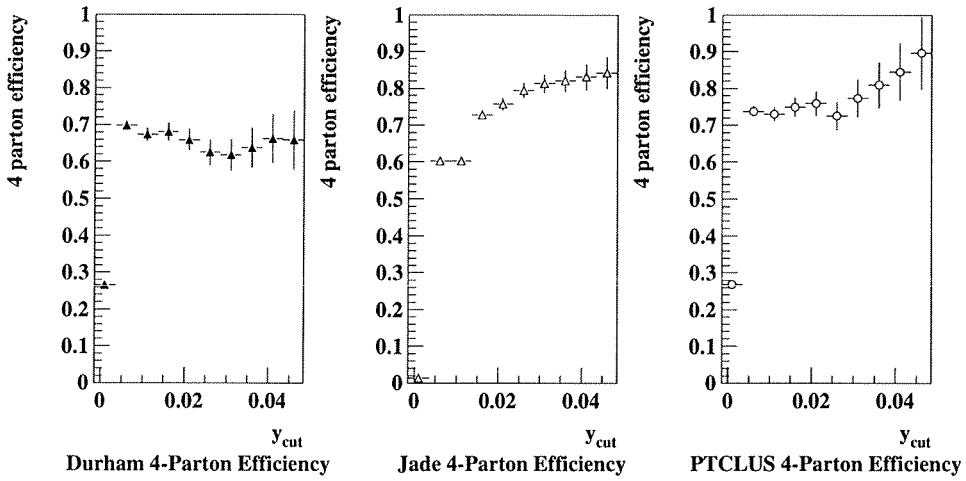

Figure 5.2: The 4 parton selection efficiency for each algorithm, defined as the number of 4 parton 4-jet events divided by the total number of 4 parton events at this y_{cut}.

contamination. It should be noted that the information derived from this comparison is also used to select the best value of the y_{cut} parameter for the chosen scheme. All plots in the remainder of the Section are derived from the MEMC_{234} sample and show the effect of the jet finding before the energy calculation and re-clustering scheme.

Figure 5.2 shows the 4 parton selection efficiency defined as the number of 4 parton 4-jet events found at a given y_{cut} divided by the total number of 4 parton events at this y_{cut}.

In Figure 5.3 we compare the signal to background ratios for each clustering scheme defined as the ratio of 4-parton 4-jet events (signal) to 2 and 3 parton 4-jet events (background). Note that these plots display the information more accessibly than the conventional purity measure because in this case the purity tends to unity for all algorithms.

Combining the information presented in the previous three Figures we can

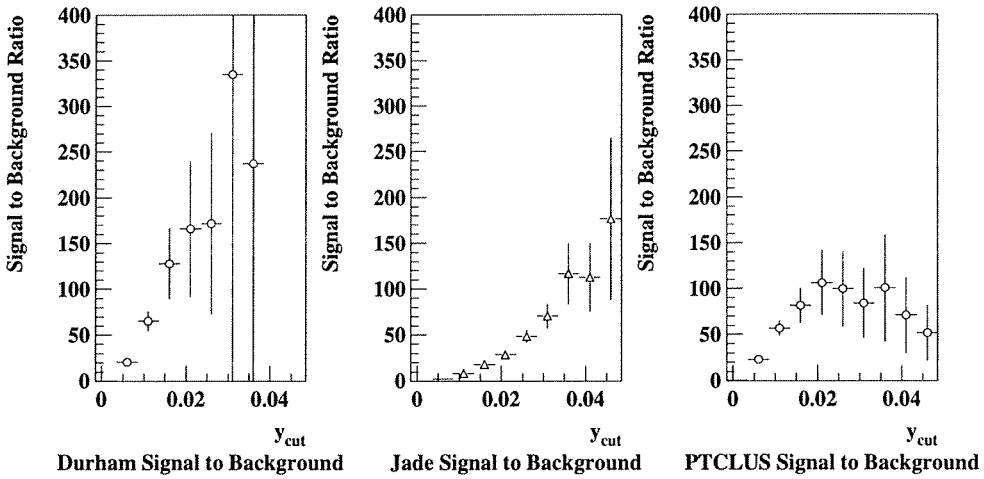

Figure 5.3: The 4-jet signal to background ratio for each clustering scheme as a function of y_{cut}. The plots show the ratio of 4-parton 4-jet events (signal) to 2 and 3 parton 4-jet events (background).

choose the best y_{cut} for each algorithm and thus make a comparison of each scheme. A balance must be struck between statistics which favours low y_{cut} values and the purity of the sample from 2 and 3 parton contamination which favours high values.

Looking initially at the DURHAM algorithm we see that the lowest y_{cut} value which reaches an acceptable level of purity is 0.01, which combines a signal to background ratio of 65 with good statistics. To compare this performance with JADE in a fair way we must look at a y_{cut} value around 0.027 in order to have the same number of 4-jet events. To compare PTCLUS we use the same y_{cut} value of 0.01 as it is based on the DURHAM algorithm. At these points JADE has a signal to background ratio of 55 while PTCLUS has a ratio of 54.

In addition to the 2 and 3 parton background we also compare the performance of the algorithms in terms of how well the characteristics of the parton initiator of the jet are reproduced. The relevant parameters are the difference in angle between the jet and parton (δ_θ) and the difference in energy (δ_E) as introduced in the previous Chapter.

In Figure 5.4 we compare the clustering algorithms in terms of δ_θ and δ_E. The following table summarizes the performance of each through the mean value of the distribution, and the quoted errors are statistical only. In the DURHAM and PTCLUS plots a y_{cut} value of 0.01 is used, and in the JADE plots the equivalent value of 0.027 is used.

Clustering Algorithm	$< \delta_\theta >$ (degrees)	$< \delta_E >$(GeV)
DURHAM	6.31 ± 0.05	4.69 ± 0.04
JADE	7.67 ± 0.05	4.81 ± 0.04
PTCLUS	6.11 ± 0.05	4.61 ± 0.03

These figures show a definite improvement in the angular resolution of the DURHAM algorithm, which when combined with the increased background rejection detailed above confirms our choice of DURHAM with a y_{cut} of 0.01 as the best clustering algorithm in this environment.

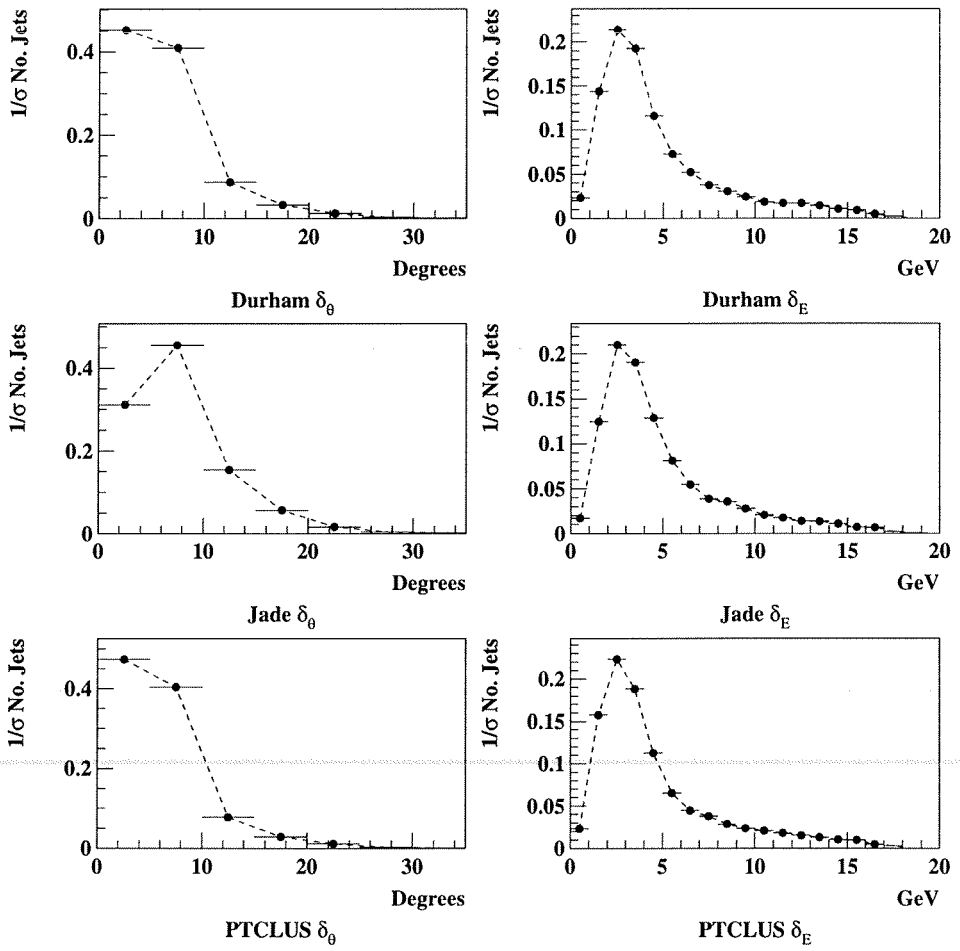

Figure 5.4: Comparison of angular and energy resolutions achieved with the DURHAM, JADE and PTCLUS clustering techniques.

Now we turn to the choice of combining algorithm. In Figure 5.5 we apply the same parton reconstruction quality test to the E P and E0 schemes. The plots are made using the DURHAM algorithm with a y_{cut} of 0.01. The mean of each distribution is displayed in the following table.

Combining Algorithm	$< \delta_\theta >$ (degrees)	$< \delta_E >$(GeV)
E	6.31 ± 0.05	4.69 ± 0.04
P	6.04 ± 0.05	4.83 ± 0.04
E0	6.44 ± 0.05	4.73 ± 0.04

From the above we can see that the choice of combining algorithm does not influence the quality of jet reconstruction significantly. Note that in making this choice we must consider the issue of jet masses in light of the fact that the energy calculation procedure assumes all jets to be massless. Also the b sample would naturally contain jets of larger mass than the udsc sample. However when we compare massive and massless jets constructed with the E and E0 schemes both in terms of the total efficiency of the energy calculation procedure and of the efficiency for b events, no difference is found between the two approaches. Having failed to differentiate between the performance of the three methods, the E scheme was chosen for its simplicity.

In addition to the choice of jet finder an attempt was made to improve the accuracy of jet reconstruction by applying a range of further cuts after the energy calculation scheme. These included a restriction on the angle of the event Thrust-axis[1] so as to be well contained in the detector, a cut on how close a jet could be to the beam line, a minimum jet energy and a minimum jet multiplicity. However, these measures proved not to be effective in improving the reconstruction quality. As a result the reduction in statistics could not be justified and the cuts were

[1]The Thrust-axis is calculated for an event by picking the direction for which the sum of the projections of all particle momenta is maximized. The value of the Thrust variable is given by the sum of the projections along this axis divided by the sum of all particle momenta.

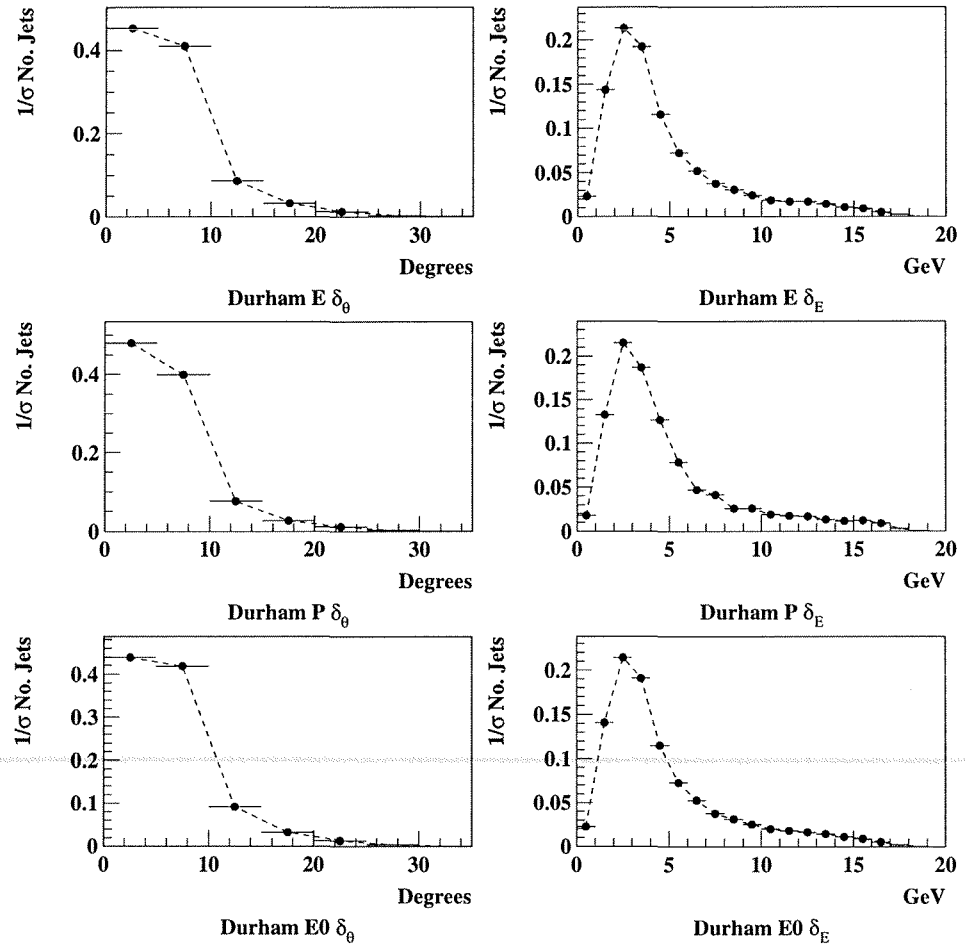

Figure 5.5: Comparison of angular and energy resolutions achieved with the E, P and E0 combining techniques.

abandoned in favour of a more elegant analysis structure including only clustering and jet energy calculation.

5.4 Reconstruction Performance

This Section investigates the performance of the chosen DURHAM jet finding algorithm in reproducing the parton level kinematics of the event. It contains systematic checks to ensure that hadronization and detector effects do not introduce a bias in any region of jet angle or energy. Each Section quotes the resolution attained on parton characteristics and the ACV accuracy which these imply are calculated at the end of the Chapter. Note that all plots display the combined effect of the clustering algorithm and the energy calculation scheme introduced in Section 4.5.3.

5.4.1 Angular Resolution

The variation of the angular resolution of the jet as a function of its position in the detector is investigated in Figure 5.6 which shows δ_θ as a function of the jet angle to the beam line. Recall that the angular resolution δ_θ is defined as the difference in angle between the jet and its parton initiator. One would expect jets close to the beam line to be poorly reconstructed and suffer from degraded angular resolution, but the smoothness of the plot above the acceptance cutoff confirms that this effect is not important. This regular response is an artefact of the the energy calculation scheme which tends to remove poorly reconstructed events.

The reconstruction quality of jets as a function of their energy is examined in Figure 5.7 which shows that low energy jets tend to suffer from poor angular resolution. The detector seems to have little influence on this phenomenon as can be seen from the similarity of the RECO and HADRON level plots. The effect is due to the tendency for low energy jets to arise from secondary parton production, which is mainly due to gluon rather than quark initiators. The hadronization of gluon jets has been shown to be considerably less collimated than quark jets of

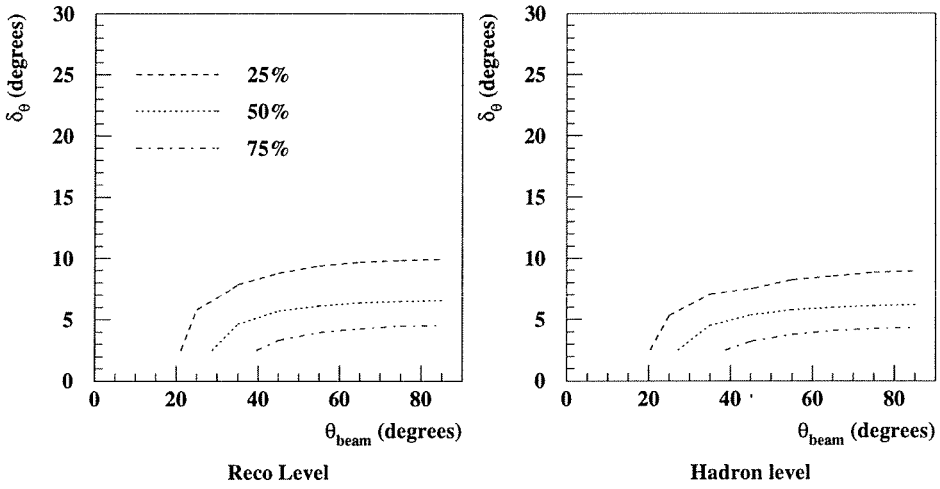

Figure 5.6: Contour plot of the jet angular resolution (δ_θ) as a function of the angle of the jet to the beam line. The lines show the height of the plot at that point. The left hand plot includes both hadronization and detector effects (RECO level) while the right hand plot includes only hadronization effects (HADRON level).

similar energy [50] leading to diffuse jets with less well defined directions and a greater probability of particles being included in the wrong jet.

When we integrate over the energy and angular dependence of the above distributions we obtain the result that the average resolution on the parton direction is $< \delta_\theta >= 5.05° \pm 0.01°$ (statistical error only). This spread is mainly due to the hadronization process (4.7°).

5.4.2 Energy Resolution

The quality of the jet energy reconstruction is investigated in Figure 5.8 which shows δ_E as a function of the jet angle to the beam line.. Recall that the energy resolution δ_E is defined as the difference between the energy of the jet and its parton initiator. The smooth variation above the cutoff introduced by the accep-

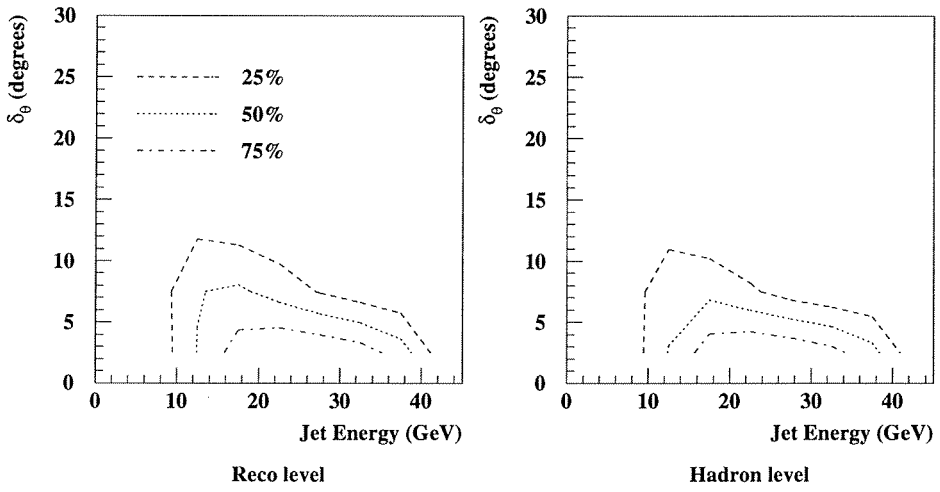

Figure 5.7: Contour plot of the jet angular resolution (δ_θ) as a function of the jet energy. The lines show the height of the plot at that point. The left hand plot includes both hadronization and detector effects (RECO level) while the right hand plot includes only hadronization effects (HADRON level).

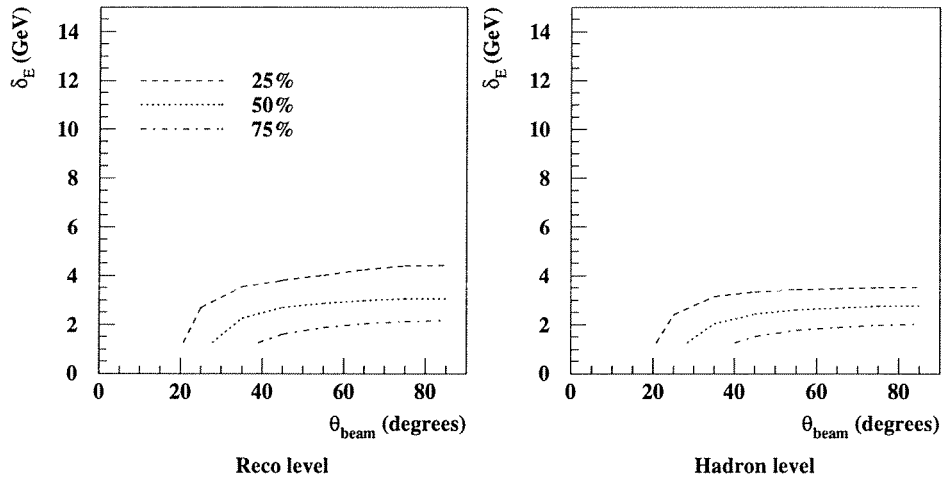

Figure 5.8: Contour plot of the resolution on the jet energy (δ_E) as a function of the angle of the jet to the beam line. The lines show the height of the plot at that point. The left hand plot includes both hadronization and detector effects (RECO level) while the right hand plot includes only hadronization effects (HADRON level).

tance limit again confirms that the analysis is insensitive to poorly reconstructed jets in this region.

Figure 5.9 shows that the energy resolution of low energy jets is degraded in the same way as the angular resolution. This is an artefact of the increased width of gluon jets which dominate the low energy region. This width leads to an increase in particle to jet mis-assignment which results in poor jet energy resolution.

When the energy and angular dependence of the above distributions are integrated out the average resolution on the parton energy is found to be $< \delta_E > = 2.28 \pm 0.01$ GeV (statistical error only). This comes primarily from the hadronization process (1.52 GeV).

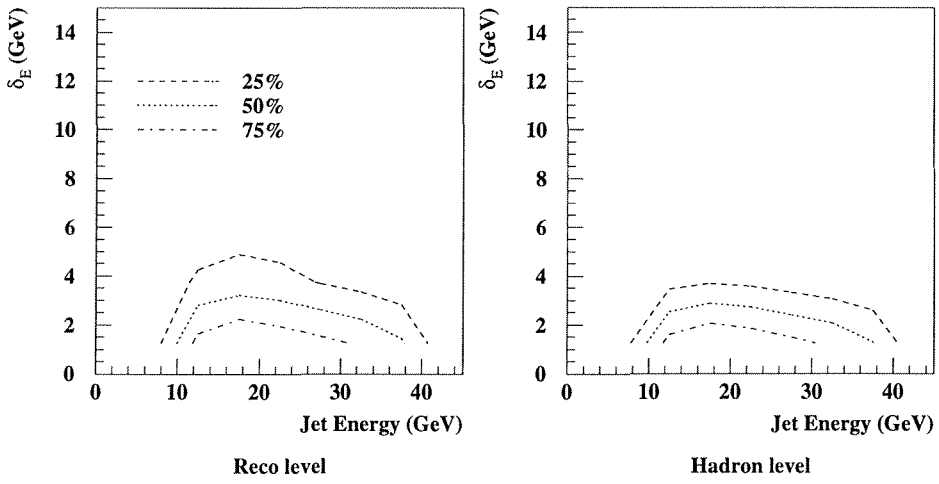

Figure 5.9: Contour plot of the resolution on the jet energy (δ_E) as a function of the jet energy. The lines show the height of the plot at that point. The left hand plot includes both hadronization and detector effects (RECO level) while the right hand plot includes only hadronization effects (HADRON level).

5.4.3 ACV Resolution

In this Section we conclude the discussion of jet techniques by extracting the accuracy with which we can measure each ACV from the angular and energy resolutions quoted above. The results obtained are given in the following table.

ACV	% error	δ_{acv}	Av. Bin Width
χ_{BZ}	5.7%	5.1°	9°
χ_{KSW}	5.7%	5.1°	9°
θ_{NR}	11.5%	10.4°	9°
α_{34}	4.0%	7.2°	18°

The fact that the resolutions obtained for the ACV's are less than or comparable to the bin width used to plot the variables is significant. It encourages the belief that transitions between bins as a result of the hadronization process and detector effects will be small. This fact justifies the use of a multiplicative correction function rather than a matrix which would track any inter-bin movement.

In conclusion we have justified the choice of clustering technique and shown the analysis procedure to be free from any large systematic biases in a region of jet energy or area of the detector. The few percent resolution achieved on the characteristics of the original parton give us confidence that the procedure used is particularly insensitive to hadronization effects, and that any shortcomings of the detector have negligible impact.

Chapter 6

Heavy Quark Tagging

This Chapter introduces the techniques used to identify b quark jets in 4-jet events. The motivation for this method and the way in which it complements the rest of the analysis have been discussed in Chapter 4. The tagging procedure is explained in the next Section which is followed by a comparison of the appearance in data and Monte-Carlo of variables relevant to the analysis. The Chapter concludes with a statement of the correction method applied to the data.

6.1 Lifetime Tagging

Lifetime tagging is used to overcome the problem of failing to pick out primary quark jets with the energy-ordering technique and thus mis-measuring variables. It exploits the relatively long 1.5 picosecond lifetime of b hadrons [51] which results in flight lengths of around 2mm before decay. The displaced decay vertices are measurable with the vertex tracking detector introduced in Chapter 2 which, when combined with the other tracking detectors, achieves an impact-parameter resolution of 25μm for a well-defined track.

Two lifetime tags are in use within the ALEPH Collaboration. One employs the impact-parameter information of each charged track directly, while the other searches for groupings of tracks which do not originate from the main interaction point, known as secondary decay vertices. The remainder of this Section introduces the principles upon which the two methods rely.

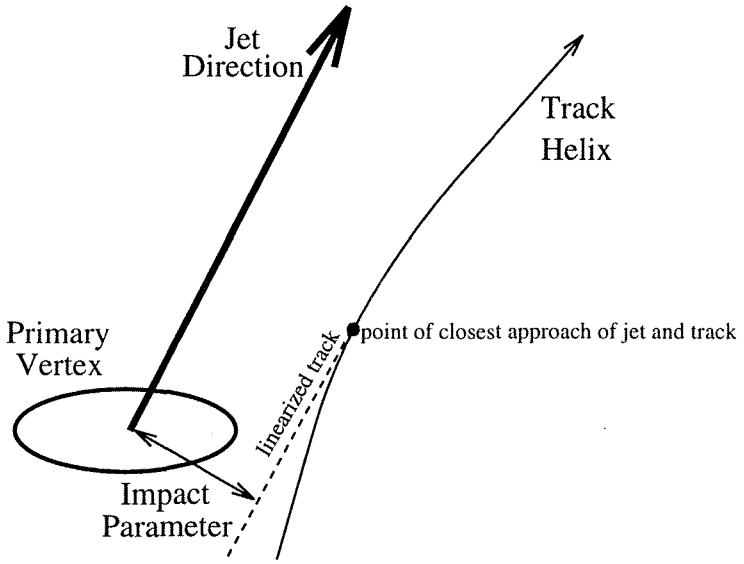

Figure 6.1: The definition of the impact-parameter used in identifying tracks from displaced decay vertices. The linearized track extrapolates the direction of the track at its point of closest approach to the jet toward the primary vertex. The distance of closest approach of this extrapolation to the primary vertex defines the impact-parameter.

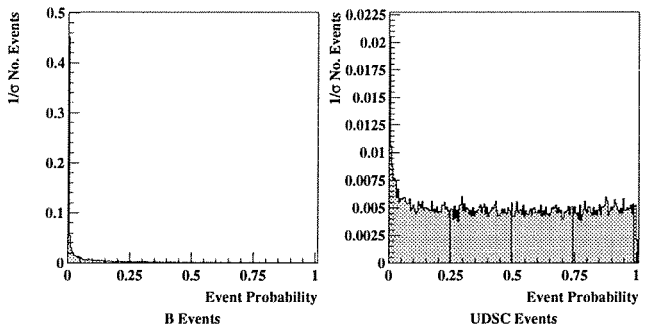

Figure 6.2: The distribution of the probability that an event contains no lifetime for b events (left hand plot) and udsc events (right hand plot). Each distribution has been normalized to unit area.

The impact-parameter is defined as the distance of closest approach between a track and the primary interaction point as shown in Figure 6.1. The impact-parameter is signed +ve (-ve) depending on whether the point of closest approach of the track and jet are in the same (opposite) hemisphere as the jet.

In order to have an even handed treatment of well and poorly measured tracks the QIPBTAG routine [53] deals with the 'significance' of tracks, defined as their signed impact-parameter divided by the error on this quantity. In the absence of lifetime the tracks would be evenly distributed around the interaction point, and indeed this is what we observe for uds events which have a symmetric distribution of positive and negative significance values. Assuming that any enhancements of positive significance compared to the negative distribution are due to lifetime effects we can derive a probability that a track originated from the primary vertex. This probability has been combined for all tracks in the event to produce a probability that the event contains no lifetime.

In Figure 6.2 we see the probability that an event contains no lifetime for 4-jet b and udsc events in the MEMC_{234} sample. The enhancement at zero for b events is clearly visible, while the udsc plot is mainly flat.

The QVSRCH routine [54] looks in a jet for secondary vertices. It scans the

coordinate space near the interaction point calculating the change in the track fit χ^2 obtained by assigning tracks to either the primary, or the primary plus a candidate secondary vertex at each point. The position which produces the greatest reduction in the χ^2 is chosen as the origin of the new vertex and tracks are then assigned depending on whether they have a lower impact-parameter relative to the primary or the new secondary vertex. This method is based on the same impact-parameter information as the QIPBTAG routine but employs it in a way which exploits the distinctive grouping of b tracks in displaced vertices.

6.2 The Combined Tag

In order to maximize the purity and efficiency with which b jets are selected a tag was developed which combines lifetime and jet energy information in a novel way. The energy of each jet is incorporated in the tag because of the tendency for primary b quarks to be harder than secondary partons as shown in Figure 6.3. A high P_T lepton tag was not used as the 20% semi-leptonic branching ratio of b decays [52] would limit the double tag efficiency to 4%.

The tag proceeds in two steps. An initial exclusion of udsc events is made by cutting on the probability that an event contains no lifetime derived from the QIPBTAG routine. Events which do show significant lifetime are processed by the QVSRCH routine which finds a secondary vertex in each jet and returns a significance for the new vertex calculated as the distance from the primary vertex divided by the error on this quantity. The vertex significance is plotted as a function of jet energy to form a two-dimensional variable on which a cut is made. The analysis requires two jets to pass this cut in order for the event to be included in the b sample. All remaining events form the udsc sample.

Figure 6.4 shows the two-dimensional variable for b and udsc events. The ratio of the two plots is shown in Figure 6.5 in which the signal to background values peak at high jet energy and vertex significance. A cut line is drawn in this plane above which jets are considered to come from b quark initiators.

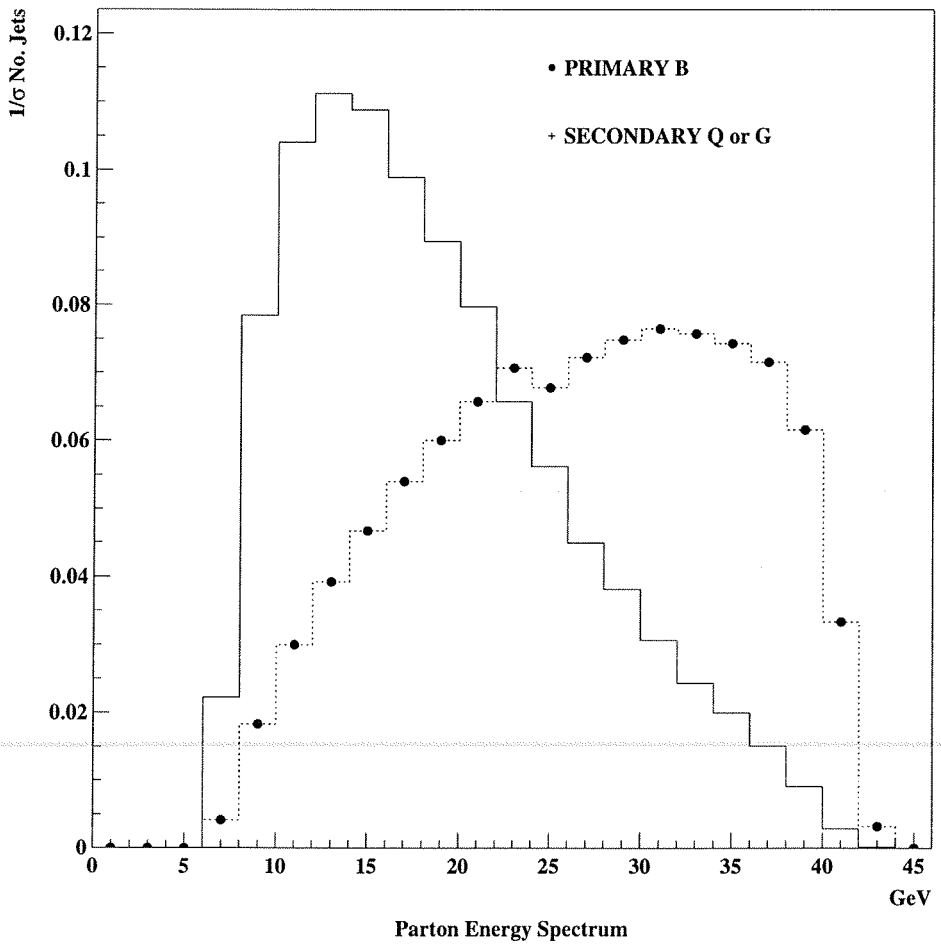

Figure 6.3: The energy distribution of primary b jets and secondary quark and gluon jets at parton level. Both plots have been normalized to unit area.

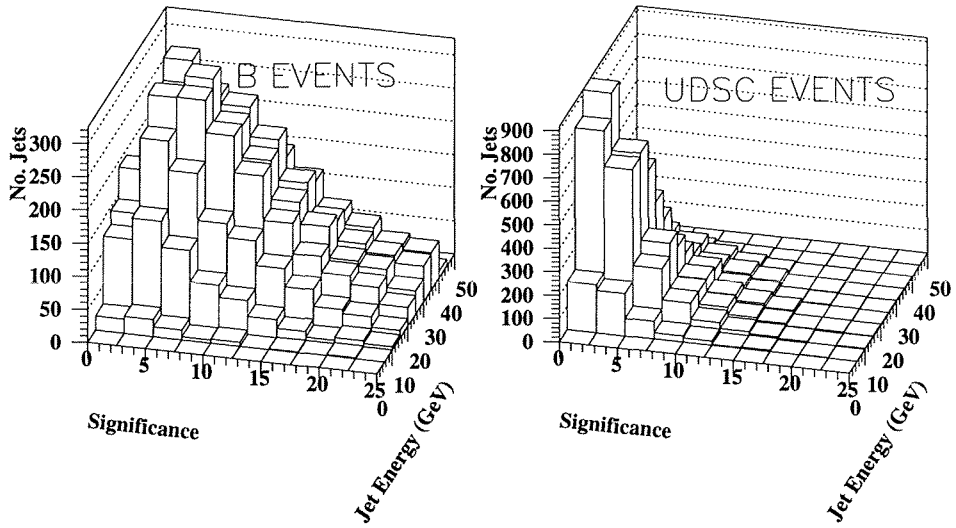

Figure 6.4: The two-dimensional plot of jet energy as a function of vertex significance for b and udsc events.

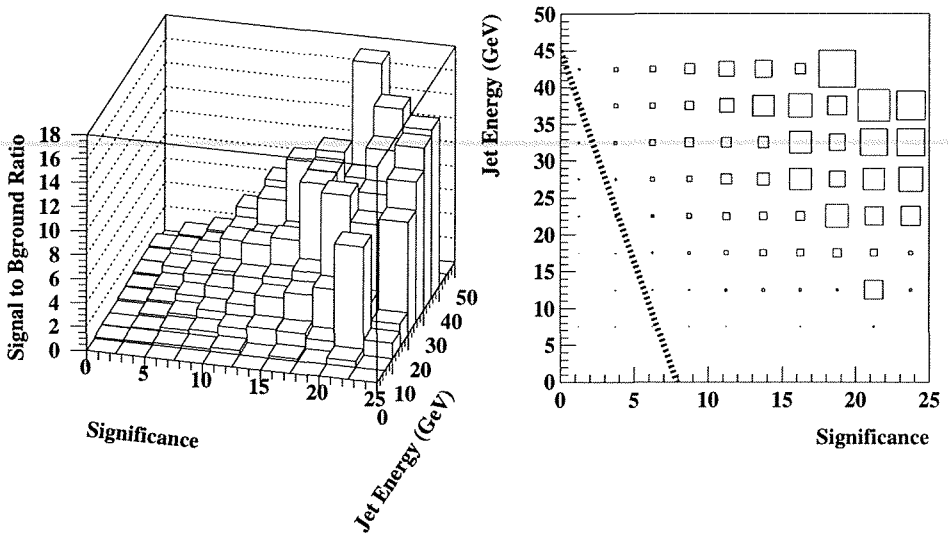

Figure 6.5: The ratio of b and udsc events in the jet energy / significance plane. The line in the right hand version of the plot represents the cut used in the final analysis.

6.3 Tag Optimization

Having introduced the two-step tag we proceed to the optimization of the three variables it employs: the QIPBTAG event cut, the gradient of the cut line in the jet energy / significance plane and the intercept of the cut line. Note that b tagging in the 4-jet environment is more demanding than the conventional case because jets tend to be less well separated and a double tag is required. The lifetime signal is also reduced due to the lower jet energy producing b hadrons with a smaller boost and less significant vertices.

The following tag performance results are derived using the $MEMC_4$ sample. The cuts were optimized by varying all three parameters and selecting the best combination in terms of double tag purity and efficiency and minimal contamination from udsc events.

We begin by focussing on the performance of the event cut in removing udsc events, ignoring for the moment the double tag performance. Figure 6.6 displays the results obtained in terms of the purity and efficiency with which the cut selects b events from the 5 flavour $MEMC_4$ sample. The final analysis uses an event cut value of 0.02 which combines an efficiency of 56% with a purity of 78%. This point was selected by considering the double tag performance as well as the udsc contamination as explained below.

The optimization of the three parameters was performed by holding the QIPBTAG event cut fixed while the intercept and gradient of the vertex significance / jet energy cut line scanned a range of values. The process was then repeated at a variety of event cut values. In calculating purities and efficiencies a b event in which fewer than 2 b jets are correctly identified counts as a failed tag, and the rare case of $b\bar{b}b\bar{b}$ events is ignored as they form less than 0.02% of the MC sample.

The upper plots in Figure 6.7 show the performance of the combined tag for a fixed event cut and a range of intercept and gradient values. The lower plots show straight line fits to the same data which help to quantify the performance of each event cut value. Figure 6.8 shows straight line fits to the purity vs. efficiency plot for several event cut values. This information was used to select the event

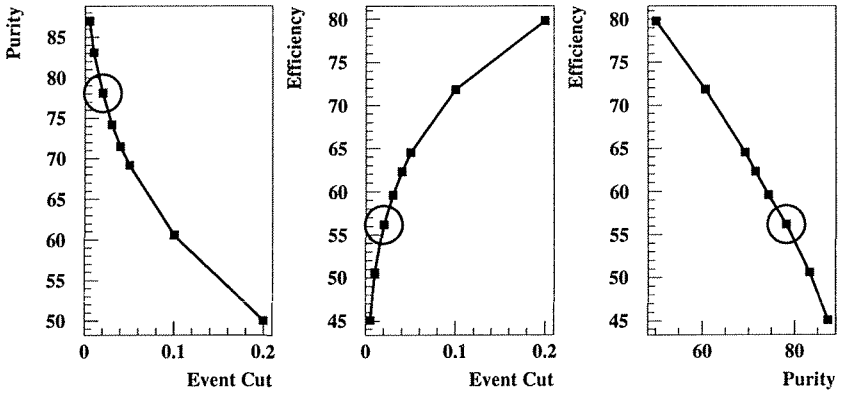

Figure 6.6: The performance of the QIPBTAG event cut. The left hand plot shows the purity and the centre plot the efficiency with which the cut selects b events from the 5 flavour $MEMC_4$ sample. The right hand plot shows the efficiency as a function of purity. The circles denote the point used in the final analysis.

cut value of 0.02 used in the final analysis as it provides the best performance.

The intercept and gradient values used in the final analysis of 45 and -5.7 respectively were chosen so as to maximize the efficiency of the tag while maintaining a meaningful tag purity. The final values of purity, efficiency and udsc contamination are shown in the following table where the errors quoted are statistical only.

purity	efficiency	udsc contamination
$58.4 \pm 1.3\%$	$21.4 \pm 0.5\%$	$12.0 \pm 1.6\%$

6.4 Monte Carlo Studies

For the purpose of correcting the b sample a dedicated set of Monte-Carlo events was generated in order to improve the statistical coverage of b events provided by the $MEMC_4$ sample. This was achieved by combining 249,822 4-parton MEMC

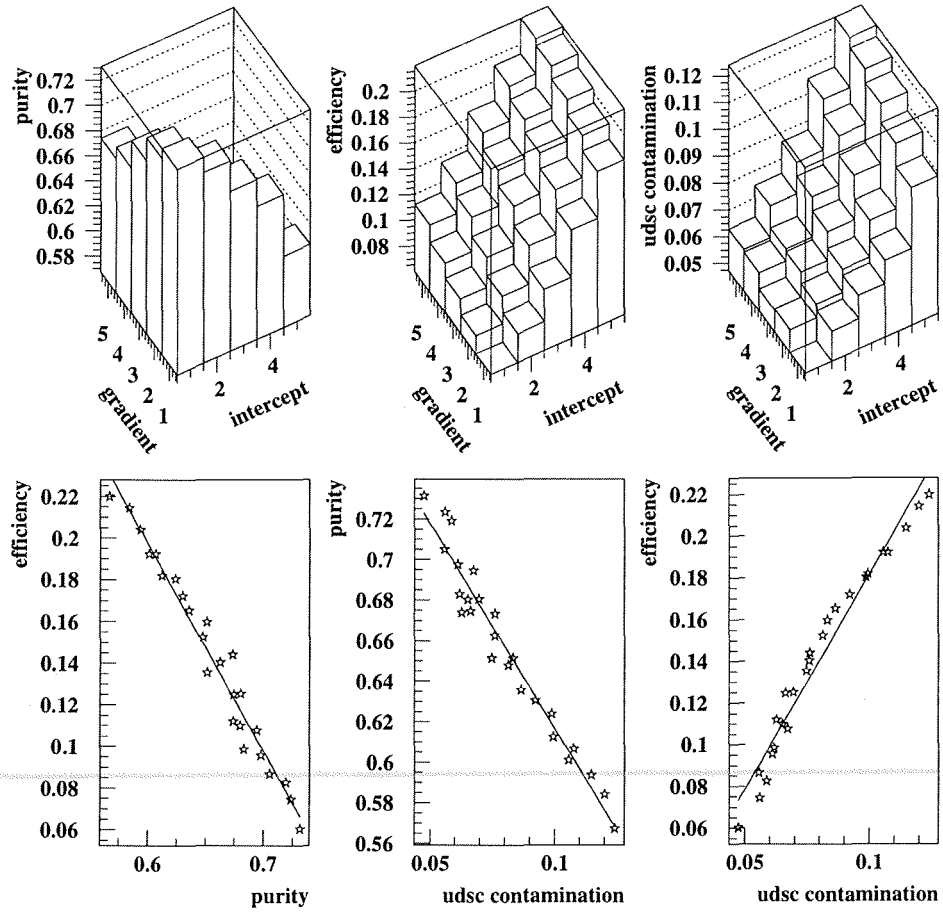

Figure 6.7: The purity, efficiency and udsc contamination performance of the combined tag for an event cut of 0.02 and a range of cut line gradient and intercept values. The intercept and gradient axis is marked in arbitrary units.

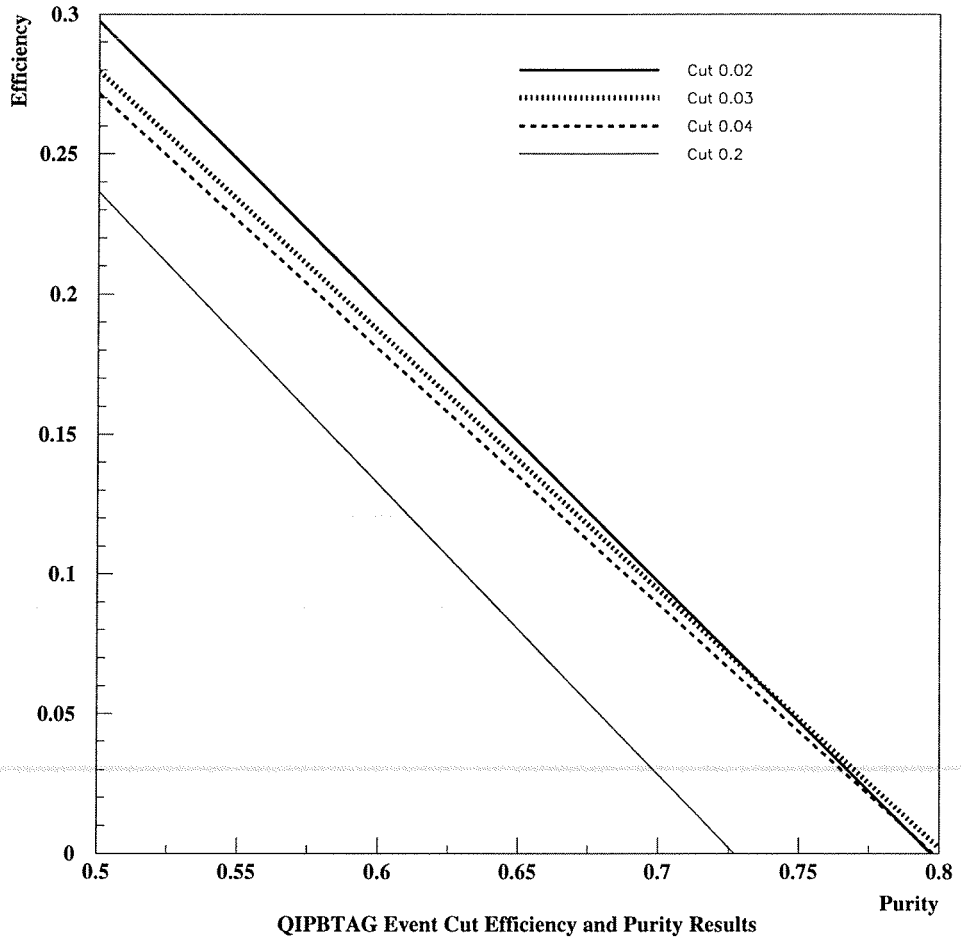

Figure 6.8: The straight line fits to the double tag purity as a function of efficiency for a range of event cut values.

events which all have $b\bar{b}$ primary quarks with a set of udsc events from the MEMC_4 sample which were included in the correct proportion to reproduce the measured 12% contamination.

The $b\bar{b}$ events were subject to exactly the same selection criteria as the data b sample. However the QIPBTAG event cut was turned off for the udsc events in order to provide a sufficient number of background events without having to generate another large Monte-Carlo sample. The following table displays the details of this new MEMC_b sample as it will be referred to.

MEMC_b Sample	
Total No. $b\bar{b}$ events	249,822
No. double tagged $b\bar{b}$ events	8263
No. double tagged udsc events	1127
Total No. double tagged events	9390

In the remainder of this Section we compare the appearance of variables relevant to the tagged analysis in data (b sample) and Monte-Carlo (MEMC_b sample). The good agreement displayed in Figure 6.9 gives us confidence that inter-jet angles and jet energies in the b sample are reasonably well modelled by the Monte-Carlo. The overall shape of the event is measured in the plots shown in Figure 6.10 where again we see a reasonable agreement between the two samples. The finer details of the jet development also seem to be reproduced by the Monte-Carlo, as can be seen in Figure 6.11.

In Figure 6.12 we see that the impact-parameter and QIPBTAG probabilities agree well in the data and Monte-Carlo, while Figure 6.13 displays a slightly poorer agreement for the vertex significance which shows a tendency towards more separated vertices in the MC. This is thought to be caused by an underestimation of quantities which degrade the tracking quality leading to a smaller error on tracks and hence vertices in the MC. This leads to a slightly different b selection rate from the total 4-jet sample of $6.4 \pm 0.1\%$ in the data compared with

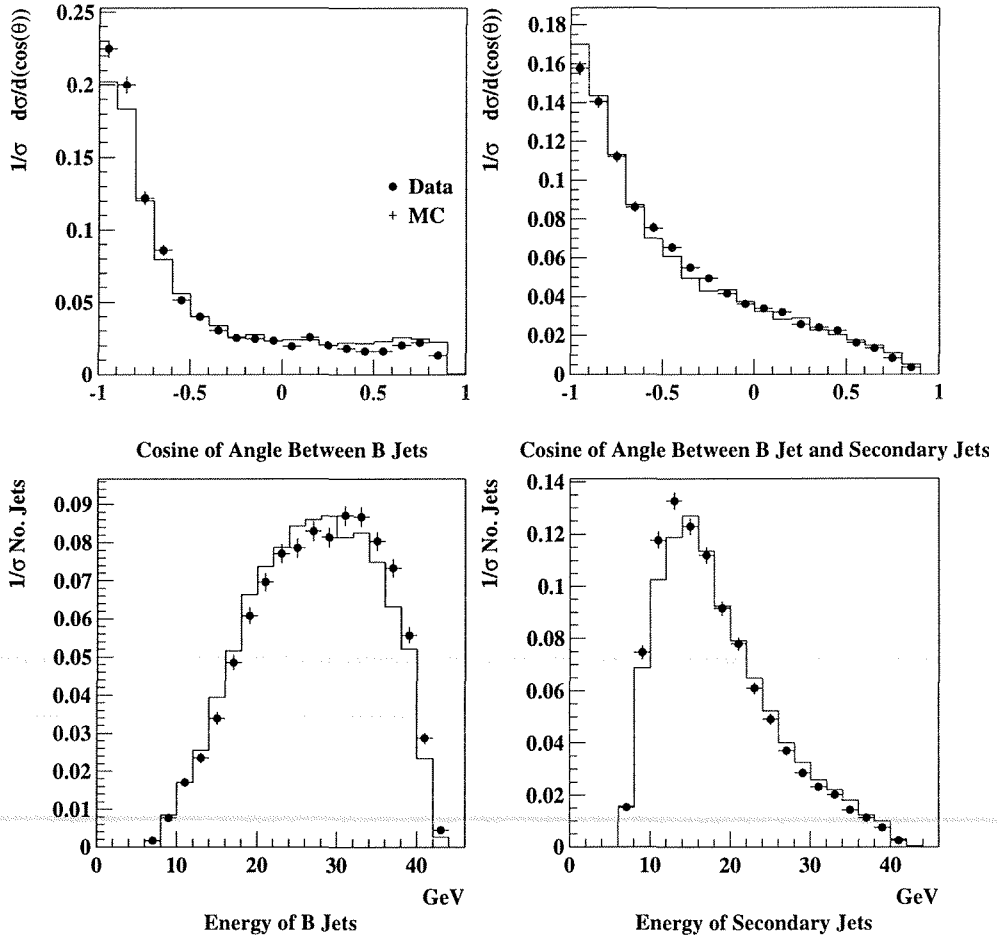

Figure 6.9: The top left plot shows the cosine of the angle between the two tagged jets, while the top right plot displays the angle between the hardest tagged jet and the two secondary jets, for both data and Monte-Carlo. The lower two plots show the tagged jet energy and the secondary jet energy.

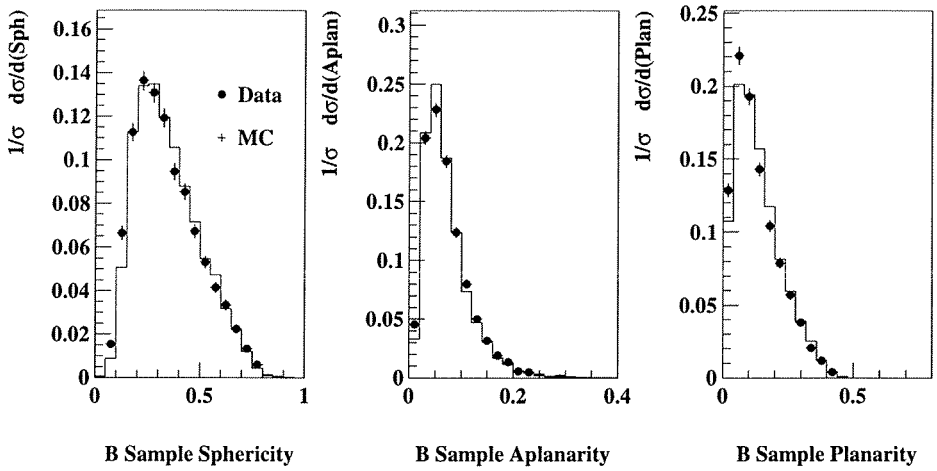

Figure 6.10: The event shape variables introduced in Section 4.4.2 for the data b sample and the MEMC$_b$ sample.

the $8.8 \pm 0.2\%$ in the Monte-Carlo (statistical errors only). This is not considered to be a major problem as the analysis takes no account of the number of events in the sample. Also, the final Colour Factor measurement has been shown to be insensitive to the purity of the b sample as explained in Chapter 7.

We conclude the Section by displaying the ACV's measured in each sample. In these plots the variables have been plotted in 'tag' order with the b jets in position one and two, the secondary jets in position three and four, and with each pair energy ordered. The close agreement shown in Figure 6.14 gives us confidence that the analysis is insensitive to any discrepancy between the data and Monte-Carlo.

6.5 Correction Procedure

The MEMC$_b$ sample introduced above is used to correct the data following the procedure set out in Section 4.6. The principle of applying a multiplicative cor-

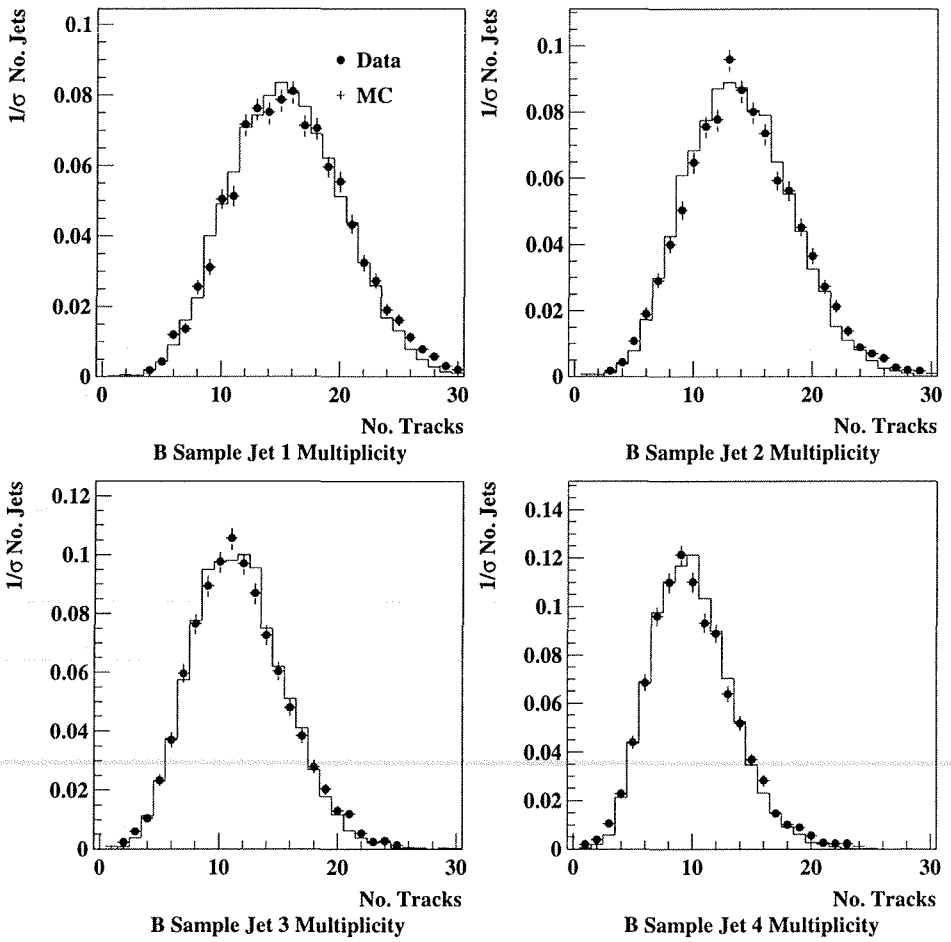

Figure 6.11: The total jet multiplicity for each jet in the data b sample and the MEMC_b sample. The jet numbers refer to 'tag' ordering.

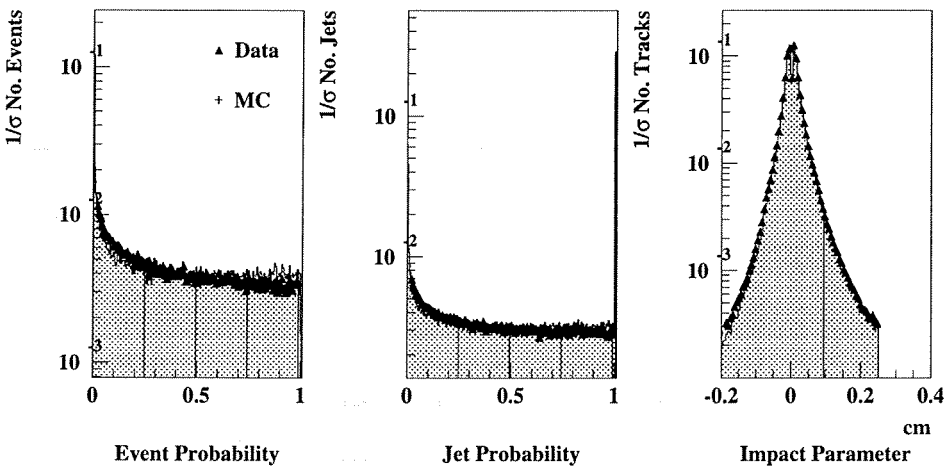

Figure 6.12: The QIPBTAG event and jet probabilities in data and Monte-Carlo ($MEMC_4$). The right hand plot displays the track impact parameter for both samples.

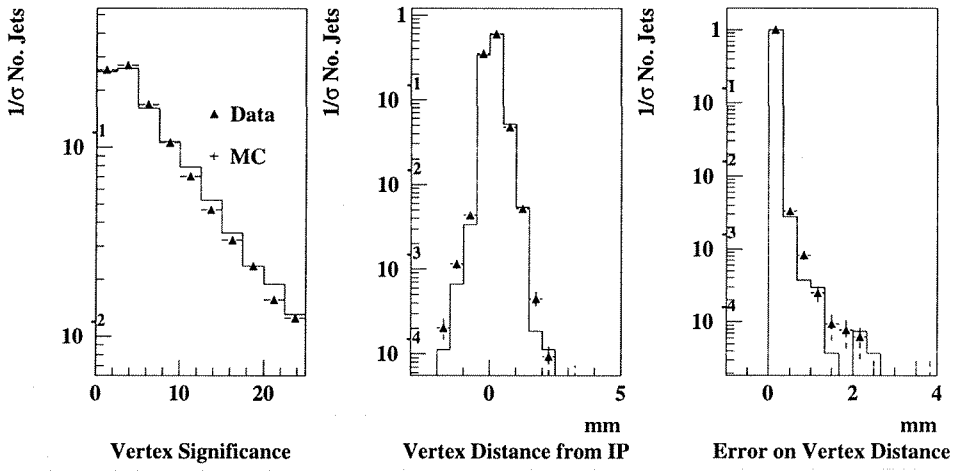

Figure 6.13: The QVSRCH vertex significance in data and Monte-Carlo ($MEMC_4$). The centre plot shows the the distance of the vertex from the interaction point and the right hand plot shows the error on this quantity.

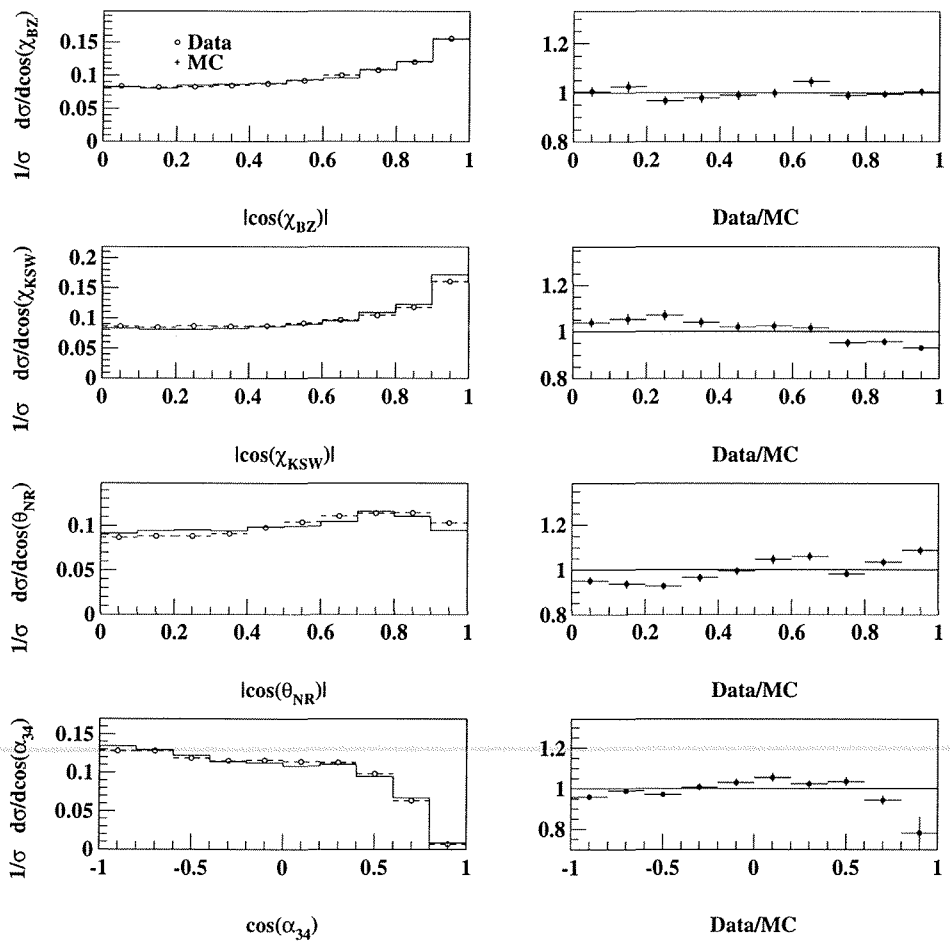

Figure 6.14: The ACV distributions measured in the data (b sample) and Monte-Carlo (MEMC$_b$ sample).

rection factor to compensate for the effects of the detector and hadronization and thus obtain distributions which reflect PARTON level ACV's is unchanged.

Figure 6.15 shows the MEMC_b derivation of the correction function. It has been divided into two elements, the first of which shows the effect of tagging the wrong jet. This is a large effect as only 58% of b events are free of mis-tags, and highlights the fact that we require the MC correction to work harder for us here than in the udsc sample. The second element is the combined effect of the detector and hadronization assuming perfect tagging. This second distribution shows much the same form as the combined correction function derived for the udsc sample. At the foot of the plot the two elements are combined to produce the final correction function which we see applied to the data in Figure 6.16. The reasonable regularity of this final correction function gives us confidence that the ACV's are fairly insensitive to the effects of mis-tagging, hadronization and the detector, and that the corrected distributions give a reasonable description of parton level processes.

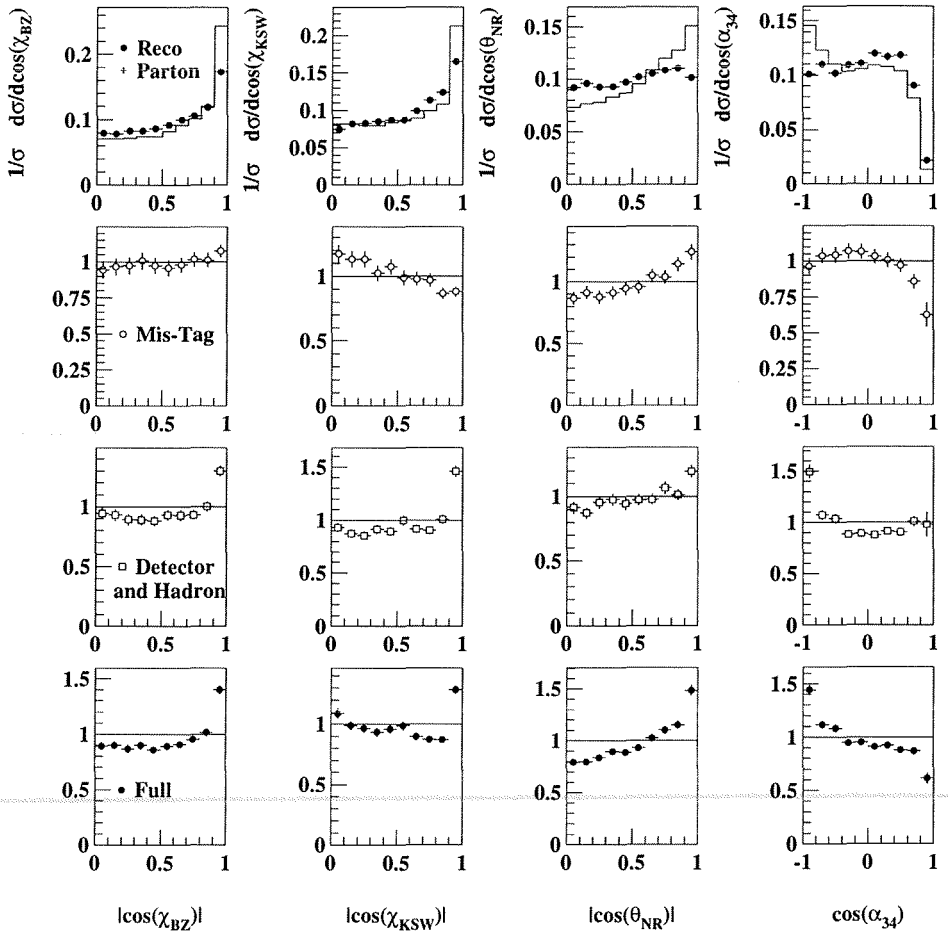

Figure 6.15: The b sample Monte-Carlo correction function. The plots in the second and third row show the correction function divided into a mis-tagging component and a detector and hadronization component. The bottom plots show these two elements combined into the full correction function.

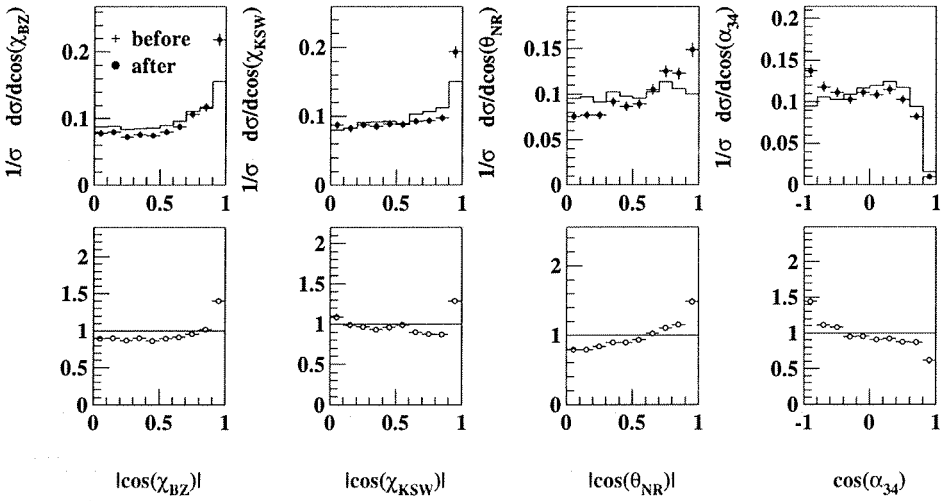

Figure 6.16: The data b sample before and after the application of the multiplicative correction factor derived from the MEMC$_b$ sample, which is shown in the lower plots.

Chapter 7

Results

This Chapter introduces the fitting techniques used to obtain Colour Factor values from measured ACV distributions and then shows the results obtained from the b and udsc data samples. In the final Section a full error analysis is presented which covers statistical, theoretical and systematic effects.

7.1 Fitting Procedure

The principle of extracting Colour Factor values from angular distributions was introduced in Section 4.1. The first step is to separate the contribution of the three processes to the 4-jet cross-section in an $\mathcal{O}(\alpha_s^2)$ QCD matrix element calculation. This facilitates the generation of ACV distributions divided into three components, each multiplied by a ratio of Colour Factors. Finally we perform a minimum χ^2 fit of these components to the corrected data with the Colour Factors as free parameters. The fit takes into account the correlations between the ACV's as explained in Section 7.1.2. The fit was performed using a minimization program [55].

7.1.1 QCD Matrix Element Calculations

Using a program originally written by Paulo Nason which combines a random-number generator with an $\mathcal{O}(\alpha_s^2)$ matrix element calculation [41] we can obtain

simulated 3 and 4 parton configurations with weights corresponding to their probability as predicted by 2^{nd} order QCD. For 4 parton events, this weight has been separated into contributions proportional to Colour Factor expressions. These weights provide the α, β and γ terms shown below, where y denotes some general variable.

$$\frac{1}{\sigma_{tot}}\frac{d\sigma}{dy} = \left(\frac{\alpha_s C_F}{\pi}\right)^2 \left[\alpha(y) + \frac{C_A}{C_F}\beta(y) + \frac{T_R}{C_F}\gamma(y)\right]$$

In practice we select 4 parton configurations and for each event which passes the minimum y_{cut} used in the main analysis we calculate the corresponding ACV value. We then plot the weight of the event as a function of the ACV value for each of the three α, β and γ terms. This gives us predictions for the ACV's correct to 2^{nd} order in QCD which explicitly show the contribution of each Colour Factor. In Figure 7.1 we see an example of this separation for the α_{34} variable, together with the recombination of the three terms assuming the QCD values of the Colour Factors.

The above technique, which will be referred to as the Ellis, Ross and Terrano or ERT calculation was repeated using another set of $\mathcal{O}(\alpha_s^2)$ matrix element calculations which include quark masses [42], hereafter referred to as the massive matrix element or MME calculation. A program was provided which generated parton configurations and weights as before. The separation into the α, β and γ contributions was performed with advice from one of the authors, Ezio Maina. It has been shown that the new program reproduces the results of the ERT calculation in detail for the case of massless quarks.

The MME calculation was used in the fit for the b sample because the b quark mass has a large influence on the shape of the ACV distributions and cannot be neglected. Figure 7.2 shows a comparison of the MME and ERT predictions for the $b\bar{b}q\bar{q}$ contribution to the χ_{BZ} variable ($\gamma(\chi_{BZ})$). In the plot there are differences introduced by the b quark mass which is ignored in the ERT calculation.

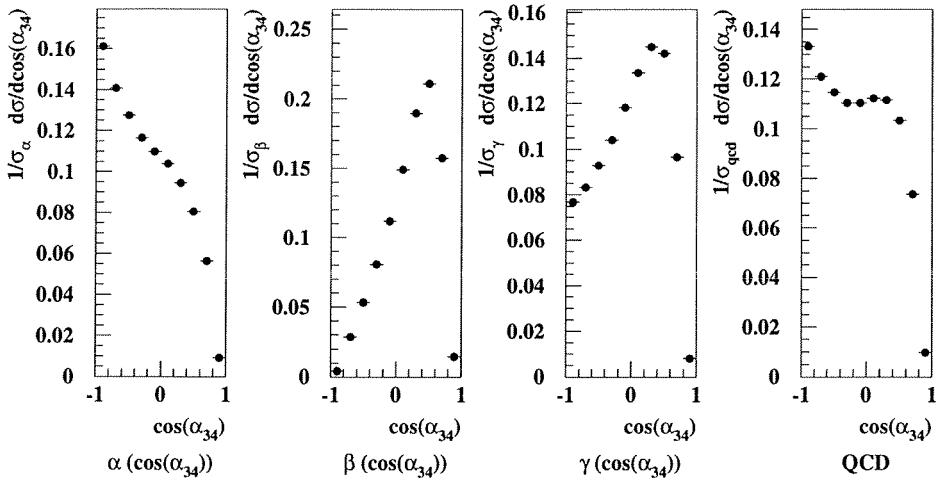

Figure 7.1: The contribution to α_{34} from the α, β and γ terms, together with the QCD combination. Each plot has been individually normalized to unit area.

The MME result assumes all events arise from an initial $b\bar{b}$ pair and are 'tag' ordered with the primary quarks in position 1 and 2, as is the case for the MEMC$_b$ sample at PARTON level. It uses a b quark mass of 5 GeV, a c quark mass of 1.5 GeV, and has all other quark masses set to zero.

Mass effects were assumed to be negligible for the light quark udsc sample which uses the ERT result. As a check of the validity of this assumption the MME routine was used to create a test sample of events in which a c quark mass of 1.5 GeV was included in the calculation. Figure 7.3 shows a comparison of this calculation with the ERT result for the γ contribution to the χ_{BZ} variable. It can be seen from the plot that the c quark mass has negligible impact.

7.1.2 Correlations

In this Section we consider how to deal with correlations between bins in a one dimensional fit. The problem can be summarized as follows. In the case where two bins are completely correlated they contain exactly the same information. In

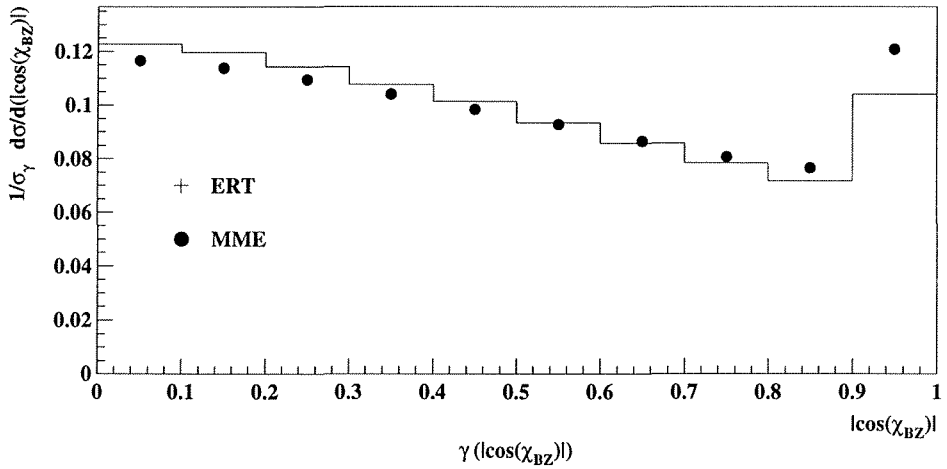

Figure 7.2: A demonstration of the impact of quark masses in the 4 quark (γ) distribution of $|cos(\chi_{BZ})|$. The plots show the $b\bar{b}q\bar{q}$ contribution in the ERT and MME schemes.

a normal fit this information would enter the χ^2 once for each bin and so receive double the correct weight.

In order to solve this problem the fit used here accounts for correlations between ACV's by de-weighting the contribution of correlated bins in the χ^2 and thus avoids double counting. It achieves this by calculating the covariance between all bins as explained below. For the purpose of performing the fit the four ACV's are concatenated together into a single long 1-dimensional vector as shown in Figure 7.4. Each ACV has been plotted with 10 bins, giving the composite vector a total of 40 bins.

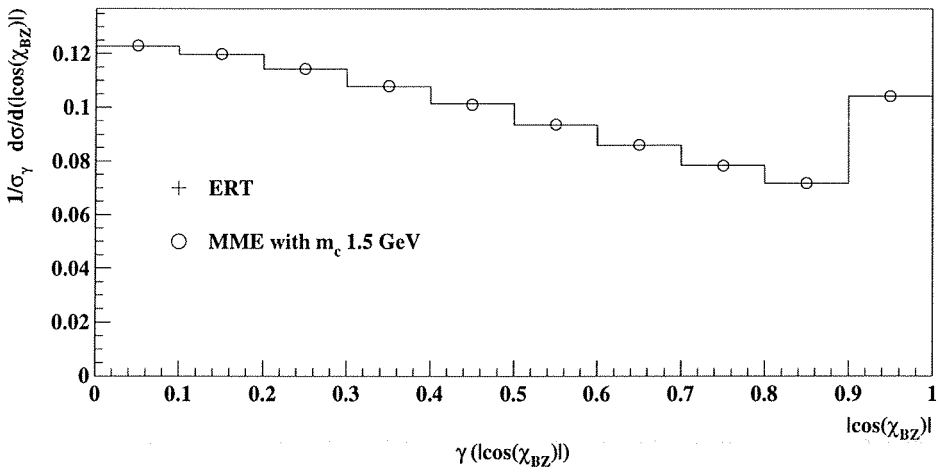

Figure 7.3: A comparison of the ERT prediction with the MME calculation with only the c quark mass included. The plots are of the 4 quark (γ) contribution to $|cos(\chi_{BZ})|$.

Figure 7.4: The long 1-dimensional vector containing all 4 ACV's.

At the time of analysis 2-dimensional plots of the correlation between each pair of ACV's were recorded in the data and Monte-Carlo samples. This allows the covariance matrix for each pair to be constructed, following the definition of the covariance of two variables [56].

$$\boldsymbol{cov(x,y)_{ij} = \frac{1}{N} \sum_i \sum_j [f(x,y)_{ij}\, x_i y_j] - \mu_x \mu_y}$$

In the above equation the x and y variables represent any pair of (different) ACV's. The $cov(x,y)_{ij}$ symbol denotes the (i,j) entry in the covariance matrix, $f(x,y)_{ij}$ is the (i,j) entry in the 2-dimensional histogram of x and y, N is the total number of entries in the histogram, x_i, y_j are the variable values at position (i,j) and μ_x, μ_y are the means of the two variables.

The 2-dimensional plots were constructed separately for the udsc and b samples, and corrected using the relevant MEMC sample for detector and hadronization effects. Following the method outlined in Chapter 4 a multiplicative correction function was constructed from the ratio of the RECO and PARTON level MEMC distributions. This was applied to the data before construction of the covariance matrix. In Figure 7.5 we see an example of the 2-dimensional matrix for χ_{BZ} and χ_{KSW}.

Having obtained the 2-dimensional $f(x,y)$ matrix for each pair of variables we then calculate the covariance between each bin as given in the formula above. The six ACV pairs are then concatenated together into one 40×40 entry matrix containing all the correlation terms from the 4 ACV's. The diagonal entries were obtained assuming that each ACV is uncorrelated with itself. This is equivalent to ignoring inter-bin transitions as discussed in Section 5.4.3. The resulting ACV covariance matrix as it will be referred to is displayed, together with its inverse obtained using a numerical algorithm, in Figure 7.6.

To complete the discussion of correlations between ACV's we present the χ^2 used in the fit. For each bin in the 1-dimensional ACV vector the fit constructs a contribution weighted by the relevant row in the cov^{-1} matrix, such that the total

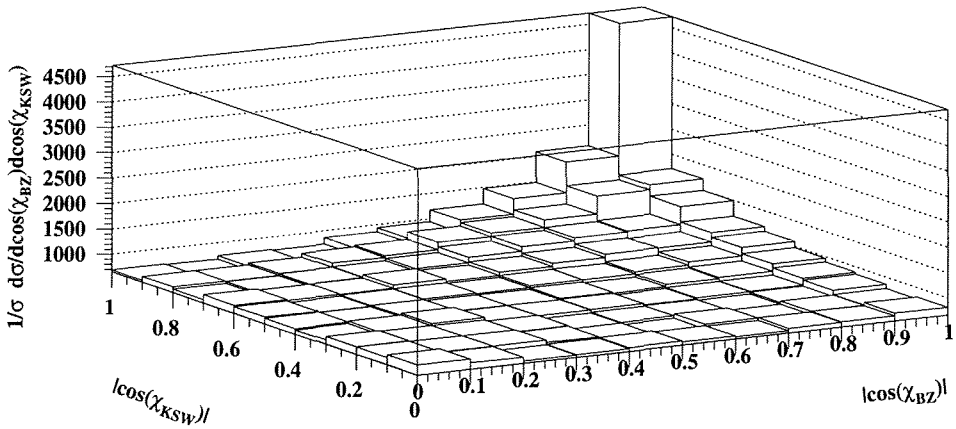

Figure 7.5: The 2-dimensional histogram of the χ_{BZ} and χ_{KSW} variables, $f(\chi_{BZ}, \chi_{KSW})$.

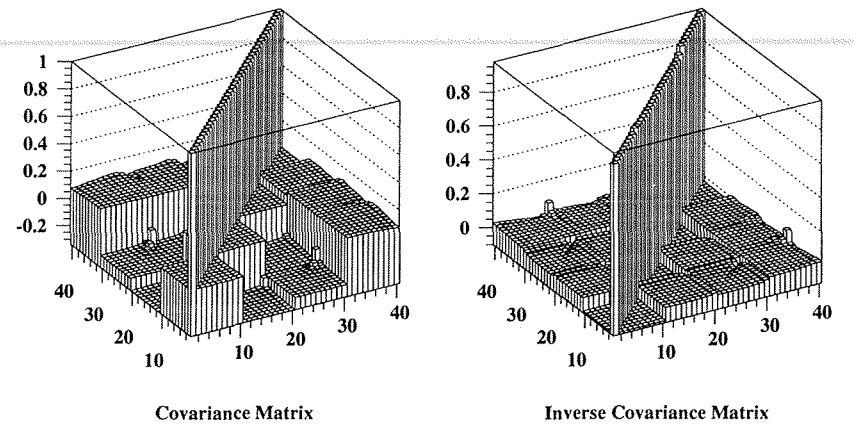

Figure 7.6: The covariance matrix (cov) of all 4 ACV's combined. The right hand plot shows the inverse of this matrix (cov^{-1}) as used in the χ^2 definition.

weight for each bin is one, and all correlations are accounted for. It also explicitly includes the combined statistical uncertainty of the data and Monte-Carlo correction function ($error_i$) as no error information is included in the covariance matrix.

$$\chi^2 = \sum_i \sum_j \left[\frac{\delta_i \ (cov^{-1})_{ij} \ \delta_j}{error_i \ error_j} \right]^2$$

In the above expression the δ_i vector represents the difference between the i^{th} bin of the long ACV data vector ($data_i$) and the i^{th} bin of the linear combination of the three components of the theory prediction ($theory_i$), i.e.

$$\begin{aligned} \delta_i &= data_i - theory_i \\ theory_i &= A\alpha_i + B\beta_i + C\gamma_i \end{aligned}$$

where the A,B,C are the free parameters in the fit.

7.2 Fit Results

We now present the result of the udsc sample fit. In Figure 7.7 we see the corrected data distribution together with the fitted function. The result obtained is shown below where the quoted errors are statistical in nature.

$$\frac{C_A}{C_F} = 2.286 \pm 0.129 \qquad \frac{T_R}{C_F} = 1.393 \pm 0.309$$

The χ^2 value of 59.84 for 37 degrees of freedom gives confidence that the result is stable and the theory predictions provide a reasonable description of the data. The fitted value in bin 20 is significantly lower than the data. The Monte-Carlo correction for this bin shown in Figure 4.22 approaches 30% and the discrepancy is subsequently considered an artefact of some limitation in the Monte-Carlo modelling of the hadronization process. The correlation coefficient between the two quantities is shown below.

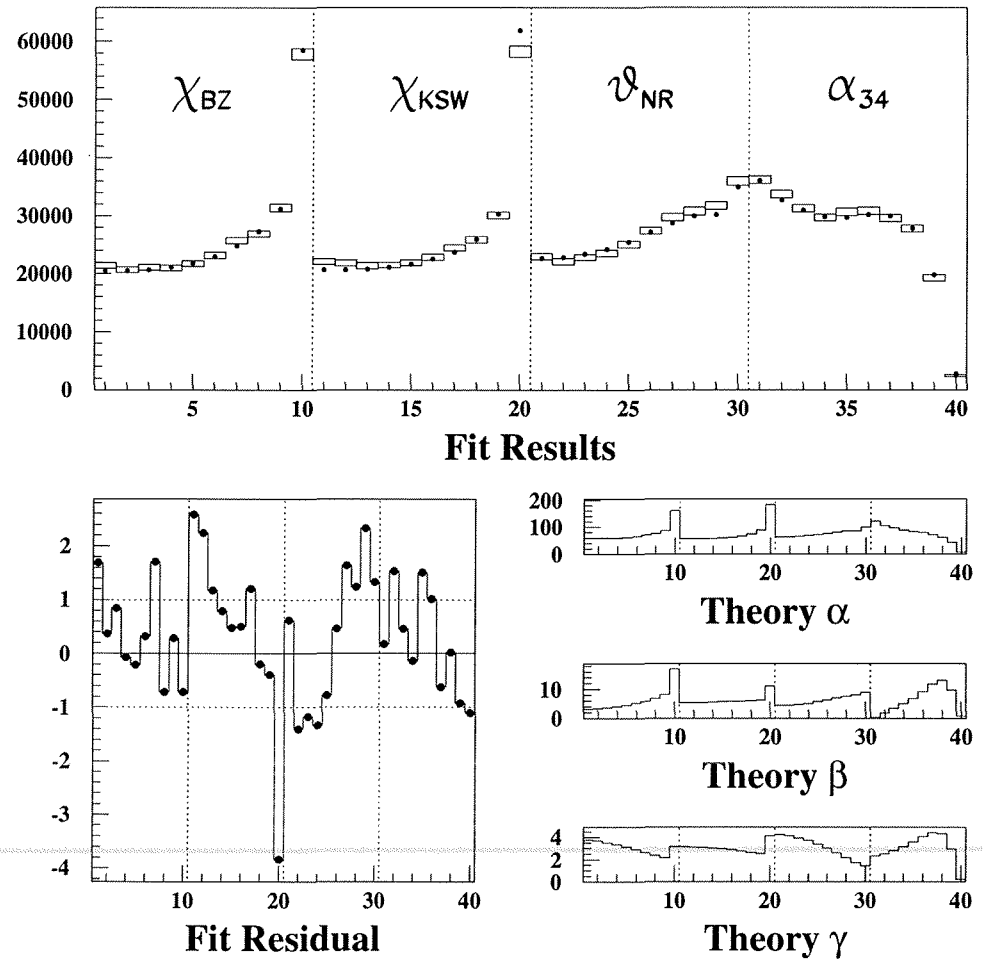

Figure 7.7: The result of the udsc sample fit. The top plot shows the data vector after all corrections have been applied. The boxes indicate the size of the statistical error while the dots show the fit. The bottom left plots shows the fit residuals in units of significance = (data - fit)/error. The bottom right plots show the three theory distributions α, β, γ.

$$\frac{cov(\frac{C_A}{C_F},\frac{T_R}{C_F})}{\sigma_{\frac{C_A}{C_F}}\sigma_{\frac{T_R}{C_F}}} = \rho(\frac{C_A}{C_F},\frac{T_R}{C_F}) = -0.424$$

The b sample fit is shown in Figure 7.8. The result obtained is shown below.

$$\frac{C_A}{C_F} = 2.298 \pm 0.091 \qquad \frac{T_R}{C_F} = 2.347 \pm 0.913$$

In this fit we have a χ^2 value of 41.80 for 37 degrees of freedom. The correlation coefficient between the two quantities is $\rho(\frac{C_A}{C_F},\frac{T_R}{C_F}) = -0.338$.

The two fits above arise from statistically independent samples and can be combined to produce the weighted average shown below where the errors are again statistical.

$$\frac{C_A}{C_F} = 2.294 \pm 0.074 \qquad \frac{T_R}{C_F} = 1.491 \pm 0.293$$

Figure 7.9 shows the results displayed on the $\frac{C_A}{C_F}, \frac{T_R}{C_F}$ plane.

7.3 Error Analysis

The accuracy of the Colour Factor measurement is limited by two factors: the number of events in the sample and the shortcomings of the method used to extract Colour Factor values. The aim of this Section is to assess the contribution of each to the final error.

7.3.1 Statistical Errors

The statistical uncertainty is obtained from the fitting routine [55]. It is related to the steepness of the minimum found by the minimization algorithm which is in turn related to the statistical accuracy of the input sample. This is given by the sum in quadrature of the bin by bin statistical errors on the data and Monte-Carlo samples. The errors produced by the fit were checked in the region around the minima and found in all cases to be symmetric. The limited Monte-Carlo statistics give a small but significant contribution to the udsc sample error. However when we consider the impact of systematic uncertainties the improvement in the overall accuracy obtained by removing this contribution would be negligible.

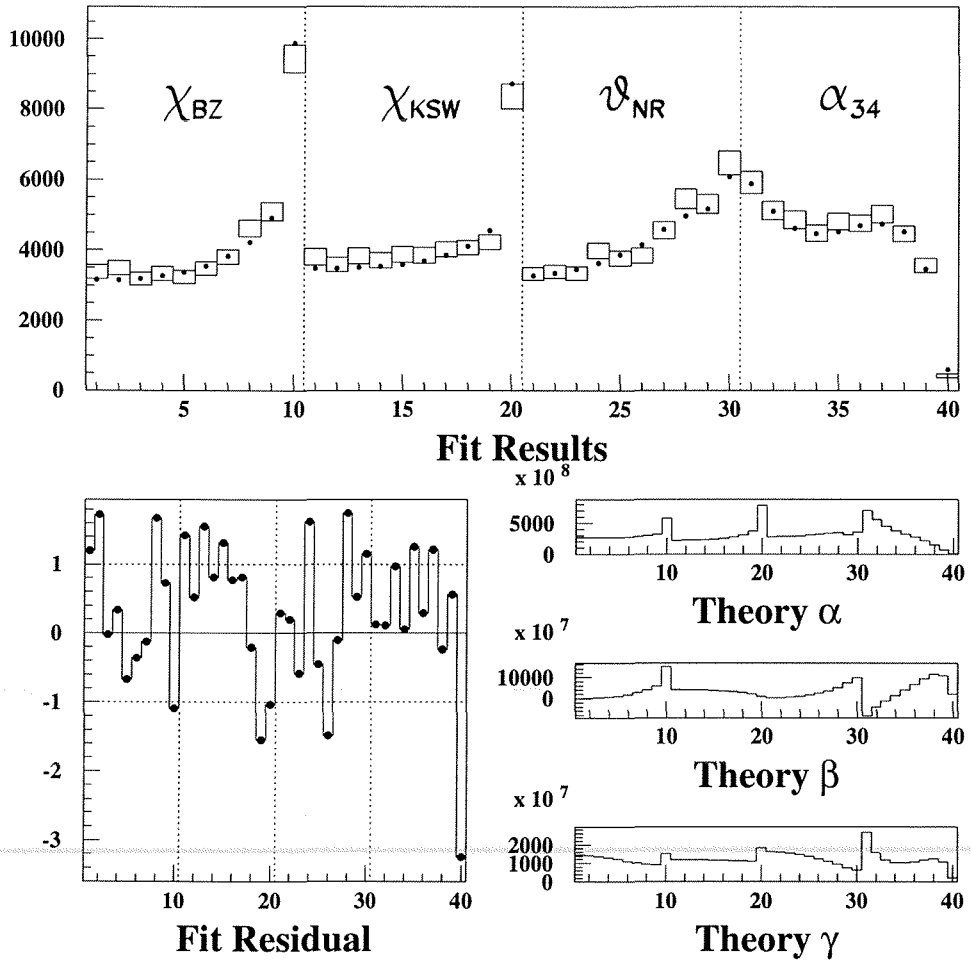

Figure 7.8: The result of the b sample fit. The top plot shows the data vector after all corrections have been applied. The boxes indicate the size of the statistical error while the dots show the fit. The bottom left plots shows the fit residuals in units of significance = (data - fit)/error. The bottom right plots show the three theory distributions α, β, γ.

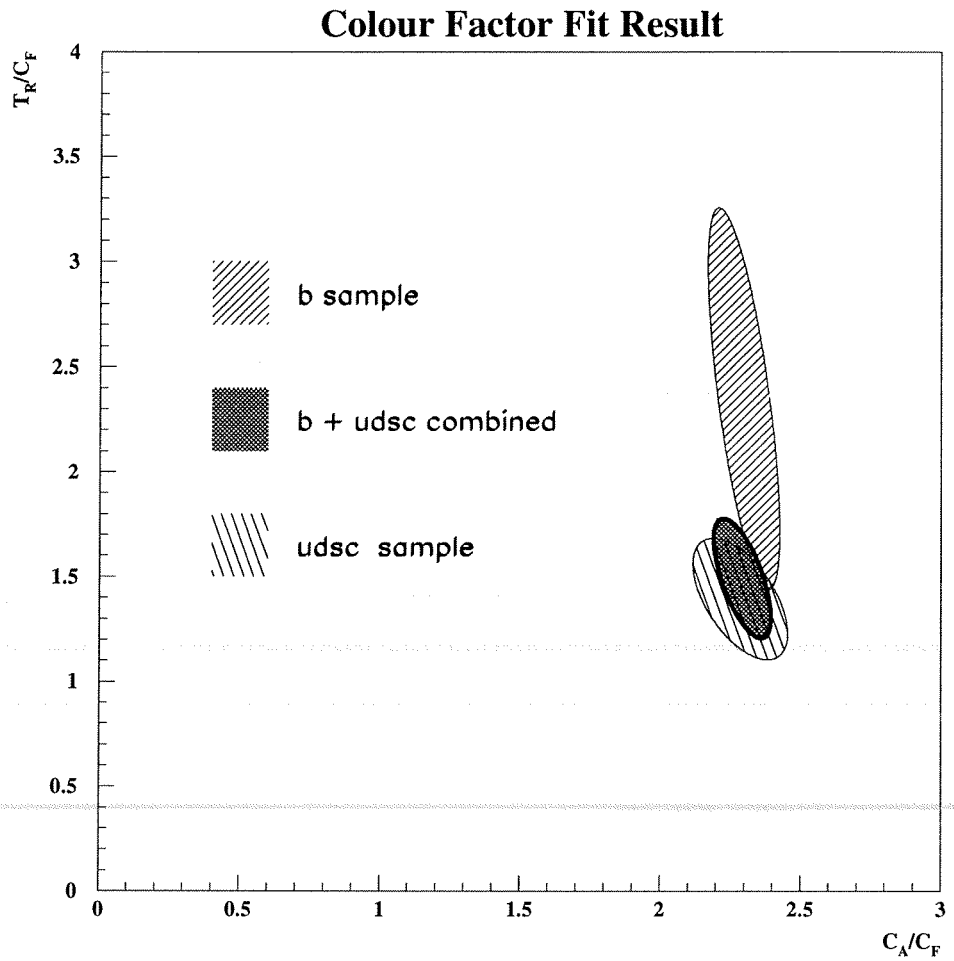

Figure 7.9: The result of the udsc and b sample fits shown in the $\frac{C_A}{C_F}, \frac{T_R}{C_F}$ plane. The combined result is also shown. The ellipses represent 1 σ statistical errors.

7.3.2 Theoretical Errors

Theoretical predictions enter the fit through the α, β and γ functions used to construct the *theory* vector. They could degrade the accuracy of the final result in two ways. They could contain insufficient statistics and thus lead to some blurring of the contribution from each event type, or they could fail to describe the data correctly. The two cases are discussed below.

Matrix Element Predictions

The statistical error from the matrix element predictions is considered to be negligible as they are derived from samples of considerably larger size than the data. The massless result used in the udsc fit is derived from a sample of 50 million events which exceeds the data sample by a factor of more than ten. The massive quark result used in the b fit is derived from a 10 million event sample which is larger than the data sample by a similar factor. This allows any contribution to the error on the final result from this source to be ignored.

The possibility that the matrix element predictions contain some calculation error is discounted by the fact that the ERT and MME predictions have been shown to agree exactly in the case of massless quarks as discussed in Section 7.1.1.

Higher Order Effects

The analysis carried out here is based on QCD predictions correct to $\mathcal{O}(\alpha_s^2)$. The influence of higher order terms in the perturbative expansion beyond this point could in principle alter the shape of the α, β and γ distributions and so change the Colour Factor values obtained.

It is possible to get a feel for the possible influence of unknown $\mathcal{O}(\alpha_s^3)$ terms by comparing the change observed in going from $\mathcal{O}(\alpha_s)$ to $\mathcal{O}(\alpha_s^2)$ in the three jet region. The 3 jet rate is known to experience a correction of up to 50% due to next-to-leading order terms, but the jet structure of these events does not vary significantly. Figure 7.10 displays the event-shape variable Thrust which was defined in Section 5.3 and is sensitive to the shape of two and three jet events. It

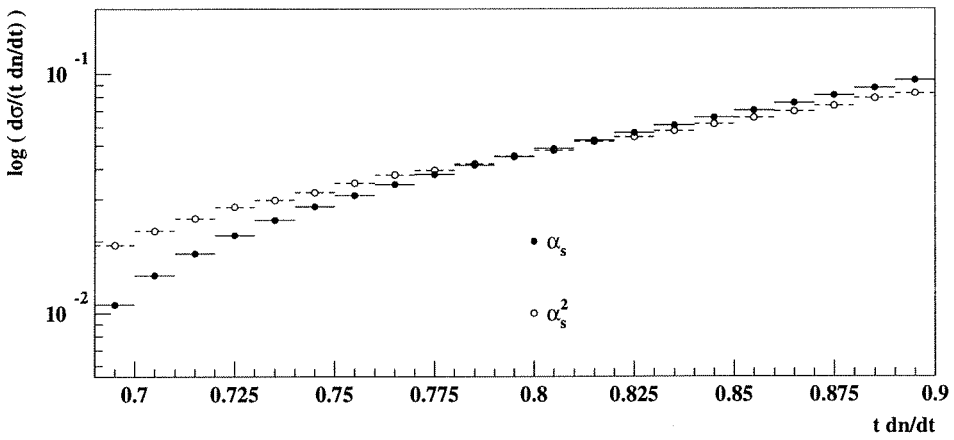

Figure 7.10: A comparison of the 1^{st} and 2^{nd} order predictions for the event-shape variable Thrust from the ERT matrix element calculation. Both distributions have been normalized to unit area.

demonstrates that significant deviations in the shape of the distribution do not occur when going from leading to next-to-leading order.

As this analysis is insensitive to the overall four jet rate it is hoped that the influence of next-to-leading order terms on the shape of the event as measured by the ACV's would again be small. In order to test this assumption we must await the results of $\mathcal{O}(\alpha_s^3)$ matrix element calculations. A full third order result is not yet available but a preliminary version which neglects terms suppressed by a factor $\frac{1}{N_{fun}^2}$ has recently been produced [57]. The suggestion that the ACV's used here are insensitive to these effects seems to be confirmed by the first results from this calculation [58] which show significant deviations in the four jet rate but little change in the shape of the ACV's.

7.3.3 Systematic Errors

The specific details of the analysis such as the choice of clustering algorithm or Monte-Carlo scheme can lead to biases in the final result which must be evaluated. In this Section we examine each element of the procedure in turn and attempt to gauge the impact on the final result.

Clustering Algorithm

The reasons for using the DURHAM algorithm were discussed in Chapter 5 which also justified the chosen y_{cut} value of 0.01. In order to evaluate the dependence of the result on these choices the full analysis was repeated on data and Monte-Carlo with different values of y_{cut} close to the original. In a third variant the JADE algorithm was used. In this case an equivalent y_{cut} value of 0.027 was used which selected the same total number of events as the nominal analysis. It was found that changing the combining algorithm did not alter the sample significantly so all of the variants employ the 'E' scheme.

The fit was only performed for the udsc sample as this employs the same clustering techniques as the b-tagged analysis. For each variant 5 million events were generated with the ERT matrix element calculation using the new clustering requirement.

The effect of the change is in all cases to include events in the sample from different regions of the 4-parton phase space. This has led to the three variations being combined in a single systematic error. The results are contained in the following table where the quoted errors on the Colour Factor ratios are statistical. The Δ entries refer to the numerical change with respect to the nominal result, and the 'sig' entries express the significance of these shifts by showing them in units of the statistical error on the new value. The χ^2 entries show the value of the χ^2 per degree of freedom which gives a measure of the fit quality.

Clustering Algorithm	$\frac{C_A}{C_F}$	$\Delta(\frac{C_A}{C_F})$	sig$(\frac{C_A}{C_F})$	$\frac{T_R}{C_F}$	$\Delta(\frac{T_R}{C_F})$	sig$(\frac{T_R}{C_F})$	χ^2
Durham $y_{cut} = 0.12$	2.202 ± 0.151	-0.084	-0.553	1.241 ± 0.356	-0.151	-0.425	1.487
Durham $y_{cut} = 0.008$	2.258 ± 0.106	-0.027	-0.260	1.128 ± 0.263	-0.265	-1.004	5.19
Jade $y_{cut} = 0.027$	2.173 ± 0.128	-0.113	-0.881	1.906 ± 0.411	0.513	1.248	2.89

Detector Simulation

The accuracy of the detector simulation program used to model the response of the detector to Monte-Carlo events has been examined by repeating the analysis using only charged tracks.

In general the response of a detector to neutral particles is open to greater uncertainty as there is no tracking information available against which to check the calorimeter signals. The possibility that some error in the modelling of this response introduces a bias is rigorously explored by removing all neutral particles from the analysis and comparing the results obtained. This step degrades the jet angular resolution δ_θ by 10% from the nominal value of 5.1° to 5.6°. The effect of the change on the measured values is shown below.

Systematic Check	$\frac{C_A}{C_F}$	$\Delta(\frac{C_A}{C_F})$	sig$(\frac{C_A}{C_F})$	$\frac{T_R}{C_F}$	$\Delta(\frac{T_R}{C_F})$	sig$(\frac{T_R}{C_F})$	χ^2
Charged Tracks Only	2.435 ± 0.192	0.149	0.777	1.266 ± 0.454	-0.127	-0.279	1.43

Initial and Final State Radiation

Photon radiation either from the e^+e^- before they annihilate or from quarks in the early stages of the perturbative shower can skew the topology of the event as it recoils from the emitted photon.

The initial state radiation (ISR) process tends to produce low energy photons at angles close to the beam pipe which usually escape undetected. In fact, only 5% of events contain an ISR photon of energy greater than 1 GeV so the influence on the overall topology is small. The energy calculation and re-clustering procedure reduces the impact further by preferentially removing events which have significant missing energy.

There is however a possible sensitivity in the analysis due to the following mismatch. The matrix element calculations used in the fit ignore ISR but the

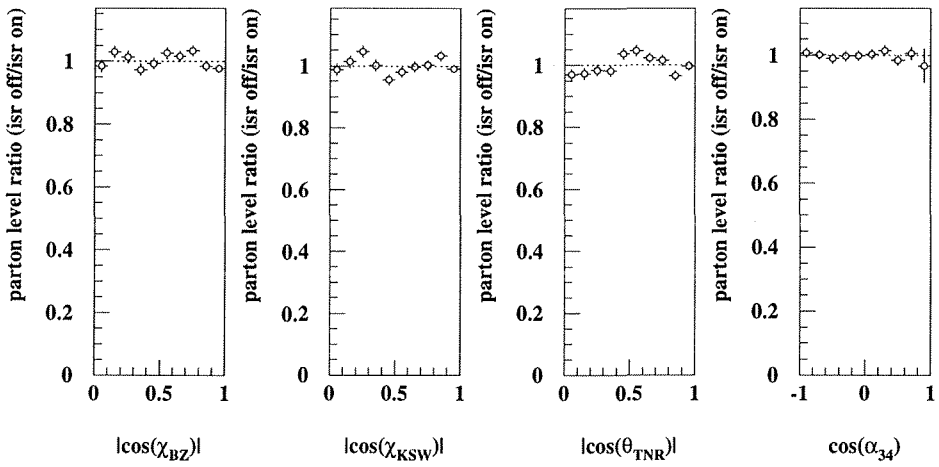

Figure 7.11: The ACV correction functions applied to the data to account for ISR effects.

partons produced in the Monte-Carlo used to correct the data have these effects included. To check the possible influence of this discrepancy a sample of Monte-Carlo parton events with the ISR effects removed was generated and a correction function for the ACV's created by taking the ratio of these parton level events to those with ISR included. This correction function is shown in Figure 7.11. The result of the fit after the correction function was applied is shown in the table below.

In the case of final state radiation from quarks the photon energy can be as high as 45 GeV and so could in principle have a large effect. The main problem arises in the high energy - high emission angle region where the photon could be mistaken for a hadronic jet and thus cause a 3-jet $q\bar{q}g$ event to mimic a $q\bar{q}gg$ or $q\bar{q}q\bar{q}$ event. This process is unlikely as the $q \rightarrow q\gamma$ cross-section favours soft and collinear emission and the electromagnetic coupling constant is much smaller than the strong coupling constant. However the possibility of contamination has been investigated by repeating the full analysis with the exclusion of any event

containing a jet in which the proportion of the jet energy due to a single photon exceeds 90%. The result of this analysis is shown below together with the result of the ISR corrected fit.

Systematic Check	$\frac{C_A}{C_F}$	$\Delta(\frac{C_A}{C_F})$	sig$(\frac{C_A}{C_F})$	$\frac{T_R}{C_F}$	$\Delta(\frac{T_R}{C_F})$	sig$(\frac{T_R}{C_F})$	χ^2
ISR	2.277 ± 0.161	-0.009	0.056	1.262 ± 0.387	-0.131	-0.339	1.79
FSR	2.288 ± 0.129	0.002	0.016	1.459 ± 0.310	0.066	0.211	1.62

Monte-Carlo Modelling of B Sample

The version of the Jetset Monte-Carlo used has been tuned to describe the ALEPH data [45]. However in order ensure that any deficiency in the description of b hadron decays does not introduce a bias in the results a check of the b-tag purity has been performed.

In the Monte-Carlo sample the estimated contamination from udsc events was found to be 12.0% as explained in Chapter 6. Any inaccuracy in the modelling of the vertex attributes or decay characteristics of the b sector would distort the tagging efficiency in the MC, resulting in an unreliable purity measurement.

In order to assess the impact of this effect on the results a set of MC correction functions were created at values of udsc contamination between 0% and 28%. The b sample fit was repeated with data corrected using each new function and the Colour Factor ratios plotted as a function of udsc contamination. Figure 7.12 shows the result for each ratio along with a straight line fit to the points, the parameters of which are shown below.

$$\frac{C_A}{C_F}_{impurity} = 2.231 + 0.443 \times impurity$$
$$\frac{T_R}{C_F}_{impurity} = 3.101 - 5.463 \times impurity$$

Using this fit the change in the results is estimated when the purity is varied from its measured value by $\pm 5\%$. The effects are shown in the table below where the Δ values are defined relative to the nominal b sample result. The errors on the Colour Factor ratios are taken from the uncertainty on the intercept value in the straight line fit.

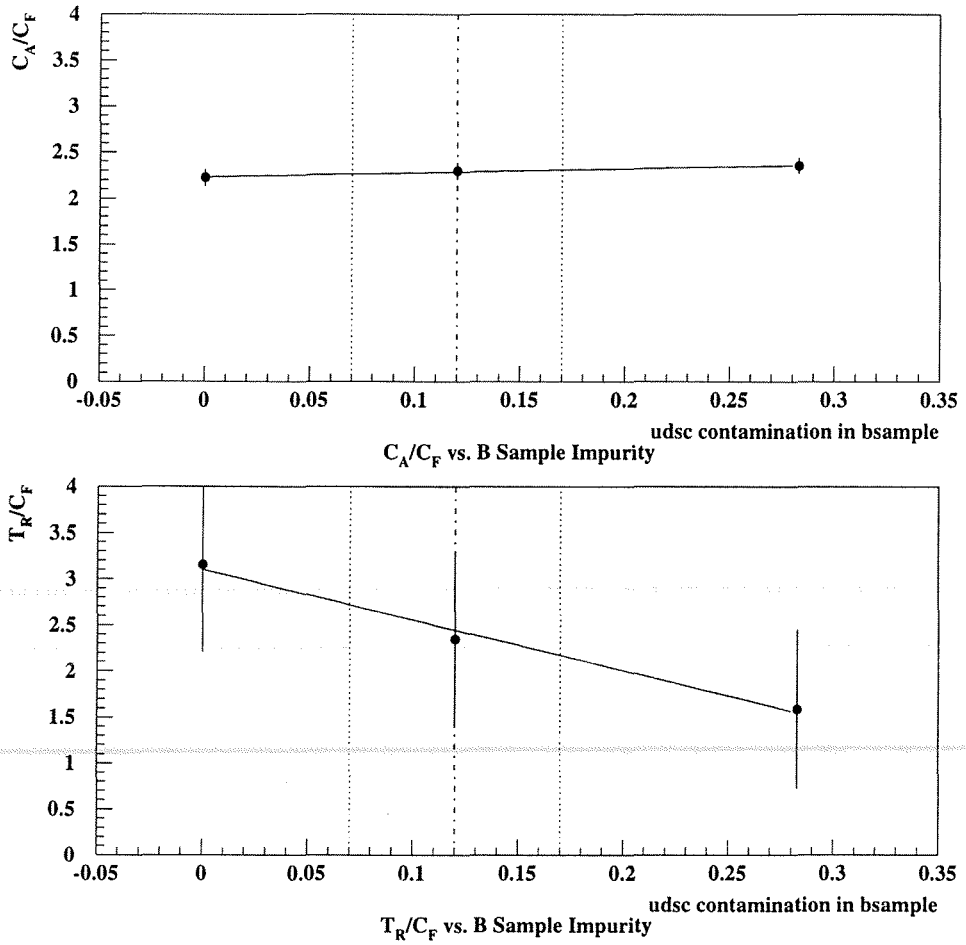

Figure 7.12: The variation of the Colour Factor ratios $\frac{C_A}{C_F}$ and $\frac{T_R}{C_F}$ as a function of b sample contamination from udsc events. The errors shown are statistical.

Systematic Check	$\frac{C_A}{C_F}$	$\Delta(\frac{C_A}{C_F})$	sig($\frac{C_A}{C_F}$)	$\frac{T_R}{C_F}$	$\Delta(\frac{T_R}{C_F})$	sig($\frac{T_R}{C_F}$)
b sample impurity 7%	2.262 ± 0.082	-0.026	-0.315	2.718 ± 0.830	0.371	0.448
b sample impurity 17%	2.306 ± 0.082	0.019	0.225	2.172 ± 0.830	-0.175	-0.211

Hadronization

As a further check of the Monte-Carlo dependence of the result a new sample of Monte-Carlo events was generated in which the hadronization parameters had been radically changed. This has the effect of altering the momentum spectrum of hadrons within jets which in turn influences the structure of the event.

The string fragmentation procedure used in the JETSET Monte-Carlo [8] was introduced in Section 1.3.3. One of the main parameters involved in the hadronization process is the longitudinal fragmentation function $f(z)$ which controls the momentum spectrum of the produced hadrons. It is possible to adopt different definitions but the version used in the JETSET Monte-Carlo is shown below. The z parameter describes the fraction of the remaining longitudinal momentum $(E + p_z)$ taken by a hadron produced in the break up of the string. The transverse mass is defined as $m_T^2 = E^2 - p_z^2$ where the z direction is defined as being along the string.

$$f(z) \propto \frac{(1-z)^A}{z} exp(\frac{-Bm_T^2}{z})$$

In this expression the A and B parameters are arbitrary and have been tuned to best fit the data. The two are highly correlated so in our adjustment the A parameter was left fixed at its nominal value of 1. The B parameter was changed from the fitted value given in Reference [45] of 0.496 ± 0.015 by five times the error on the fit to a value of 0.571. This change would tend to produce a harder momentum spectrum for the hadrons. The fragmentation function for the two cases is shown in Figure 7.13.

The sample was used to derive a new hadronization correction for the data and by combining this with the existing detector correction and fitting as before a new udsc result was obtained which is displayed in the following table.

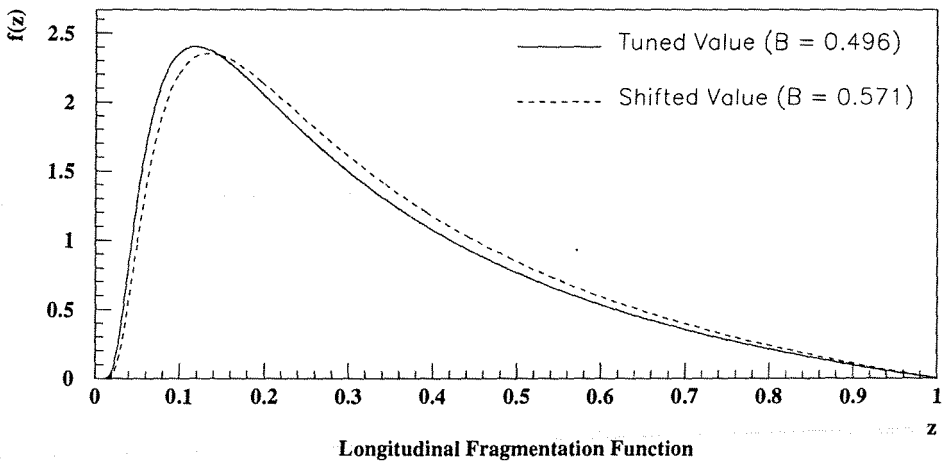

Figure 7.13: A comparison of the fragmentation function for the normal parameter tuning (full line) and the 5σ de-tuned case (dashed line). Both plots have been normalized to the same area. In the plot a typical value of $m_T^2 = 0.27$ GeV^2 has been assumed.

Systematic Check	$\frac{C_A}{C_F}$	$\Delta(\frac{C_A}{C_F})$	sig$(\frac{C_A}{C_F})$	$\frac{T_R}{C_F}$	$\Delta(\frac{T_R}{C_F})$	sig$(\frac{T_R}{C_F})$	χ^2
Hadronization	2.447 ± 0.183	0.161	0.879	1.023 ± 0.444	-0.370	-0.834	1.27

Energy Calculation Algorithm

In the energy calculation algorithm introduced in Section 4.5.3 all events which have a jet energy re-scaling factor greater than 3 are removed from the sample. This value was chosen as a compromise between statistical coverage and the exclusion of ill-defined jets, but as the re-clustering process which follows the calculation also removes poorly reconstructed events the cut value is not critical. In order to check the influence on the results the full analysis was repeated with maximum re-scaling factors of 2 and 4. The results of the new fits are shown below.

Systematic Check	$\frac{C_A}{C_F}$	$\Delta(\frac{C_A}{C_F})$	sig$(\frac{C_A}{C_F})$	$\frac{T_R}{C_F}$	$\Delta(\frac{T_R}{C_F})$	sig$(\frac{T_R}{C_F})$	χ^2
Rescale Cut=2	2.221 ± 0.133	-0.065	-0.487	1.562 ± 0.320	0.169	0.527	1.61
Rescale Cut=4	2.290 ± 0.128	0.004	0.033	1.461 ± 0.307	0.068	0.222	1.63

Histogram Binning

In the nominal analysis there are 10 bins for each ACV. The possibility that this choice introduced some effect on the results was investigated by repeating the analysis with 9 and 11 bins in each distribution. The results are shown below.

Systematic Check	$\frac{C_A}{C_F}$	$\Delta(\frac{C_A}{C_F})$	sig$(\frac{C_A}{C_F})$	$\frac{T_R}{C_F}$	$\Delta(\frac{T_R}{C_F})$	sig$(\frac{T_R}{C_F})$	χ^2
9 bins per ACV	2.340 ± 0.128	0.054	0.423	1.266 ± 0.312	-0.127	-0.406	2.05
11 bins per ACV	2.274 ± 0.129	-0.012	-0.094	1.428 ± 0.312	0.035	0.112	1.71

7.3.4 Error Analysis Conclusion

The UDSC Sample

The following table summarizes the contribution to the udsc sample experimental error from each source. The scheme used to evaluate the size of the error is to take half the maximum deviation for each effect. This method is intended to compensate in some measure for the contribution to each shift from the limited

Monte-Carlo statistics: This factor is highlighted by the low significance value of many of the errors.

Systematic Effect	$\frac{C_A}{C_F}$	$\sigma(\frac{C_A}{C_F})$	$\frac{T_R}{C_F}$	$\sigma(\frac{T_R}{C_F})$
Clustering	2.229	-0.057	1.650	0.257
Detector Simulation	2.361	0.075	1.330	-0.064
ISR & FSR	2.282	-0.005	1.328	-0.066
Hadronization	2.367	-0.081	1.208	-0.185
Jet Energy Calculation	2.254	-0.033	1.478	0.085
Histogram Binning	2.313	0.027	1.203	-0.064
Statistical	2.286	0.129	1.393	0.309

The sum in quadrature of all systematic contributions to the udsc sample uncertainty is included in the final error quoted below where the first error is statistical and the second is systematic.

$$\frac{C_A}{C_F}_{udsc} = 2.286 \pm 0.129_{stat} \pm 0.131_{syst} \qquad \frac{T_R}{C_F}_{udsc} = 1.393 \pm 0.309_{stat} \pm 0.346_{syst}$$

Combining these errors in quadrature we obtain the udsc result shown below.

$$\frac{C_A}{C_F}_{udsc} = 2.286 \pm 0.184 \qquad \frac{T_R}{C_F}_{udsc} = 1.393 \pm 0.464$$

The B Sample

In calculating the b sample systematic contributions the same scheme has been adopted as for the udsc sample. The common uncertainties arise from the same phenomena and the uncertainties derived for the udsc sample are also adopted for the b sample. The following table summarizes the contribution to the b sample experimental error from each source.

Systematic Effect	$\frac{C_A}{C_F}$	$\sigma(\frac{C_A}{C_F})$	$\frac{T_R}{C_F}$	$\sigma(\frac{T_R}{C_F})$
Clustering	2.229	-0.057	1.650	0.257
Detector Simulation	2.361	0.075	1.330	-0.064
ISR & FSR	2.282	-0.005	1.328	-0.066
Monte-Carlo B Purity	2.273	-0.013	1.579	0.186
Hadronization	2.367	-0.081	1.208	-0.185
Jet Energy Calculation	2.254	-0.033	1.478	0.085
Histogram Binning	2.313	0.027	1.203	-0.064
Statistical	2.298	0.091	2.347	0.913

The sum in quadrature of all systematic contributions to the b sample uncertainty is included in the final error quoted below where the first error is statistical and the second is systematic.

$$\frac{C_A}{C_F}_b = 2.298 \pm 0.091_{stat} \pm 0.132_{syst} \qquad \frac{T_R}{C_F}_b = 2.347 \pm 0.913_{stat} \pm 0.393_{syst}$$

Combining these errors in quadrature we obtain the b result shown below.

$$\frac{C_A}{C_F}_b = 2.298 \pm 0.160 \qquad \frac{T_R}{C_F}_b = 2.347 \pm 0.994$$

7.4 Summary

The two results given above are derived from independent samples and can be combined by weighting each result with its statistical error following the standard method of Reference [52]. The final error is calculated assuming the two measurements share common systematic effects. These lead to the error contributions shown below.

$$\frac{C_A}{C_F}_{final} = 2.294 \pm 0.074_{stat} \pm 0.132_{syst} \qquad \frac{T_R}{C_F}_{final} = 1.491 \pm 0.293_{stat} \pm 0.393_{syst}$$

The final result obtained from the sum in quadrature of the systematic and statistical uncertainties is then:

$$\frac{C_A}{C_F}_{final} = 2.294 \pm 0.151 \qquad \frac{T_R}{C_F}_{final} = 1.491 \pm 0.490$$

in agreement with the QCD prediction introduced in Section 1.3.4 of $\frac{C_A}{C_F} = 2.25$ and $\frac{T_R}{C_F} = 1.875$. These values are displayed in the $\frac{C_A}{C_F}$, $\frac{T_R}{C_F}$ plane in Figure 7.14 together with the udsc and b sample results and the QCD prediction.

It is possible to re-express the result presented above for $\frac{T_R}{C_F}$ by recalling the definition $T_R = n_f T_F$. By assuming the Standard Model prediction of $n_f = 5$ we obtain the measurement of $\frac{T_F}{C_F}$ displayed below which is in agreement with the QCD prediction of $\frac{T_F}{C_F} = 0.375$.

$$\frac{T_F}{C_F} = 0.298 \pm 0.059_{stat} \pm 0.079_{syst}$$
$$\frac{T_F}{C_F} = 0.298 \pm 0.098$$

Alternatively the $\frac{T_R}{C_F}$ result can be used to obtain a limit on the number of strongly interacting fermions, n_f. Assuming the QCD value of $\frac{T_F}{C_F} = 0.375$ we obtain:

$$n_f = 3.976 \pm 0.781_{stat} \pm 1.048_{syst}$$
$$n_f = 3.976 \pm 1.307$$

in agreement with the Standard Model prediction of $n_f = 5$. This value can be expressed as a limit on gluino production which would predict $n_f = 8$ for the case of a massless gluino. This possibility can be excluded at $> 99\%$ confidence level by the result.

In the case of a massive gluino the limit is weakened by the phase space suppression inherent in massive particle production which results in a tendency to reduce the impact on n_f with respect to the massless case. The type of suppression factor suggested in [59] translates here into $\sqrt{1-(2m_{gluino})^2/(sy_{jade})}$ where we have used the minimum invariant mass between two jets ($\sqrt{sy_{jade}}$) as the mass scale of the process. The JADE algorithm $y_{cut} = 0.03$ is used as it is equivalent to the DURHAM $y_{cut} = 0.01$ used in the analysis. This formula

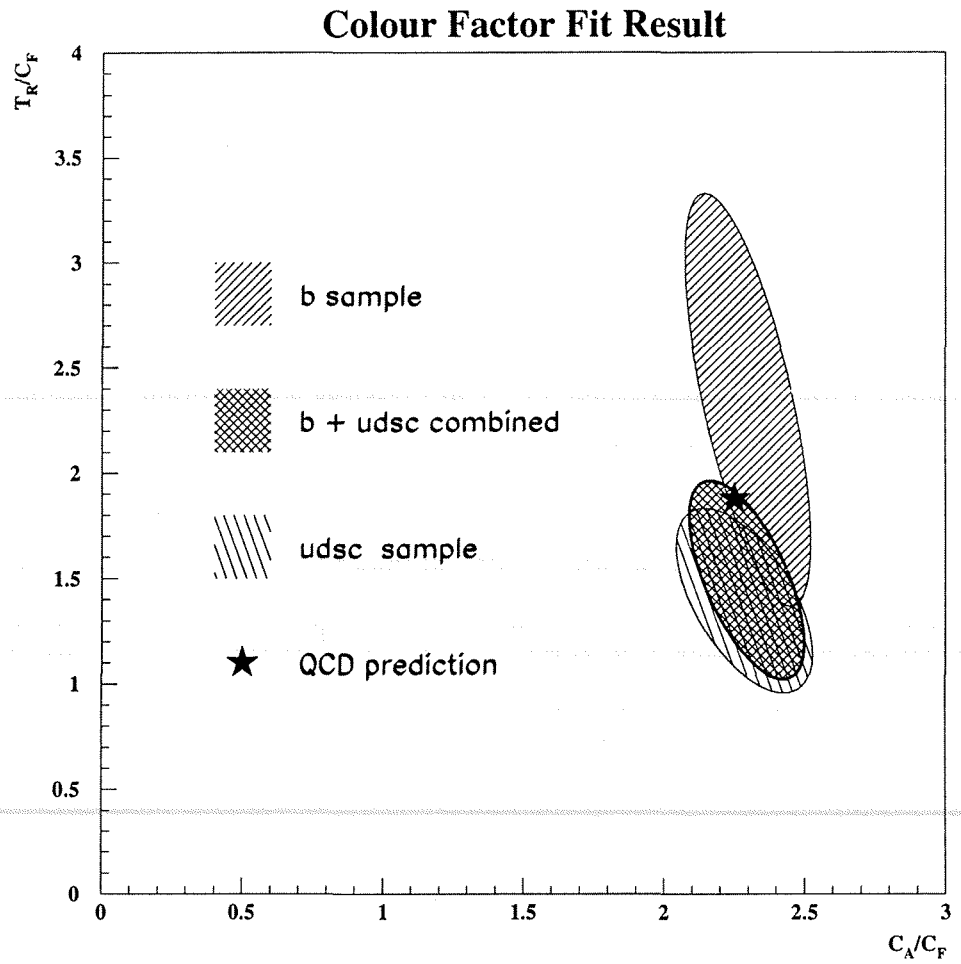

Figure 7.14: The final result displayed in the $\frac{C_A}{C_F}, \frac{T_R}{C_F}$ plane. The star represents the QCD prediction for the two ratios. The ellipses represent the combined statistical and systematic error on each measurement.

correctly reproduces the suppression predicted by the MME calculation for the b quark mass.

The 95% confidence level limit on the change in n_f above its predicted value of 5 is $\delta n_f < 1.59$. We combine this with the above formula for the mass suppression to obtain a lower limit on the gluino mass as shown below.

$$\delta n_f = 3\sqrt{1 - \frac{(2m_{gluino})^2}{(sy_{jade})}} < 1.59$$

$$m_{gluino} > 6.70 \text{ GeV}.$$

Figure 7.15 displays the result in the $\frac{C_A}{C_F}, \frac{T_F}{C_F}$ plane together with the Colour Factor ratios of several theories. The massless gluino point is derived assuming that the increase in n_f from 5 to 8 is expressed as an enhancement of $\frac{T_F}{C_F}$ by $0.375 \times (\frac{8}{5}) = 0.6$. The abelian gluon model is a toy model of the strong interaction with three colours but no gluon self-coupling [40]. The QED point which is based on a U(1) symmetry group is displayed for comparison as are the SU(2) and SU(4) points.

Discussion of Statistical Error

The statistical accuracy of the udsc result is largely as expected. However in the b sample the error on $\frac{T_R}{C_F}$ is relatively large, especially when compared with the $\frac{C_A}{C_F}$ error which is smaller than in the udsc sample even though the b sample contains 15 times fewer events. The reason for the difference in the two b sample accuracies is not statistical as equal numbers of events are used to derive both results.

On examination of the correlation coefficients measured by the fitting routine the reason for the discrepancy becomes clear. In the udsc sample the ACV plots from the α, β and γ processes are correlated to approximately the same level, with correlation coefficients as shown below. Recall that the α, β and γ processes are related to C_F, C_A and T_R respectively.

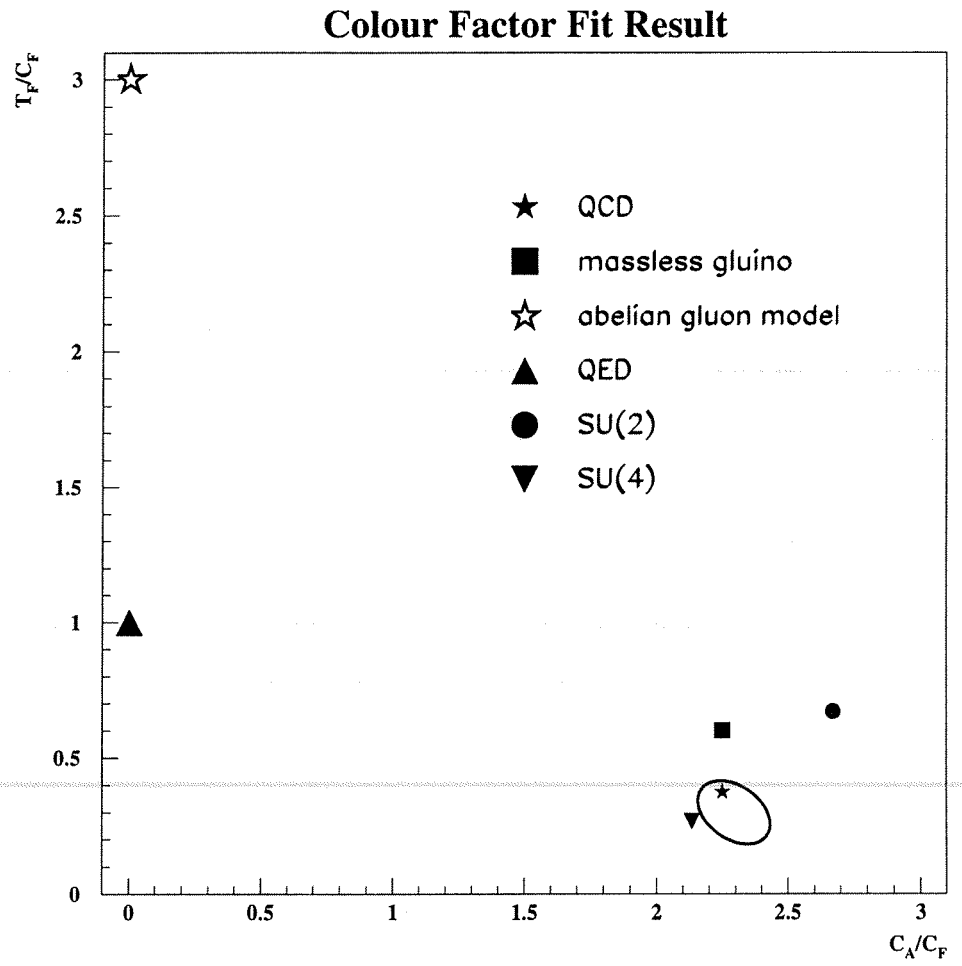

Figure 7.15: The final result displayed in the $\frac{C_A}{C_F}, \frac{T_F}{C_F}$ plane. The star represents the QCD prediction and the ellipse represents the combined final result.

$$\rho(C_F, C_A) = -0.340 \qquad \rho(C_F, T_R) = -0.501 \qquad \rho(C_A, T_R) = -0.424$$

However in the case of the b sample we use the massive matrix element predictions in the fit and place the tagged jets in position 1 and 2. In this scheme the α and γ distributions display some similarities in shape and we observe a large correlation between the two in the fit results. The strong similarity between the distributions dilutes the potential accuracy of the $\frac{T_R}{C_F}$ b-tagged measurement. The correlation coefficients determined from the b sample are displayed below.

$$\rho(C_F, C_A) = 0.251 \qquad \rho(C_F, T_R) = -0.823 \qquad \rho(C_A, T_R) = -0.338$$

Discussion of Systematic Error

The evaluation of systematic effects has not revealed any problems with the method. This fact gives us confidence in the accuracy of the result which is reinforced by the similar conclusions derived from two independent samples with complementary techniques.

Chapter 8

Conclusions

This thesis presents a measurement of the Colour Factors of Quantum Chromodynamics from 4-jet events observed with the ALEPH detector using data collected at the LEP accelerator between 1992 and 1995.

The analysis contains two distinct elements which combine to provide the following Colour Factor results:

$$\frac{C_A}{C_F} = 2.294 \pm 0.151 \qquad \frac{T_R}{C_F} = 1.491 \pm 0.490$$

which are in agreement with the QCD predictions of $\frac{C_A}{C_F} = 2.25$ and $\frac{T_R}{C_F} = 1.875$.

These results are among the most accurate measurements of these quantities to date and confirm QCD as the theory of the strong interaction. The possibility of a supersymmetric gluino below 6.7 GeV is excluded at the 95% confidence level.

References

[1] CDF Collaboration, Phys. Rev. Lett. 74 (1995) 2626.

[2] R. P. Feynman, Rev. Mod. Phys. 20 (1948) 367. J. Schwinger, Phys. Rev. 74 (1948) 1439.

[3] F. Combley, Rep. Prog. Phys. 42 (1979) 1889.

[4] M. Drees, APCTP-05 SLAC HEP-PH/9611409 (1996).

[5] S. Moretti et al., CERN HEP-PH/9609206 (1996);
R. Muñoz-Tapia, W.J. Stirling, Phys. Rev. D 49 (1994) 3763.

[6] H. Fritzsch, M. Gell-Mann, H. Leutwyler, Phys. Lett. B 47 (1973) 365.

[7] G. Altarelli, G. Parisi, Nucl. Phys. B 126 (1977) 298.

[8] T. Sjöstrand, Comput. Phys. Commun. 27 (1982) 243; 28 (1983) 229;
T. Sjöstrand, M. Bengtsson, Comput. Phys. Commun. 43 (1987) 367;
T. Sjöstrand, Comput. Phys. Commun. 82 (1994) 74.

[9] G. Marchesini, B.R. Webber, Nucl. Phys. B 238 (1984) 1.

[10] ALEPH Collaboration, D. Buskulic et al., submitted to ICHEP94 Session Pa-11, Glasgow, 20-27 July 1994, Ref 0529;
DELPHI Collaboration, P. Abreu et al., Phys. Lett. B 274 (1992) 498;
L3 Collaboration, B. Adeva et al., Phys. Lett. B 264 (1991) 551;
OPAL Collaboration, G. Alexander et al., Z. Phys. C 52 (1991) 543.

[11] ALEPH Collaboration, D. Decamp et al., Nucl. Instr. and Meth. A 294 (1990) 121.

[12] ALEPH Collaboration, D. Buskulic et al., Nucl. Instr. and Meth. A 360 (1995) 481.

[13] W.B. Atwood et al., Nucl. Instr. and Meth. A 306 (1991) 446.

[14] D. Casper, 'ALEPH ONLINE 101 An introduction to the ALEPH Online System', ALEPH 93-026 SOFTWR 93-006.

[15] R. Fruhwirth, HEPHY-PUB 503/87 (1987).

[16] M. Towrie, Ph. D. Thesis, 'Multiphoton Resonant Ionisation - Applications to High Energy Physics', University of Glasgow, 1987.

[17] H.G. Sander, M. Schmelling, R. St.Denis, 'Measurement of the Mirrors in the ALEPH TPC', ALEPH 89-133, TPCGEN 89-014.

[18] M. Schmelling, B. Wolf, 'Laser Calibration of the ALEPH TPC', ALEPH 91-150, TPCGEN 91-004.

[19] F. Sauli, 'Instrumentation in High Energy Physics', World Scientific, London, 1992.

P. Langevin, C. R. Acad. Sci. Paris 146 (1908) 530.

[20] D. Colling, B. Wolf, 'First Results of the ITC/TPC Alignment from the 1991 Cosmics Run', ALEPH 91-065 TPCGEN 91-002.

[21] ALEPH Collaboration, D. Decamp et al., Nucl. Instrum. Methods A294 (1990) 121.

[22] A. I. M. Rae, 'Quantum Mechanics' (2nd ed.), Hilger, Bristol, 1986.

[23] A. Breakstone et al., Phys. Lett. B 248 (1990) 220.

[24] J. Ellis et al., Phys. Lett. B 305 (1993) 375.

[25] G. Farrar, Phys. Rev. D 51 (1995) 3904.

[26] J.G. Korner, G. Schierholz, J. Willrodt, Nuc. Phys. B 185 (1981) 365.

[27] O. Nachtmann, A. Reiter, Z. Phys. C 16 (1982) 45.

[28] M. Bengtsson, P.M. Zerwas, Phys. Lett. B 208 (1988) 306.

[29] M. Bengtsson, Z. Phys. C 42 (1989) 75.

[30] DELPHI Collaboration, P. Abreu et al., Phys. Lett. B 255 (1991) 466.

[31] DELPHI Collaboration, P. Abreu et al., Z. Phys. C 59 (1993) 357.

[32] L3 Collaboration, B. Adeva et al., Phys. Lett. B 248 (1990) 227.

[33] L3 Collaboration, B. Adeva et al., submitted to ICHEP94 Session Pa-11, Glasgow, 20-27 July 1994.

[34] OPAL Collaboration, M.Z. Akrawy et al., Z. Phys. C 49 (1991) 49.

[35] OPAL Collaboration, M.Z. Akrawy et al., Z. Phys. C 65 (1995) 367.

[36] OPAL Collaboration, R. Akers et al., Z. Phys. C 68 (1995) 519.

[37] VENUS Collaboration, K. Abe et al., Phys. Rev. Lett. 66 (1991) 280.

[38] ALEPH Collaboration, D. Decamp et al., Phys. Lett. B 284 (1992) 151.

[39] ALEPH Collaboration, D. Decamp et al., submitted to ICHEP94 Session Pa-11, Glasgow, 20-27 July 1994.

[40] S. Bethke, A. Ricker, P.M. Zerwas, Z. Phys. C 49 (1991) 59.

[41] R.K. Ellis, D.A. Ross, A.E. Terrano, Nuc. Phys. B 178 (1981) 421.

[42] A. Ballestrero, E. Maina, S. Moretti, Nuc. Phys. B 415 (1994) 265.

[43] H.A. Olsen, P. Osland, I. Overbo, Phys. Lett. B 89 (1980) 221.

[44] F. Halzen, A.D. Martin, 'Quarks and Leptons', J. Wiley & Sons, New York, 1984.

[45] ALEPH Collaboration, D. Decamp et al., Z. Phys. C 55 (1992) 209.

[46] Y. Dokshitzer, J. Phys. G 17 (1991) 1441.

[47] C.W. Evans, 'Engineering Mathematics' (1st ed.), Van Nostrand Reinhold, London, 1989.

[48] JADE Collaboration, W. Bartel et al., Z. Phys. C 33 (1986) 23; Phys. Lett. B 213 (1988) 235.

[49] M. Scarr, I. Ten Have, 'PTCLUS: a Jet Finding Algorithm for High Energy Hadronic Final States', ALEPH 89-150, PHYSIC 89-060.

[50] ALEPH Collaboration, D. Buskulic et al., Phys. Lett. B 384 (1996) 353.

[51] ALEPH Collaboration, D. Buskulic et al., Phys. Lett. B 369 (1996) 151.

[52] Particle Data Group, R.M. Barnett et al., Phys. Rev. D 54 (1996) 1.

[53] D. Brown, M. Frank, 'Tagging B Hadrons using Impact Parameters', ALEPH 92-135, PHYSIC 92-124.

[54] T. Mattison, 'QVSRCH: A Tool for Inclusive Secondary Vertex Finding', ALEPH 92-173, PHYSIC 92-155.

[55] F. James, 'MINUIT - Function Minimization and Error Analysis' CERN Program Library entry D506.

[56] R.J. Barlow, 'Statistics - A Guide to the Use of Statistical Methods in the Physical Sciences' (1st ed.), John Wiley & Sons, Chichester, 1989.

[57] L. Dixon and A. Signer, SLAC-PUB-7309, 1996.

[58] L. Dixon and A. Signer, Private Communication, 1997.

[59] D.H. Perkins, 'Introduction to High Energy Physics' (3rd ed.), Addison-Wesley, Menlo Park, California, USA, 1986.